uc3m | Universidad Carlos III de Madrid

Master Degree in Aerospace Engineering
2018-2019

*Master Thesis*

# "Intrinsic Calibration of Air Pressure Measurements using Laser Spectroscopy"

---


Cristina Benéitez Ortega

Stefano Discetti

Raoul-Amadeus Lorbeer


02/09/2019, Madrid (Spain)

**AVOID PLAGIARISM**

The University uses the Turnitin Feedback Studio program within the Aula Global for the delivery of student work. This program compares the originality of the work delivered by each student with millions of electronic resources and detects those parts of the text that are copied and pasted. Plagiarizing in a TFM is considered a **Serious Misconduct**, and may result in permanent expulsion from the University.

# ABSTRACT

Since the very beginning of aviation, instruments have been placed on the aircraft to analyze the airflow's characteristics. Pitot-static tubes and static ports are two examples of this type of devices. They are commonly used for measuring static pressure, so the altitude and speed aircraft is flying at can be estimated a posteriori.

Focusing into Pitot-static tubes, since their very first known incorporation in military aircraft (August, 1912), they have been the primary instrument on board to estimate the speed of flight through the air [1]. Pitot-static tubes measure flow speed via the static and stagnation pressure difference. They are simple and small devices located on the fuselage accurately measure the air flow pressure with a very small intrusive approach. Although these characteristics are the reason for a continuous and successful performance of Pitot-static tubes, isolated aircraft accidents can happen from their malfunction. Misalignments with the flow's direction and obstructions inside the probe are possible causes that can lead to such catastrophes, as for example the Air France Fligh 447 crash.

Centering now the attention to static ports, they collect the outside static pressure and send the value to other instruments for future usage. Vertical speed indicators, altimeters and pressurization systems are various examples fed by the static ports. Similarly to Pitot-tubes, their simple structure allows them to read pressure values in a non-intrusive way. Nonetheless, apart from their numerous advantages, static ports are immersed in the fuselage's skin, making the acquired pressure values to be affected by the fuselage itself. Furthermore, they can be easily obstructed too, leading to wrong pressure readings.

The aim of this Master Thesis is to propose other alternative for measuring the flow's static pressure and demonstrate its potential use in the aerospace field. The technique selected is called Tunable Diode Laser Absorption Spectroscopy (TDLAS). Its working principle relies on acquiring value of static pressure from the width of oxygen absorption lines. Hence, in this paper, spectroscopy experiments to prove this previous statement are presented. To validate pressure results, they are contrasted against pressure readings from a mechanical sensor. Moreover, to support its implementation into the aerospace field, the location of TDLAS in the airplane has been analyzed as well as preliminary designs for the technique's enclosure.

From the comparison between both readings, the viability of using TDLAS for static pressure estimation has been proved. A 0.04 atm difference from sensor's pressure has been obtained. As for the implementation into the aircraft, components directly involved into the absorption process are defined to be housed in airfoil shapes at the upper central part of the fuselage meanwhile the remaining components are kept inside the aircraft.

**Keywords**

TDLAS, Static Pressure, Spectroscopy, Asorption of Light

# ACKNOWLEDGMENTS

Although in engineering they teach you how to use a tool in order to find the solution of a problem and solve it, I have a liking for understanding the problem itself and the science beyond it. Quoting Edward Teller from the very last slide of my presentation: *"The science of today is the technology of tomorrow"*, for me "how this problem arise?" is as important as "how can I solve it?". For this reason, when I was looking for a master thesis, I did not want just to focus into aeronautics but in other scientific fields.

In the direction of this though, I looked for different international aerospace companies that also have other scientific departments to work in. After searching for different types of master thesis, I found the most attractive one for me at the Deutsches Zentrum für Luft- und Raumfahrt (DLR) Technical Physics Department in Stuttgart (Germany).

*"Intrinsic Calibration of Air Pressure Measurements using Laser Spectroscopy"* is a master thesis that has given me the opportunity to accomplish my goal. It encloses three of the pillars that science is based on: aeronautics, physics and electronics. During these months, I have improve my knowledge in each one of the fields. Moreover, in relation with the soft skills gained in this time, I would like to outstand my communication skills. Working in an international company has given me the possibility to improve my English and also begin to learn a new language, German.

For all the reasons previously mentioned, I would like to thank my DLR supervisor Dr. Raoul-Amadeus Lorbeer for placing his trust in me to develop this master thesis. His continued support and guidance have been indispensable for successfully accomplish the master thesis objectives. Thanks to him, I submerged into several physics fields of research, such as optical physics and laser science, acquiring abundant knowledge in them. I would also like to express my gratitude to Dr. Oliver Kliebisch from the DLR for his extended discussions and valuable suggestions which have contribute greatly to the Master Thesis development. In addition, I would like to give special thanks to the Technical Physics Department for the excellent working conditions provided and for giving me the possibility to use daily their installations for the spectroscopy experiments.

Finally, I would like to acknowledge my supervisor from Universidad Carlos III de Madrid (Spain), Dr. Stefano Discetti, for his constant support and his advices throughout the development of the thesis.

# LIST OF ACRONYMS

---

**A/C** Aircraft

**FP** Fabry Perot Interferometer

**FT** Fourier Transform

**FWHM** Full Width Half Maximum

**HITRAN** HIgh-resolution TRANsmission molecular absorption database

**HT** Hilbert Transform

**HWHM** Half Width Half Maximum

**LD** Laser Diode

**LPF** Low Pass Filter

**MZ** Mach Zehnder Interferometer

**OFDR** Optical Frequency-Domain Reflectometer

**OSA** Optical Spectrum Analyzer

**TAS** True Airspeed

**TDLAS** Tunable Diode Laser Absorption Spectroscopy

**TEC** Thermoelectric Controller

**TLS** Tunable Laser Source

# CONTENTS

# LIST OF FIGURES

# LIST OF TABLES

# 1. INTRODUCTION

## 1.1. Motivation of Work

As an example of a catastrophe from the wrong performance of static pressure measuring instruments, in 2009, the Air France Flight 447 crashed into the middle of Atlantic Ocean without any survivors. According to the final report developed by the Bureau d'Enquêtes et d'Analyses pour la sécurité de l'aviation civile (BEA), the temporary inconsistencies of the airspeed values during the flight leaded the A/C to enter in the aerodynamic stall without any possible recovery. [1]

The cause behind this discrepancy in the speed values was a direct consequence of a Pitot-static tube failure when reading the pressure. Since the beginning of aviation history, Pitot tubes have been the primary device on board to estimate the speed at which the aircraft is flying. This is done via pressure difference. They consist of a probe with two types of holes at specific different locations. Recapitulating in its principle of operation, the holes located at the sidewalls measure the static pressure of the flow meanwhile the hole in the front is destined to read the stagnation pressure, as illustrates Figure 1.1.

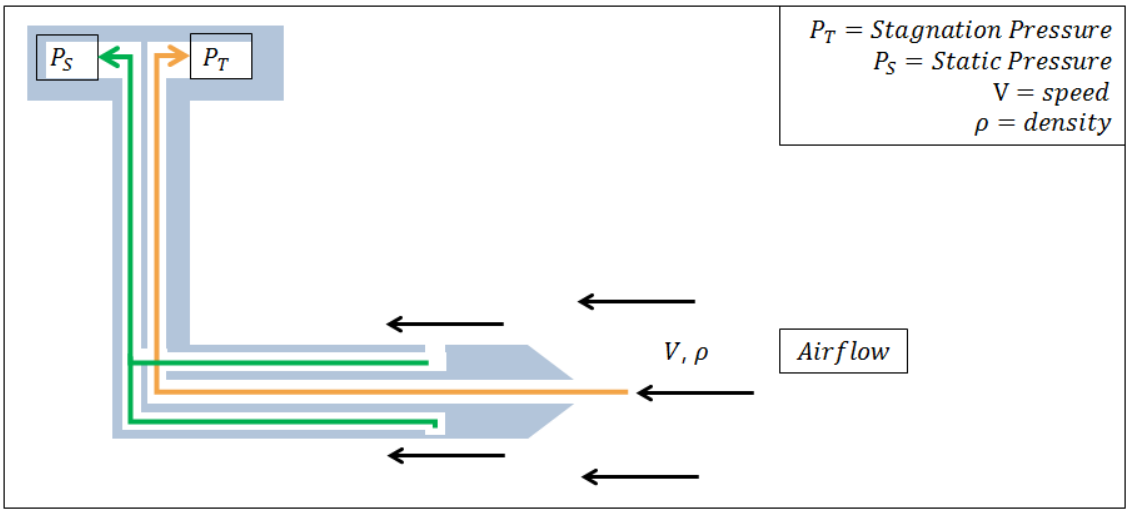


Fig. 1.1. Pitot-Static tube working principle

Applying the energy balance equation at those locations, an expression as a function of both kinetic and potential energy is obtained. In this expression, the left hand side corresponds to the sidewall hole meanwhile the right hand side to the front one:

$$p_s + \frac{1}{2}\rho V^2 + \rho g z_s = p_0 + \frac{1}{2}\rho V_0^2 + \rho g z_0 \tag{1.1}$$

[1] Bureau d'Enquêtes et d'Analyses pour la sécurité de l'aviation civile, "Final Report - On the accident on 1st June 2009 to the Airbus A330-203 registered F-GZCP operated by Air France flight AF 447 Rio de Janeiro - Paris" (2012)

where $p_s$ is the static pressure, $\rho$ is the density of the flow, $V_1$ and $V_0$ correspond to the velocity value at each location according to the local vertical coordinate, g is the gravity constant, $z_{s_1}$ and $z_0$ are the location of each point in the Pitot tube and $p_0$ is the stagnation pressure. Assuming the hydrostatic pressure difference governed by $z_{s_1}$ and $z_0$ is negligible, the speed at the stagnation hole is equal to zero and incompressible flow, the energy balance equation can be reduced to the well-known Bernoulli's equation[2].

$$p_s + \frac{1}{2}\rho V^2 = p_0 \rightarrow \frac{1}{2}\rho V^2 = p_s - p_0 \tag{1.2}$$

Substituting into the expression the static $p_s$ and stagnation pressure $p_0$ obtained from the Pitot-static tube measurements, the dynamic pressure term is obtained. Then, with the aid of the temperature sensors placed on the fuselage's skin, temperature and altitude at each instant of time during the flight profile are measured. Knowing the altitude, density can be calculated straightforward. Finally, placing all the three parameters into Bernoulli's equation and resolving for the speed, the true airspeed is estimated.

$$V = \sqrt{\frac{2\,(p_0 - p_s)}{\rho}} \tag{1.3}$$

As assumed beforehand, Equation 1.3 is only true for incompressible flows i.e. Mach numbers less than 0.3. Nonetheless, aircraft today usually fly at Mach numbers around 0.8, where compressibility effects cannot be further neglected. This includes significant density and temperature changes in the flow. Hence, two more variables are included for the speed computation, being the energy balance rewritten as [3]

$$\frac{1}{2}\rho V^2 = \frac{\gamma}{\gamma - 1} p_s \left[ \left( \frac{p_0}{p_s} \right)^{\frac{\gamma-1}{\gamma}} - 1 \right] \tag{1.4}$$

where $\gamma$ is defined as the specific heat ratio. Thus, the speed is determined from

$$V = \sqrt{\frac{a_0^2 M^2}{1 + \frac{\gamma-1}{2} M^2}} \tag{1.5}$$

being $a_0$ the speed of sound and M the Mach number, expressed as:

$$a_0 = \sqrt{R\gamma T_0} \tag{1.6}$$

$$M = \sqrt{\frac{2}{\gamma - 1} \left[ \left( \frac{p_0}{p_s} \right)^{\frac{\gamma-1}{\gamma}} - 1 \right]} \tag{1.7}$$

From Eq. 1.7, it is proved that both pressure values estimated with the Pitot-static tube are the main drivers that define the airspeed. A misreading of them leads to an error

in the speed value. This is what happened in the Air France Flight 447 crash. During the flight, probes were blocked with ice crystals. Although the former are equipped with heating systems to avoid the deposition of ice and droplets inside of them, for this flight, the ice was not entirely removed, leading to incorrect readings of the pressures' values. With these errors in both magnitudes, the True Airspeed (TAS) was wrongly computed, being three almost a third part of the real one. To maintain the lift force constant at that flight level without knowing the TAS value, the pilot increased the angle of attack. This action made the aircraft to enter into aerodynamic stall and crashed.

From the chain of consequences just mentioned, one can ask why Pitot-static tubes are still being used in pressure readings. The answer is pretty obvious: they work. Also, they have a simple and small configuration which needs little money to build [4]. An advantage from this configuration is that they cause negligible pressure loss in the airflow when doing measurements. In addition to the list, the installation procedure on the aircraft's skin is easily performed and non-intrusive.

Although these advantages must seem sufficient to continue marking use of Pitot-static tubes, several drawbacks are carried with them, making their working performance not as suitable as desired. To begin with, in order to have a correct lecture of pressure, the probe must be aligned with the direction of the flow. This condition cannot always be fulfilled as the flow direction may be unknown. Secondly, Pitot-static tubes are unappropriated for unsteady aerodynamics by reason of their slow response to changes. Concerning the Euler angles at which the aircraft can be flying, there are substantial errors when the yaw angle is higher than 5 degrees, returning incorrect pressure outcomes[5]. Another weak point of the usage of Pitot-static tubes is the Mach number limitation. When the Mach number has a large value (i.e. supersonic), a correction must be introduced to account for compressibility effects. As stated above, temperature changes are considered and so pressure variations need to be introduced into the model. To deal with these effects, Rayleigh corrections are used. Equation 1.8, 1.9, 1.10 show an example of pressure, temperature and density correction. Here, $M_1$, $P_1$, $T_1$ and $\rho_1$ are the current Mach number and pressure of the flow meanwhile $M_2$, $P_2$, $T_2$ and $\rho_2$ are the corrected magnitudes [6].

$$\frac{P_2}{P_1} = \frac{1 + \gamma M_1^2}{1 + \gamma M_1^2} \tag{1.8}$$

$$\frac{T_2}{T_1} = \left[\frac{1 + \gamma M_1^2}{1 + \gamma M_1^2}\right]^2 \left(\frac{M_2}{M_1}\right)^2 \tag{1.9}$$

$$\frac{\rho_2}{\rho_1} = \frac{M_2}{M_1}\sqrt{\frac{T_2}{T_1}} \tag{1.10}$$

In the other way around, for small Mach numbers Pitot-static tubes give incorrect readings by reason of the small pressure differences. Finally, Pitot-static tubes can easily become obstructed with particles carried by the airflow.

In connection with the last disadvantage previously mentioned, it can be corroborated that weather conditions can tremendously affect the pressure reading. Droplets and ice crystals can deposit inside the probe's openings and alter the measurements, as happened in the crash accident of the Airbus A330-200 [7].

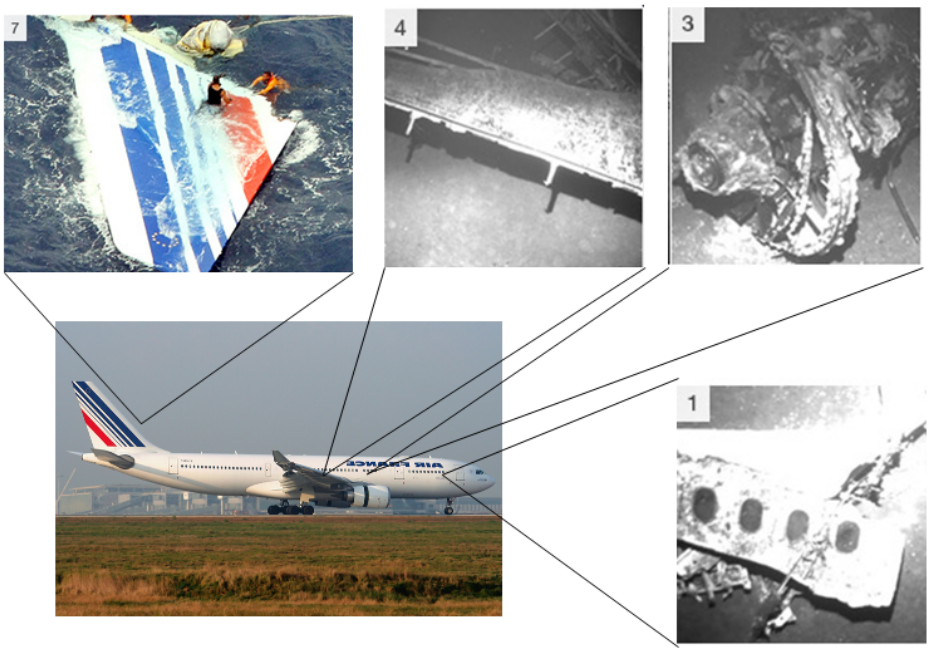


Fig. 1.2. Air France Flight 447 crash

For all the previous reasons, although the Air France Flight 447 crash was a tragic accident caused by both instrument malfunction and human error, engineers are currently looking for a suitable alternative to measure static pressure, so these types of accidents can be prevented. The Air France Flight 447 accident was not an isolated event but one of several fatalities that occur in the aviation field involving the malfunction of instruments on board. As another example, in 1951, the Turkish Airlines Flight 1951 crashed during the landing procedure in Amsterdam Schiphol Airport due to malfunction of the radio altimeter. In this case, the radio altimeter was giving inconsistencies in the aircraft flying height, leading the aircraft to stall and crash.

In addition to these facts, the constant evolution of the aerospace field and the increase of aerial traffic are also pushers leading to this change. For a higher density of traffic, more accurate values of the altitudes aircraft is flying at are required. Keeping this in mind, engineers and scientists have begun to design an alternative technique for static pressure measurements to increase the accuracy of values from both Pitot-static tubes and static ports. The technique presented in this Master Thesis is called Tunable Diode Laser Absorption Spectroscopy (TDLAS).

## 1.2. Master Thesis Objectives

The principal aim of this Master Thesis is to prove TDLAS is a potential substitute for static pressure measurements. The idea behind this purpose is to continue evolving in the scientific level by developing an innovative technique that minimizes the number of disadvantages that static pressure measuring techniques have. For reaching such purpose, different objectives have been established.

- Analysis of consequences from wrong static pressure readings. Example with Pitot-static tubes: understanding fundamentals of performance, reviewing Bernoulli's principle. Identification of the advantages and drawbacks when using static probes for pressure measurements in the aerospace field.
- Extensive examination of TDLAS setup for complete understanding. Break down TDLAS into its components to distinguish each ones's function.
- Meticulous calibration of TDLAS with an interferometer. Comparison between the different interferometers available and deduction of the most suitable for TDLAS. Implementation of the interferometer into the TDLAS setup for further calibratation of the system via temperature sweep procedure.
- Spectroscopy experiments execution using TDLAS. Obtention of the light beams intensities before and after the absorption procedure by the conversion of them into the electrical signals.
- Post-processing of results from the spectroscopy experiment. Determination of the connection between the absorption value described with the electrical signals and the pressure in the experiment. Estimation of the flow static pressure. Validation of the results with the pressure readings from a mechanical sensor.
- Definition of the TDLAS implementation procedure into the aircraft. Preliminary description in terms of location, shape and size of the enclosures where TDLAS will be kept in.

## 1.3. Master Thesis Outline

During the past seven months, each one of the six objectives mentioned above has been effectively accomplished for the complete fulfillment of the Master Thesis's aim. The detailed description of the procedure followed is presented in this paper.

To introduce the reader to this Master Thesis, this section contained a brief outline of the tasks which have been completed through the thesis development. First of all, the problem has to be identified. In this case, there is not an actual need to find a solution to an urgent issue but a desire to avoid the issue by proposing other possible suitable

substitute. Putting names into labels, the motive here is the desire to keep evolving in science by designing a technique capable of measuring static pressure and use it to evolve from both Pitot-static probe and static ports. Therefore, in Chapter 1, an example of a fatality caused by the malfunction of pressure readings was shown. From the fatality, the current performance of the static-pressure mechanism involved was studied, which in this case was the Pitot-static tube. Moreover, the relative advantages and disadvantages of using Pitot-static tubes as instruments for static pressure measurements were evaluated and a conclusion from them, regarding their continued utilization, was made.

Continuing with the Master Thesis outline, the potential alternative to substitute the static pressure mechanisms is brought in. Chapter 2 contains the theoretical approach that will be followed to estimate pressure values. To begin with, an introduction of TDLAS technique and an exhaustive description of the setup is presented. Here each one of the TDLAS setup components will be identified and characterized. Because of setup is not yet calibrated, in this Section it will be included the description of the implementation of the interferometer in the setup for the calibration procedure. Once the setup is calibrated, spectroscopy experiments will be performed. Just to finish, the principle that relates the results from spectroscopy with the static pressure values will be explicitly defined for its computation in the following chapters.

Subsequently, all results from the theoretical approaches described in Chapter 2 are included in Chapter 3. From the calibration procedure previously defined, one type of experiment sweeping in temperature will be performed, giving the value of the calibration parameter, in frequency/phase units. As for static pressure estimation, numerous experiments at different input settings will be performed. Firstly, just one laser diode at ambient pressure will be utilized. Then, one laser diode at variable pressure from 0.2 to 0.96 atm is used. Finally, two laser diodes at different working conditions are used for experiments in which pressure is swept from 0.2 to 0.96 atm. From these three types of experiments, static pressure is estimated. The validation of pressure will also be described in this section by using as reference the pressure sensed with the mechanical sensor.

As a supplemental activity, in Chapter 4 a preliminary design of the device in which TDLAS will be confined is included. It covers the physical location in the aircraft, the aerodynamic shape it will have and the external sizes.

# 2. THEORY

## 2.1. TDLAS Introduction

Throughout last years, new methods have been emerged for improving accuracy of flight parameter measurements. The one in which this study will be focused on is TDLAS. TDLAS is acronym for Tunable Diode Laser Absorption Spectroscopy. It is defined as an innovative technique based on laser spectroscopy, which measures the air flow static pressure of aircraft flying at subsonic regime. At a more detailed level, the working principle of TDLAS relies on the computation of the pressure from the absorption of light in a medium.

As previously mentioned, the purpose of developing this technique is to keep evolving from Pitot-static tubes and static ports. To successfully complete its incorporation into the aerospace field, a project plan was designed. Figure 2.1 shows the complete project's structure as well as the main aim of each one of the stages.

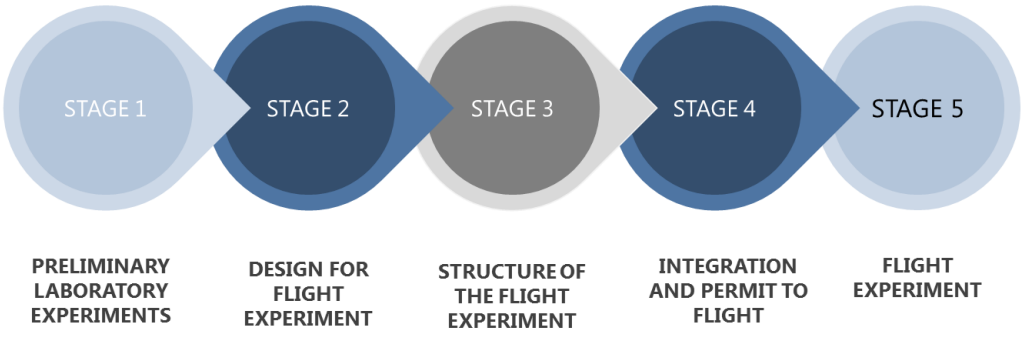


Fig. 2.1. TDLAS project breakdown

As a first step, the viability of the technique has to be proved. In relation to this, Stage 1 is based on the demonstration of the correct acquisition of the flow pressure by means of light absorption. Once the technique has been validated, the devices at which all the instruments, for the TDLAS's utilization, will be kept in have to be designed. The design will include the determination of the device's size and shape as well as the location in the aircraft's structure. It will be the main task for Stage 2. Subsequently, in Stage 3, the characteristics of the flight experiment will be designated. Thereafter, in Stage 4, devices will be incorporated into the aircraft (A/C). The actual configuration of the A/C will be varied by the implementation of the TDLAS devices, leading to changes in the type certificate and so the permit to flight of the A/C. Lastly, the flight experiment with the TDLAS technique on board will be performed in Stage 5.

In consequence of the project's extension and duration, this Master Thesis is going to

completely cover the first stage and part of the second stage, as mentioned in Section 1.

## 2.2. TDLAS Basic Setup

To have a better understanding of TDLAS working principle, Figure 2.2 contains a sketch in which is visualized the basic setup of the TDLAS technique.

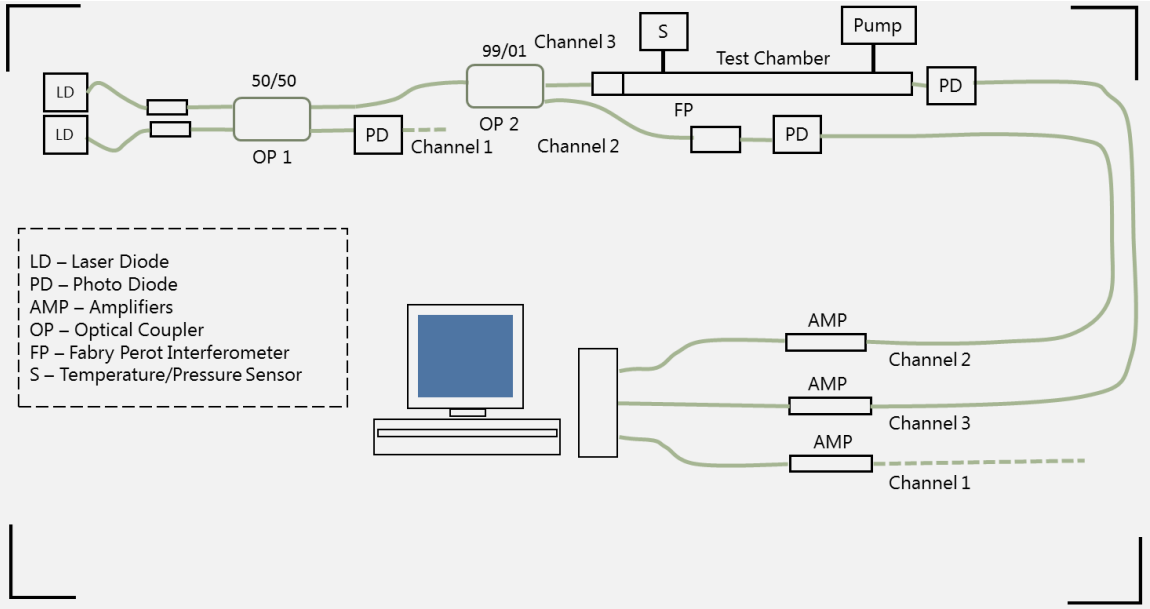


Fig. 2.2. TDLAS setup

Essentially, the system contains two laser diodes (LD). The main purpose of having a pair is to achieve redundant results. Each laser diode will work in parallel at a specific current, temperature and wavelength. These characteristics will be specifically selected for each one so the static pressure results from both are equal. Therefore, it allows to determine how pressure results are affected by the working settings of both laser diodes. Nonetheless, this is just for results comparison during the experiments development. For the TDLAS implemented in the aircraft, just one laser diode will be used.

So, focusing in the TDLAS setup sketch shown above, light is going to travel from the laser diodes through two isolated optical fibers until it reaches the first optical coupler (OP 1). At this point, there is a division of light in 50/50. The 50 % of light flowing in Channel 1 will be automatically converted into electrical current by a photodiode and processed afterwards by the computer. In consequence of the low signal, an amplifier is required before processing the signal, so the noise can be minimized and a cleaned signal obtained. Figure 2.3 shows the light path (yellow path) in this process.

The remaining fifty percent of light from the first optical coupler will travel through the optical fibers until a second optical coupler is reached (OP 2). Then, a new division of light will take place but this time in the order of 99/01. The resulting 99 % of light is the actual light involved in the absorption experiment.

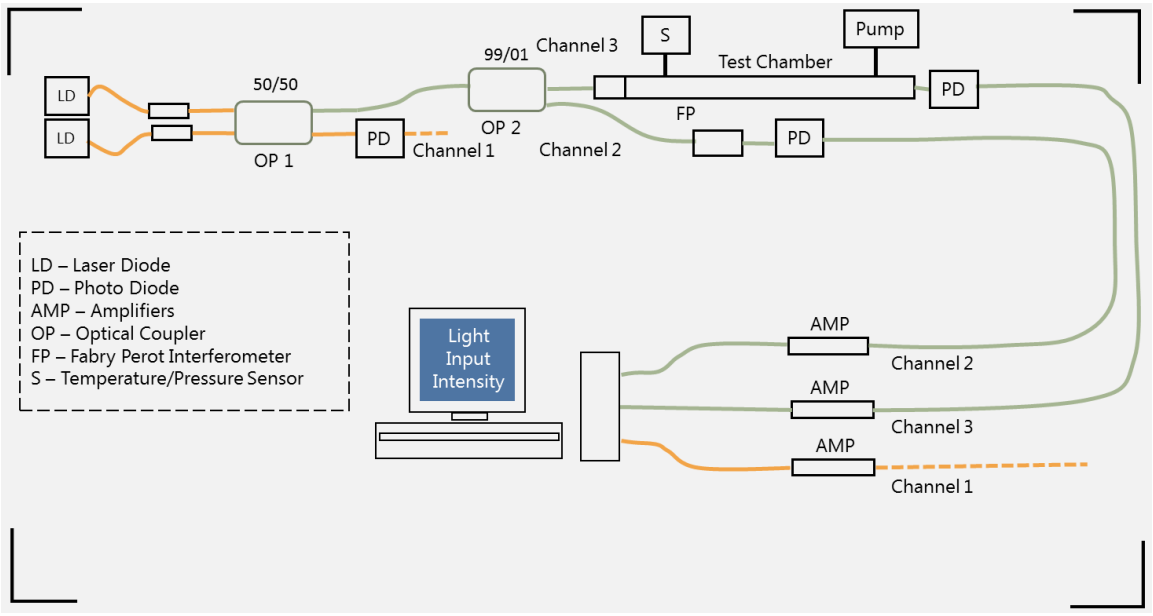


Fig. 2.3. TDLAS setup Channel 1

For the absorption experiment, in order to simulate the flight levels the aircraft with the TDLAS implemented will be flying at, a test chamber filled with air is used in the experiment. The chamber is divided into three parts, being the one at the middle where the absorption itself takes place. A pump connected to the test chamber by a valve is utilized to regulate the intrinsic properties of air, such as pressure and consequently its extensive properties, as for example the amount of substance inside. When switching on the pump and opening the valve, pressure can be easily decreased. Likewise, when switching off the pump and leaving the valve open, pressure automatically increases. To keep a specific pressure inside the test section, the pump is disconnected and the valve closed. To read the pressure and temperature internally, a sensor connected to the section is utilized.

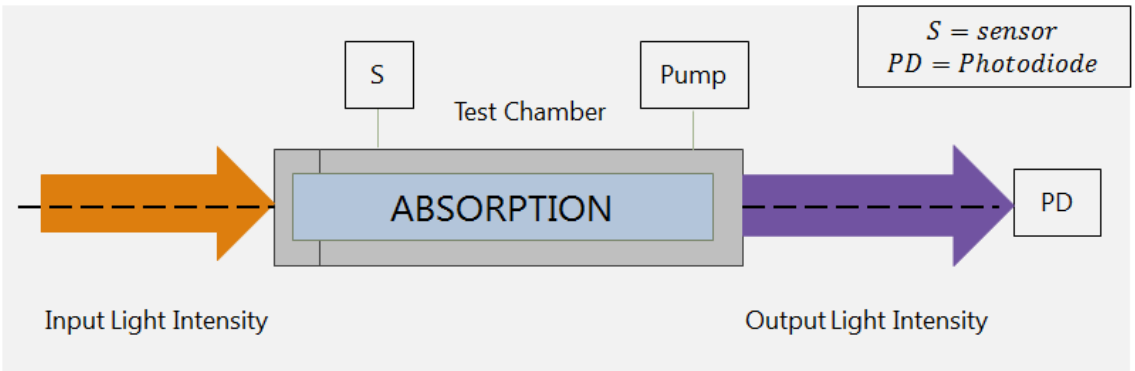


Fig. 2.4. TDLAS absorption process

Stepping backwards in the setup structure, the 99 percent of light coming out of the optical coupler enters into the container. As mentioned beforehand, the test chamber is not operating at vacuum conditions but air is contained inside. The "sensor specie" for the

absorption procedure is the molecular oxygen from air. As a result, a fraction of light will be absorbed by the medium. The remaining amount of light perceived by the photodiode will differ from the input one and so its respective intensity (Figure 2.4). As in Channel 1, the output light from this process will be converted into electrical current and will travel through the electronics of Channel 3 until it is amplified and processed.

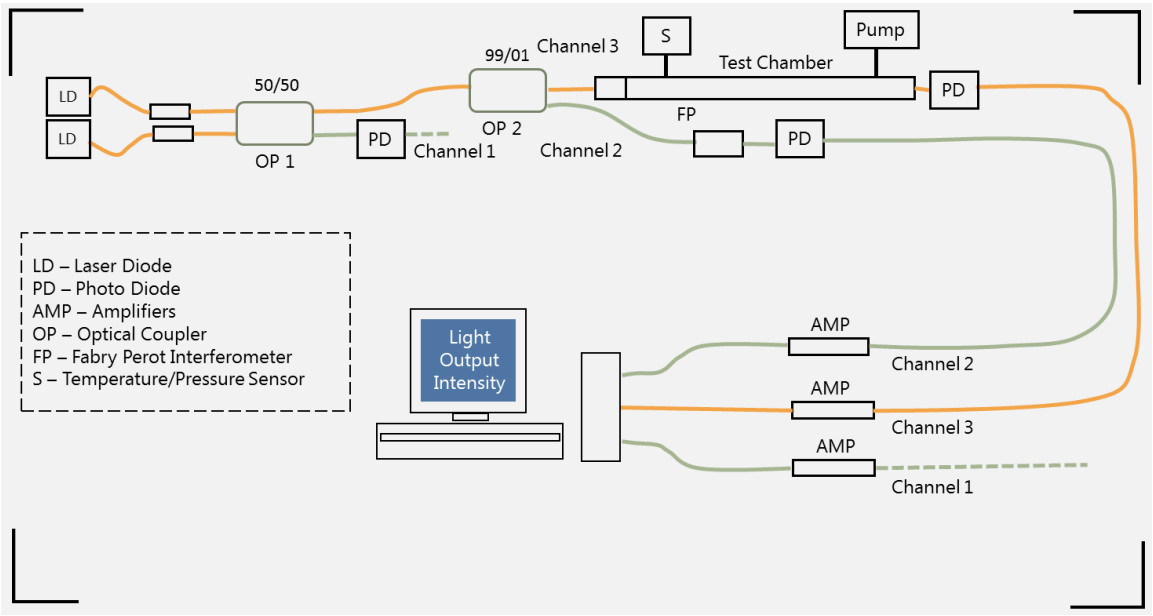


Fig. 2.5. TDLAS setup Channel 3

Lastly, in connection with the remaining 1 % of light from second optical coupler, this amount will enter directly into the Fabry-Perot Interferometer, converted into electrical current, amplified and processed by the computer in Channel 2.

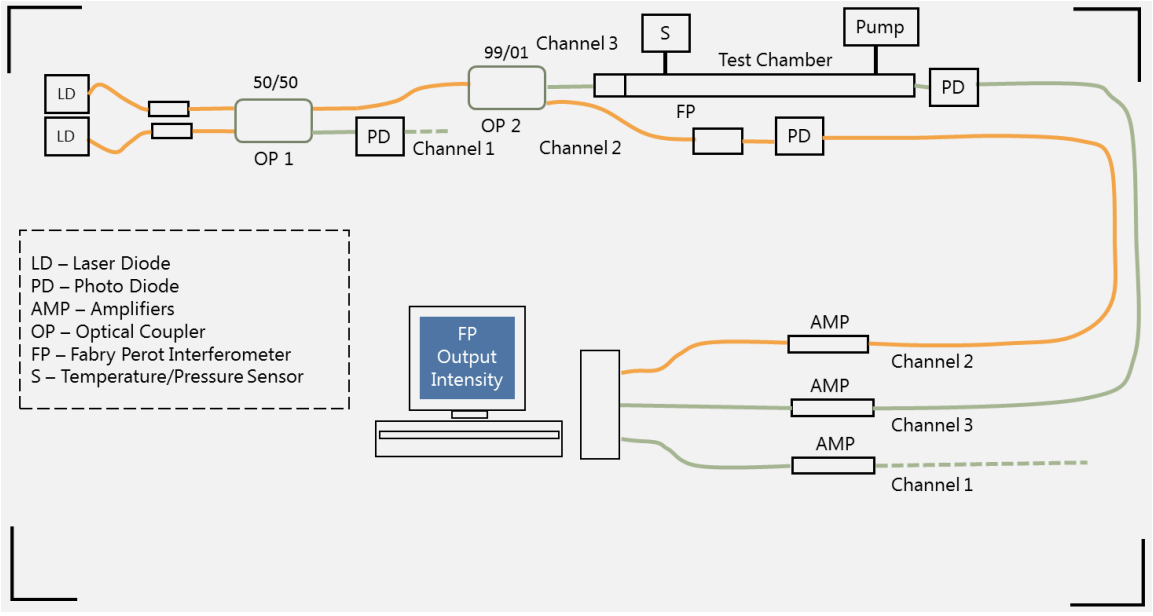


Fig. 2.6. TDLAS setup Channel 2

## 2.3. TDLAS Charcateristics

Concluding with the TDLAS introduction, what makes its utilization so appealing are its noticeable characteristics.

To begin with, TDLAS allows performing experiments in in-situ conditions. All the measurements can be carried out at the same place and conditions of the real phenomenon. As shown with today's air data measuring instruments, in-situ procedures are preferable since the system is not isolated from its original conditions and so measurements are not altered [8]. As stated above, the working principle of the TDLAS relies on the absorptivity of light by chemical species. Consequently, working in in-situ conditions provides a well defined optical interaction between the laser beam and all the species contained in the medium. Hence, strongly absorbing gases will play an important role in the analysis and will be preferred to be used as "sensor species".

Another point worthy to mention is the open-path structure that TDLAS has. The light beam is directly in contact with the medium, ensuring more reliable and accurate measurements. This advantage is particularly beneficial for the technique's location, as it lets the technique to be placed outside the skin of the body to analyze.

Other characteristic of TDLAS is the type of laser diode that the technique works with. When using tunable laser diodes, the output wavelength of the laser beam can be precisely adjusted. This is a favorable aspect that cannot be achieved with conventional radiation sources. With this property, monochromaticity is ensured. The spectrum of the measured gas is maintained undisturbed by instrumental linewidth contribution while the laser is tuned over the desired molecular absorption line. Moreover, other salient quality that tunable laser diodes have is the small linewidth at which they can operate. This last feature lets the laser diode precisely select the desired gas specie for the measurement, either in pure or trace level of concentration. From this, it can be assumed that the number of laser diodes required depends on the number of species to analyze. Nonetheless, this statement is far from true since one tunable laser diode is able to detect one or couple of substances at once. In relation with the laser diode performance, a change of the laser source allows also a variation in the line intensity. To add to the list, tunable laser diodes can generate large optical path lengths in a specific direction, which can be leveraged for absorptivity measurements in complex circumstances [9].

Finally, regarding the way of performing of the TDLAS, various advantages can be outlined in this section. TDLAS is considered as a non-destructive approach since it does not damage the equipment when performing a measure. By the same token, the samples taken during the experiments are not dependable from each other, reducing the possibility of the appearance of bias errors. Last but not least, TDLAS can operate in real time, responding to the input parameters immediately.

From all these points, it can be concluded that TDLAS is an innovative technique that could be used for pressure measurements.

## 2.4. TDLAS Theoretical Approach

Once TDLAS is presented, theoretical approach to estimate static pressure is described. It consists on two stages, as stated in Chapter 1. Breaking down each one, the first stage is based on the intrinsic calibration of the setup. For the TDLAS analysis, it is required to know the characteristics of the input light intensity signal (Channel 1). This involves the frequency at which the signal is at and the phase evolution over time. To do so, as shown in Section 2.2, an additional path (Channel 2) carrying a percentage of the exact same signal is created. Here, an interferometer is placed. From the absorption of light driven by the temperature at which the laser diode is working at, both phase and frequency from a interferometer's signal are calibrated. With respect to the second stage, a theoretical model based on laser spectroscopy is created. In this model, a correlation between the absorption of light and static pressure is defined. Then, spectroscopy experiments using the calibrated TDLAS are performed, obtaining the three signals at the three channels. By including these output results into the model, the static pressure is estimated.

### 2.4.1. TDLAS Intrinsic Calibration

Recapitulating into the TDLAS setup, the principal reason of designing three channels in the setup is to obtain in each one the quantities necessary for the absorption procedure. From Channel 1, the input intensity of light transformed into electrical current is obtained. In a like manner, Channel 3 gives the output intensity. Although it seems both quantities are sufficient to determine the absorption of light, it is necessary to calibrate the system. For such purpose, the signal from Channel 2 is used.

The calibration procedure consists of the extensive evaluation of each optical device that comprises the setup so the characteristics of the input light beam can be accurately characterized and interferences coming from electronics can be identified. Hence, the calibration of the system relies on the acquisition of frequency and phase evolution.

For this end, a technique called Optical Frequency Domain Reflectometer is used. An OFDR consists of a frequency sweeping tunable laser source (TLS) and an interferometer. As its name states, TLS is a type of laser diode whose wavelength can be modified in a controlled way, being able to sweep in the frequency domain by changing the laser diode's working temperature [10]. The idea behind the calibration is to use one of the TLS to send a light beam by sweep in frequency between two values. The resulting light beam will travel through the three channels. In the case of Channel 2, it will go directly to the interferometer, where an interference is created. Knowing the output frequency of the output signal and the frequency difference in the interference procedure, the input frequency can be estimated. In relation with the phase estimation, the calibration process relies on the absorbance of light. By sweeping in frequency again, two absorption lines are identified. Correlating the position of each line with respect to the signal's phase over two times, the phase sweep is estimated.

Putting theory into practice, the calibration procedure with the current TDLAS setup is carried out. Recalling from Section 2.2, TDLAS actual setup contains two TLS but, for the calibration procedure, just one is needed. In relation with the interferometer, the Fabry Perot interferometer is the one firstly proposed for the procedure.

### TDLAS Calibration: Fabry Perot Interferometer

Fabry-Perot interferometers are commonly utilized in optics to determine at very high precisions the wavelength of a signal. They consist of a pair of parallel mirrors separated by a specific distance. When a beam of incident light at a specific wavelength and with a certain angle with respect to surface reaches the first mirror, a fraction of this light beam passes through it meanwhile the rest is reflected. These amounts are defined by the incident angle and the refractive index of the mirror's material. Similarly, when the transmitted light beam of the first mirror reaches the second one, the same effect takes place. By treating light as an electromagnetic wave, when the incident and reflected light beams coincide at a specific point in space and time, interferences appear. If both waves are in phase, a constructive interference is created and so the output light intensity increases. On the other way around, if waves are out of phase, a darker beam caused by a destructive interference will be at the output [11].

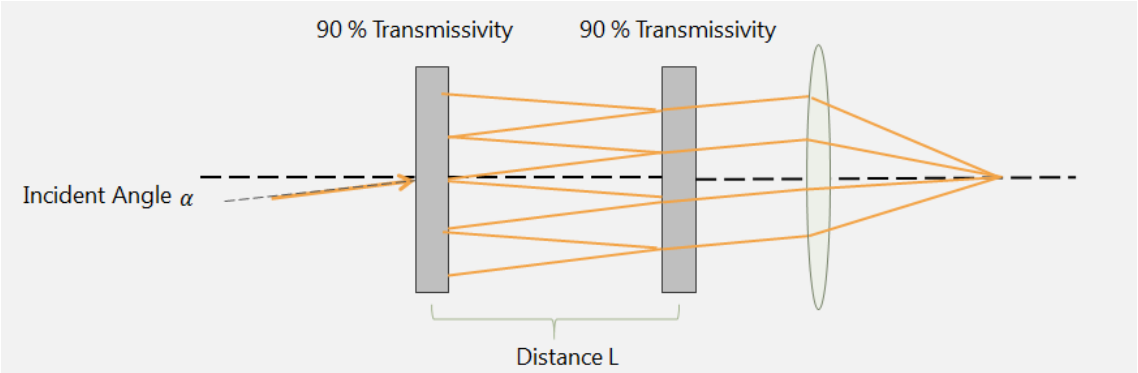


Fig. 2.7. Fabry Perot interferometer

These interferences caused by the Fabry-Perot interferometer are the key parameters to calibrate the TDLAS system. Recapitulating in the calibration procedure, one TLS is utilized. Two temperatures are selected where the absorption of light in oxygen is remarkable. Sweeping between two temperatures, a laser beam with a frequency sweep is sent though Channel 2. After passing the interferometer, with the aid of the photodiode, the signal related with the output beam after the second mirror is obtained. Out of the signal, its phase change and relative frequency are acquired. Then, in relation of the frequency sweep, by knowing mirrors' transmissivity, in this case 90 %, and the distance between them, the frequency sweep $\Delta f$ in the interference process is estimated as [12]:

$$\Delta f = \frac{c}{2L} \tag{2.1}$$

where $c$ is the speed of light and $L$ the distance between mirrors. With the frequency difference just calculated $\Delta f$ and the output frequency $f(t_1)$ obtained beforehand, the input frequency $f(t_0)$ before the interference process is determined.

$$f(t_0) = f(t_1) - \Delta f \tag{2.2}$$

Hence, by knowing this input frequency $f(t_0)$, the TDLAS system is calibrated.

Although it seems a precise approach from which an accurate value of input frequency can be obtained, FP is not the most suitable interferometer to use. One of the drawbacks FP has is the processing of a rapidly tuned TLS. Long delay line or a more complex structure of the FP setup are required [10]. Also, when working with FP interferometers, special attention to its sensitivity must be paid. FP interferometers are highly sensible to changes, as they depend on reflexion of light in mirrors. Manipulation of the optical fibers that are connected to the instrument leads to the distortion of the output signal. Theoretically speaking, even small vibrations affecting the optical fibers are able to cause significant changes in the output value. Misshapen signals will emerge and errors in the calibrations will be induced. In consequence of this fact, it can be concluded that, for a technique that is going to be placed in an A/C where turbulences are abundant, FP interferometers are not the best component to install in.

Thus, a study of the possible substitutes for the FP interferometer has to be conducted. After several propositions, it has been decided that, for the TDLAS, the most convenient interferometer to successfully calibrate the system is the Mach Zehnder Interferometer.

### TDLAS Calibration: Mach Zehnder Interferometer

The working principle of the MZ interferometer relies on the division of the amplitude. Explaining from scratch, a light beam from the TLS goes through an optical fiber (1) until the first optical coupler is reached. Then, the beam is divided in two parts. Half fraction of light flows through an optical fiber (2) meanwhile the other half passes through an optical cable (3). When both halves reach the second optical coupler, they are recombined, which is the actual output light beam (4). The intensity of the output light beam will not be the same as the input intensity but the result of an interference process created due to the paths' length difference. Here, the interference pattern at the output will totally depend on the characteristics of the path that each trace followed. Once the output light beam is obtained, it is then converted into electrical current using a photo-diode [13].

Figure 2.8 portrays the previous explanation in an sketch containing the Mach Zehnder interferometer's design. From the schematics below, it is visualized the two paths the light beams follow as building blocks. Block A is the first optical path comprised by the optical fibers 1, 2 and 4. Similarly, Block B is the second optical path which consists of two optical fibers (1 and 4) and a long optical cable (3).

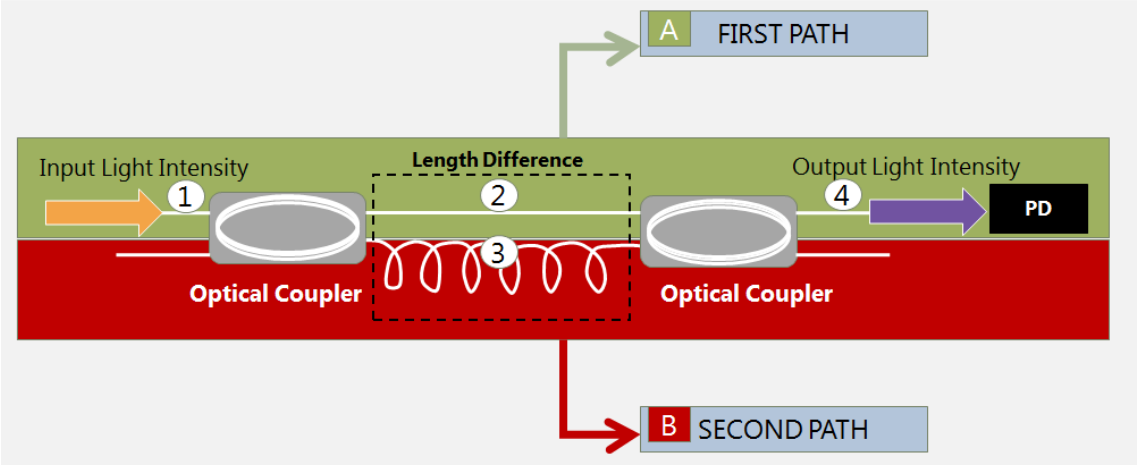


Fig. 2.8. Mach Zehnder interferometer setup

To use the MZ interferometer for the TDLAS calibration, the FP interferometer is removed from the setup and substituted by the former. Figure 2.9 illustrates the TDLAS final architecture. As it can be seen, now Channel 2 contains the electrical signal coming from the Mach Zehnder inteferometer.

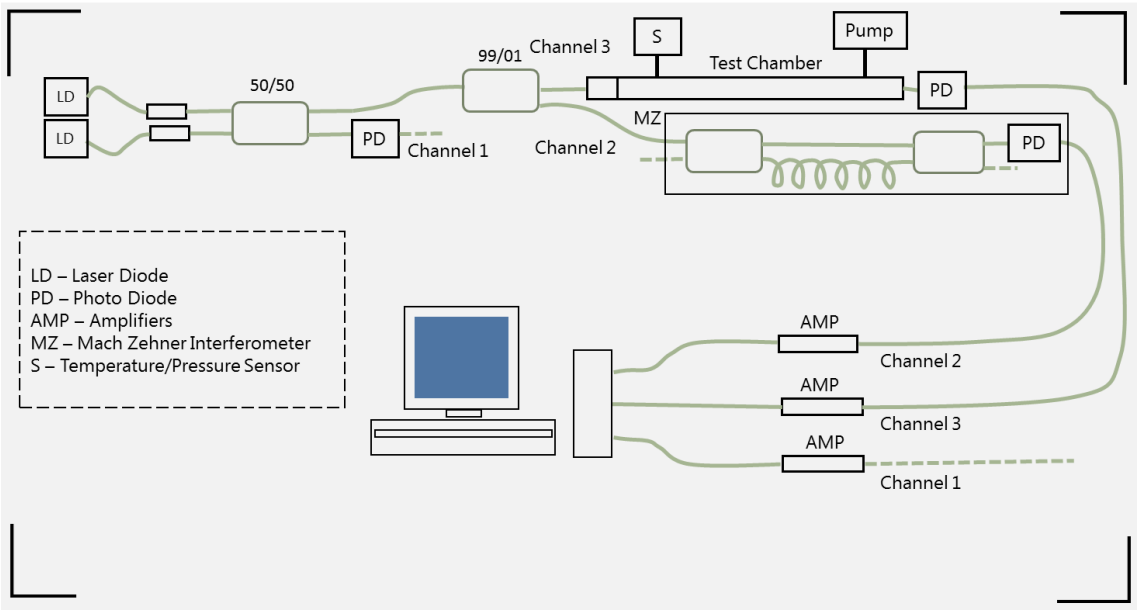


Fig. 2.9. Current TDLAS setup

In terms of calibrating the TDLAS setup, the operating principle of the Mach Zehnder interferometer is very similar to the one from the Fabry Perot. Sweeping between two temperatures, the signal from the light beam with a frequency sweep is obtained from Channel 2. Knowing its output frequency and the difference in frequency due to the interference created at the Mach Zehnder interferometer, the frequency of the input signal can be computed. In addition, from the temperature sweep, the signal's phase over time is similarly estimated and from it, the TDLAS setup is calibrated.

Therefore, just for recapitulation, the TDLAS calibration process relies on the analysis

of the signal from Channel 2. As stated above, the parameters that characterize the signal and so are the drivers for the calibration system are: the phase evolution over time and the change of frequency through time. Furthermore, as it will explain later, in order to validate the calibration from both parameters, a third magnitude is estimated: the optical length difference of the Mach Zehnder interferometer.

Retrograding to the first value for analysis, the first parameter required is the change of the output light beam's phase over time. The idea behind this phase sweep estimation is to correlate it with another controllable and known magnitude that can be swept in time. Basically, the desired output is not one discrete value but an evolution over time. From theory, this phase evolution is rising monotonously, so just two values are needed for the estimation. Therefore, for the sake of simplicity, another magnitude described by a linear regression is needed. This magnitude is the Laser Diode (LD) temperature. By definition, in a spectroscopy experiment, the appearance of absorption lines in a molecular spectrum mainly depends on the input settings at which the LD is working at. These are the wavelength, current and temperature. Banking on the values of each parameter, unique absorption lines emerge. So, selecting the LD temperature as the reference value and identifying two proper values in which two noticeable absorption lines are created at a fixed current, the phase sweep can be procured from this temperature sweep. The detailed iterative process for the phase computation is illustrated in the diagram below.

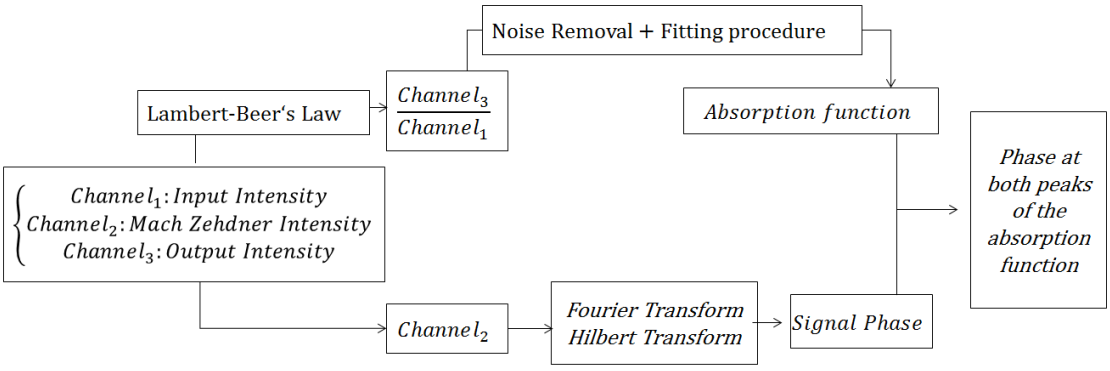


Fig. 2.10. Phase calculation diagram

Breaking down the schematics presented in Figure 2.10, phase sweep is fundamentally dependent of the output signals from Channel 1, 2 and 3. From Section 2.2, Channel 1 contains the signal related with the input intensity of the light beam at the laser diode; Channel 2 the signal from the output intensity of the light beam after the interferometer process with the Mach Zehnder; and Channel 3 the signal from the output intensity of the light beam after the absorption procedure. To obtain the three signals, one spectroscopy experiment at a variable laser diode temperature is performed. This change in temperature in time leads to the extraction of two absorption lines at each selected temperature, being the output from Channel 3. Then, making the correlation between signals from Channel 1 and Channel 3 following the Lambert-Beer's equation, both absorption lines are included

into a single absorption function (upper path of the diagram). With respect to the signal from Channel 2, its phase through time is estimated by applying the Fourier and Hilbert transform (lower path of the diagram). Finally, identifying the position in time of each absorption line in the phase function, the phase sweep is predicted.

Regarding the signals' processing, an important aspect to take into consideration for this process is the fulfillment of Nyquist sampling theorem. In principle, when passing a signal from analog to digital, a specific number of points is required to represent the signal. Therefore, the Nyquist sampling theorem states the sampling frequency has to be at least two times the highest frequency contained in the signal, so the appearance of aliasing effects can be avoided [14]. So, to successfully calibrate the system, an oscilloscope is utilized to prove the satisfaction of the theorem and to obtain the intensity signals with an unique patron of frequencies in each channel.

For the absorption function estimation, Lambert-Beer law is applied. By definition, the output light intensity after the absorption process $I$ is proportional to the input light intensity from the laser diode before the absorption process $I_0$. This proportionality relies on the dimensions of the test chamber where the air is kept, more specifically on its length $L$. Thus, the Lambert-Beer's equation is written as [15]:

$$I = I_0 e^{-\alpha L} \tag{2.3}$$

Rearranging Equation 2.3, the absorption coefficient $\alpha$ is proportional to the ratio between the output and input light intensities:

$$Ln\left(\frac{I}{I_0}\right) = -\alpha L \tag{2.4}$$

Putting names into labels, the initial ($I_0$) and resulting ($I$) light intensity are derived from the signals of Channel 1 and Channel 3. For the sake of simplicity, the absorption function is not going to be defined as the absorption coefficient but as the multiplication of the two last parameters mentioned. Thus, with Equation 2.4, the absorption function containing the two absorption lines is estimated.

Although the setup components have been evaluated so they can have an optimum performance, the absorption function can be affected by background noise. To reduce this source of distortion and filter out the unnecessary data, noise reduction filters are implemented in the analysis. Low pass filters (LPF) are commonly used in optics to block frequencies higher than the cut-off frequency. Therefore, just signals with frequencies lower than the cut-off frequencies are allowed to enter into the system. By making use of the LPF, the absorption signal is cleaned. In addition, in order to obtain the most accurate position in time of the absorption lines inside the absorption function, both absorption lines are fitted with a Voigt profile. For such purpose, firstly the absorption function is splitter into two halves, so each absorption line can be treated separately. Although a more detailed description of the fitting is presented in Section 2.4.2, Voigt profiles are

defined by its width, amplitude and center location. Introducing into the fitting widths of absorption lines as well as amplitude and center location, the absorption function is fitted.

Once the absoption funcion is completely defined, it is used to determine the phase the signal has at each one of the absorption lines. Way back to the diagram for the phase computation (Figure 2.10), the methodology utilized to do this evaluation relies on the frequency at which the Mach Zehner interferometer's signal is at [1]. To obtain this value, let's assume the output signal received from the MZ interferometer is governed by this simple expression:

$$y(t) = y_0 \sin(\phi(t) - \phi(t - \tau) + \epsilon_0) \tag{2.5}$$

where $y_0$ is the signal's amplitude, $\phi$ is the light beam's phase, $\tau$ is defied as the group delay due to the path difference of the two arms in the interferometer and $\epsilon_0$ is the phase of the signal. Using the Taylor expansion to treat the term $(\phi(t) - \phi(t - \tau))$ and assuming a short ground delay, the term can be reduced as

$$(\phi(t) - \phi(t - \tau)) = \tau \frac{d\phi(t)}{dt} + \tau^2 \frac{d^2\phi(t)}{d^2t} = 2\pi\tau v(t) + 2\pi\tau^2 = 2\pi\tau v(t) \tag{2.6}$$

Being $v(t)$ the frequency of the input light intensity signal. Substituting the output from Equation 2.6 in 2.5, the expression is simplified to:

$$y(t) = y_0 \sin(2\pi\tau v(t) + \epsilon_0) \tag{2.7}$$

The output signal of the interferometer is governed by Equation 2.7. To determine its frequency, the Fourier transform is employed. By definition, the Fourier transform is a tool that decomposes the signal into its constituents frequencies. It can be represented as the following definite integral:

$$F(x(t)) = \int_{-\infty}^{+\infty} y(t) e^{-j2\pi vt} \delta t \tag{2.8}$$

where $v$ implies the translation into the frequency domain.

From the FT, the Hilbert transform is evaluated. Theoretically, the HT of a function is the convolution of the Fourier transform with the signal $1/\pi$t [17]. In substance, it is a linear operator that shifts the phase of each one of the frequencies from the Fourier transform by 90 °. Therefore, the Hilbert transform of the output signal in the MZ interferometer is expressed as:

$$HT(y(t)) = y_0 \cos(2\pi\tau v(t) + \epsilon_0) \tag{2.9}$$

[1] Procedure explained in detail in [16]

The combination of the Hilbert transform (HT(y(t))) with the real output signal from the MZ (y(t)) gives the value of the phase in time of the output signal ($\theta$(t)).

$$\frac{y(t)}{HT(y(t))} = \frac{y_0 \sin(2\pi\tau v(t) + \epsilon_0)}{y_0 \cos(2\pi\tau v(t) + \epsilon_0)} \rightarrow \frac{y(t)}{HT(y(t))} = \tan(2\pi\tau v(t) + \epsilon_0) \tag{2.10}$$

Assuming the $\epsilon_0$ is set to 0 and using the cotangent, the phase unwrapped over time is:

$$\theta(t) = \arctan\left(\frac{y(t)}{HT(y(t))}\right) = 2\pi\tau v(t) \tag{2.11}$$

Effectively, connecting this phase evolution $\theta(t)$ with the absorption function previously estimated, the phase of the Mach Zehnder interferometer's signal at each one of the absorption lines is approximated.

Continuing with the TDLAS calibration procedure, the second parameter needed is the change of output light beam's frequency over time. Recalling from the phase sweep estimation, the laser diode's performance is described by the combination of its working temperature, wavelength and frequency. Keeping again fixed the value of current, a temperature-wavelength relation is acquired. Replacing the same values of the two temperature selected for the phase sweep computation into the equation that defines this relation, the wavelength the laser diode has at each temperature is computed, and so, the frequency sweep [16]. Lastly, for the sake of accuracy, results are introduced into HITRAN on the web for comparison. This last is a website which contains information about spectral line parameters of atmospheric gases and pollutants [18]. Thus, once again, a schematics of the described procedure is shown in Figure 2.11.

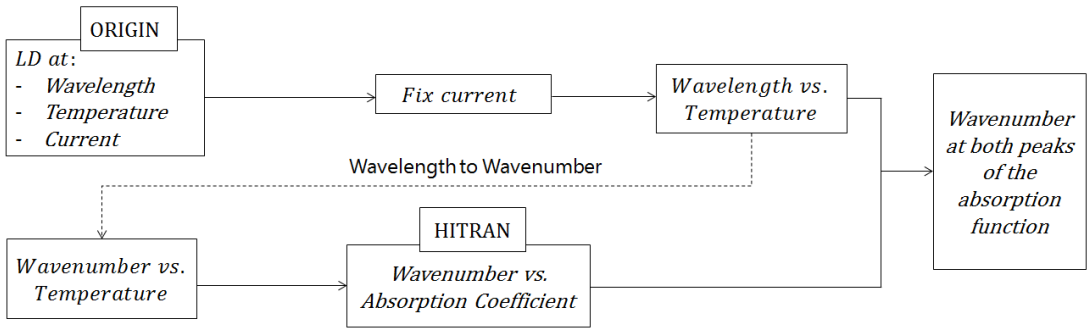


Fig. 2.11. Frequency calculation diagram

Finally, to validate and verify the TDLAS indeed is accurately calibrated as specified, the optical length difference of the Mach Zehnder interferometer is studied. The optical length difference is the difference between the two optical paths that the interferometer has, expressed in length units. From the Mach Zehnder design shown in Figure 2.8, it can be visualized in each block the optical path followed by the light beam. Although each optical fiber has its own uncertainty in its length, a robust estimation of the optical path

difference can be determined. A commonly used approximation for the optical length difference that takes relatively little calculation time is [16]:

$$\Delta L = \frac{1}{2\pi n}\frac{c}{v(t)}\arctan\left(\frac{y(t)}{HT(y(t))}\right) \rightarrow \Delta L = \frac{1}{2\pi n}\frac{c}{v(t)}\theta(t) \tag{2.12}$$

where $\Delta L$ is the length difference between the two paths in the MZ interferometer, c is the speed of light in vacuum conditions, n is the refractive index of the optical fiber and $\theta(t)$ and $v(t)$ are both the phase and frequency sweep in time previously estimated.

### 2.4.2. TDLAS Pressure Estimation

Pressure estimations can only be conducted once the TDLAS setup is completely calibrated. From this point forward, the forthcoming subsection describes the approach for spectroscopy, in flight, airflow static pressure determination with the TDLAS technique.

TDLAS is defined as a novel and promising alternative for pressure measurements. It relies on the principle that static pressure can be estimated from optical spectroscopy. Theoretically speaking, TDLAS proves that the absorption of light is correlated with the absorption line width and so with the static pressure. Although the theoretical principle may appear simple, a deep analysis is required in order to achieve this output.

To begin with, let's review Figure 2.2 which contains the TDLAS setup. As previously defined in Section 2.2, a light beam of 99 % of intensity is going to enter into the test section, where air is kept. The presence of the specie will lead to the absorption of a fraction of the light. For all the experiments, molecular oxygen is the "sensor specie". This selection was made due to the fixed high concentration of oxygen in air over the full range of atmospheric conditions, leading to noticeable amounts of light absorbed in any of the represented cases. Processing both input and output light intensities after the absorption with the photodiodes, intensity is converted into electrical current. Then, again, by making use of the Lambert-Beer law (Equation 2.4), the absorption function is estimated.

As defined in Section 2.2, the amount of light absorbed inside the test chamber directly depends on the combination of the laser diode settings and the characteristics (pressure, temperature and chemical composition) of the analyzed specie inside the gas cell. These parameters are the principal drivers for modeling the absorption line in the absorption function from the spectroscopy experiment.

Recent studies have demonstrated the width of the absorption line is influenced by the specie's characteristics. Both temperature and pressure are proportional to the line broadening [2] . It means that with the variation of the value of either pressure or temperature, the absorption gets wider or narrower. Concerning the chemical composition, it can be

[2]Procedure followed hereafter is fully explained in [19]

neglected since no chemical reactions occur in the absorption process and so, its value remains constant with respect to the broadening effects.

The influence of the temperature in the line broadening comes from the Doppler effect. When light enters into the gas cell, photons are absorbed by the air, reaching an excited state. Because each molecule of $O_2$ is moving in a different direction inside the cell, a small Doppler-shift frequency will be created and so a line broadening will arise. This line broadening will follow a Gaussian distribution. Increasing the gas temperature, the air particles will be more excited and so a higher broadening will occur, broadening the absorption line [20]. On the other way around, narrower line broadening will occur when dropping the temperature of the gas.

Therefore, the absorption line width in terms of Doppler broadening from temperature contribution can be written as:

$$\gamma_{Doppler} = \left(\frac{v_0}{c}\right)\sqrt{\frac{2kTN\ln(2)}{m}} \tag{2.13}$$

where $v_0$ is the frequency of the laser diode, c is the speed of light, k is the Boltzmann constant, N is the Avogadro number, T is the ambient temperature and m is the molecular mass of the specie. For the sake of simplicity in the analysis, all the experiments will be performed at a fixed temperature (fixed $\gamma_{Doppler}$), so a better understanding of the pressure influence into broadening of the absorption line can be achieved.

The influence of pressure in the line broadening comes from the collisions between atoms inside the chamber. When increasing concentration of gas in the test section, more molecules are presented in the cell. The probability of collisions between the molecules is higher and so the value of the pressure. On the contrary, when emptying the test cell, lower amount of substance is kept inside and so the probability of collisions is lower, being the value of pressure lower too. One effect of these collisions is their interference with the natural emission process, altering the direction and velocity of the molecule. Basically, higher number of collisions will lead to a broader range of frequencies from the molecule' interactions and so wider absorption lines. Quite the opposite, less collisions will mean narrower absorption lines. Another consequence due to molecular impacts is the sporadic release of photons from the atom' structure. Relevant to this issue, the state of the atom can be completely modified, reaching ground state from the excited one.

Thus, summing up, pressure is the main driver that defines the width of the absorption line from the collisional broadening [20]. Therefore, from pressure, the half width half maximum of the absorption line profile can be empirically expressed as:

$$\gamma_{Lorentz} = \left(\gamma^0_{Lself}p_{self} + \gamma^0_{Lforeign}p_{foreign}\right)\frac{1}{P_0}\left(\frac{T_0}{T}\right)^n \tag{2.14}$$

where $p_{self}$ is the oxygen pressure, $p_{foreign}$ are the remaining species inside the test chamber, $\gamma^0_{Lself}$ and $\gamma^0_{Lforeign}$ are the broadening coefficients from HITRAN website and T

is the ambient temperature. The factors $P_0$ and $T_0$ are used to convert the pressure and temperature units to atm and Kelvin, respectively and thus, to scale the value of $\gamma_{Lorentz}$. Parameter n defines the temperature dependence of the collisional broadening for that specific absorption line. Rearranging Eq. 2.14 by replacing the partial pressures with the molecular oxygen concentration $C_{O2}$ combined with the total gas pressure $p$ :

$$\gamma_{Lorentz} = p\left(\gamma^0_{O_2 self} C_{O_2} + \gamma^0_{Lforeign}(1 - C_{O_2})\right) \frac{1}{P_0} \left(\frac{T_0}{T}\right)^n \tag{2.15}$$

and thus isolating the total pressure in the left hand side:

$$p = \frac{\gamma_{Lorentz} P_0}{\left(\gamma^0_{O_2 self} C_{O_2} + \gamma^0_{Lforeign}(1 - C_{O_2})\right)\left(\frac{T_0}{T}\right)^n} \tag{2.16}$$

A expression for the static pressure estimation is found. Taking a close look into Eq. 2.16, $p$ and $\gamma_{Lorentz}$ are unknown. An approximation of the Lorentz HWHM has to be established beforehand so the pressure can be estimated. As previously mentioned, both collision and Doppler broadening mechanisms are convoluted in a shape function called Voigt profile. This profile represents in its entirely totality the shape of an absorption line, governed by $\gamma_{Doppler}$ and $\gamma_{Lorentz}$. Therefore, keeping this idea in mind, the absorption function from the experiment is going to be fitted into a Voigt profile. Fixing the value of $\gamma_{Doppler}$, an iterative process computing the Voigt profile is done so $\gamma_{Lorentz}$ can be estimated from these two parameters. Then, with the $\gamma_{Lorentz}$ obtained, the static pressure is estimated using Eq. 2.16. Here is presented a schematics of the iterative process for the pressure estimation:

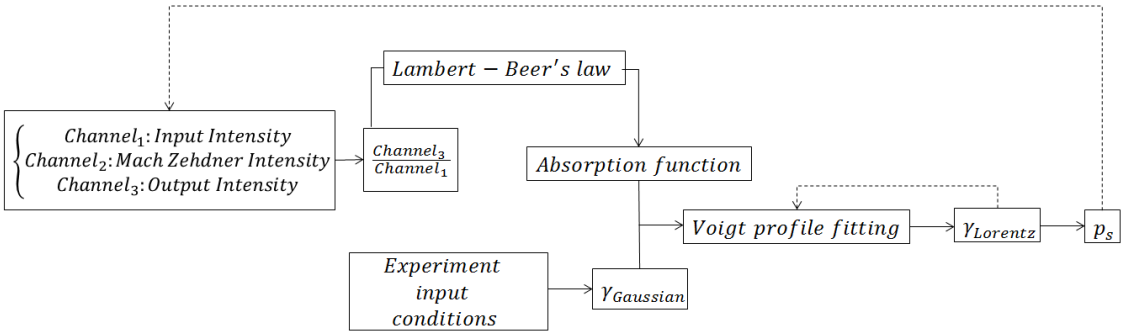


Fig. 2.12. Static pressure estimation diagram

Finally, once static pressure is approximated, the altitude at which the aircraft is flying at can be easily approximated isolating the term from the barometic expression [21]:

$$p = P_0 exp\left(\frac{mgz}{kT}\right) \tag{2.17}$$

where m is the molecular mass of oxygen, g is the value of gravity, z is the altitude and T is the temperature at that altitude, obtained from $T = T_0 - 6.5x10^{-3}z$

# 3. EXPERIMENTS AND RESULTS

## 3.1. TDLAS Intrinsic Calibration

### 3.1.1. TDLAS Calibration: Mach Zehnder interferometer

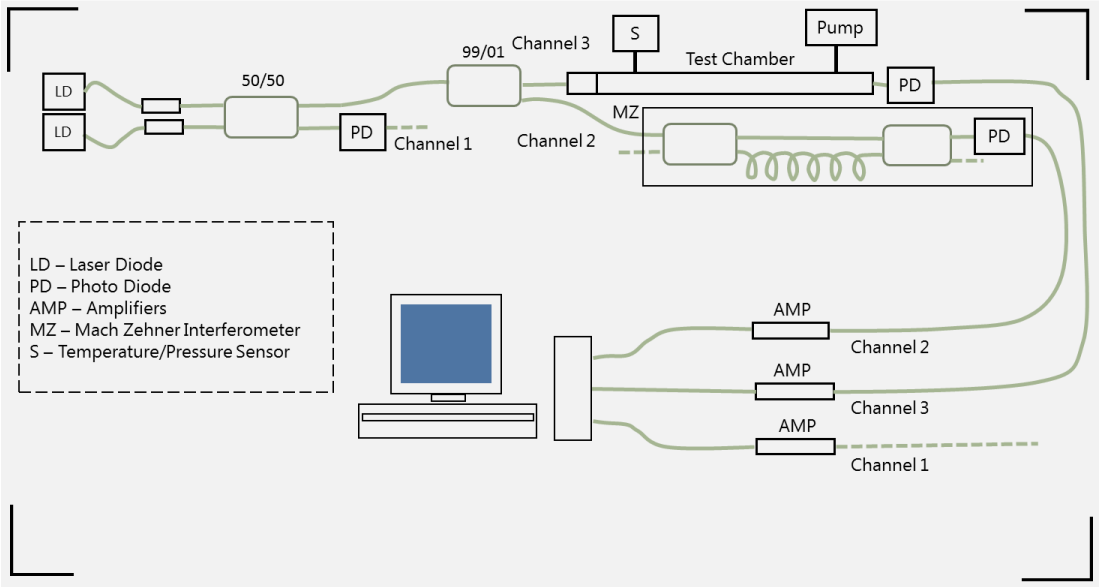


Fig. 3.1. TDLAS final setup

For the TDLAS setup calibration, one spectroscopy experiment is performed. For the sake of simplicity, air inside the test chamber is at ambient temperature (23 °C) and ambient pressure (0.96 atm). Regarding the laser diode input settings, the current is kept fixed with a value of 75 mA. To select the laser diodes temperatures, an oscilloscope is utilized. The oscilloscope settings are 20 MHz of bandwidth, an horizontal sweep of 1.00 s per division (s/div), a vertical deflection of 200 mV per division (mV/ div), an offset of -500 mV and DC coupling of 50 ohm. By changing the laser diode's temperature with a thermoelectric controller (TEC) and analyzing with the oscilloscope the appearing oxygen absorption lines in a temperature range, two suitable lines are selected. From them, their respective temperatures, which are found to be 22 °C and 26 °C. As soon as the temperatures are defined, one spectroscopy experiment is performed with a forward sweep of these temperatures (from 22°C to 26°C). The experiment lasts 4 seconds and from it the light intensities as electrical current at each one of the three channels are acquired. To acquire the results, the adlink program is utilized.

The absorption function is estimated via the Lambert - Beer's equation. Recalling Section 2.4.1, by substituting into the equation the input intensity $I$ from Channel 1 and output intensity $I_0$ from Channel 3, the absorption function is directly estimated. Figure 3.2 shows the computations discussed above. On the left hand side (Figure 3.2 a), a

graph of both input and output light's intensity functions is plotted. Recapitulating from Section 2.4.1, just 50 % of the light beam from the Laser Diode is actually involved in the experiment, being this the reason of why the output intensity light has greater value than the input. Also, it can be easily identified in this plot the two absorption lines at the two temperatures when sweeping up in temperature during 4 seconds. In addition, it can be seen a drop in intensity, leaded by the frequency sweep when doing the temperature sweep. In conjunction with the previous graph, the plot at the right hand side corresponds to the absorption function (Figure 3.2 b). Recapitulating from 2.4.1, absorption is the amount of light absorbed by a medium, being between 0 and 1. Thus, normalizing results from this plot, a value strictly located at that interval will be found.

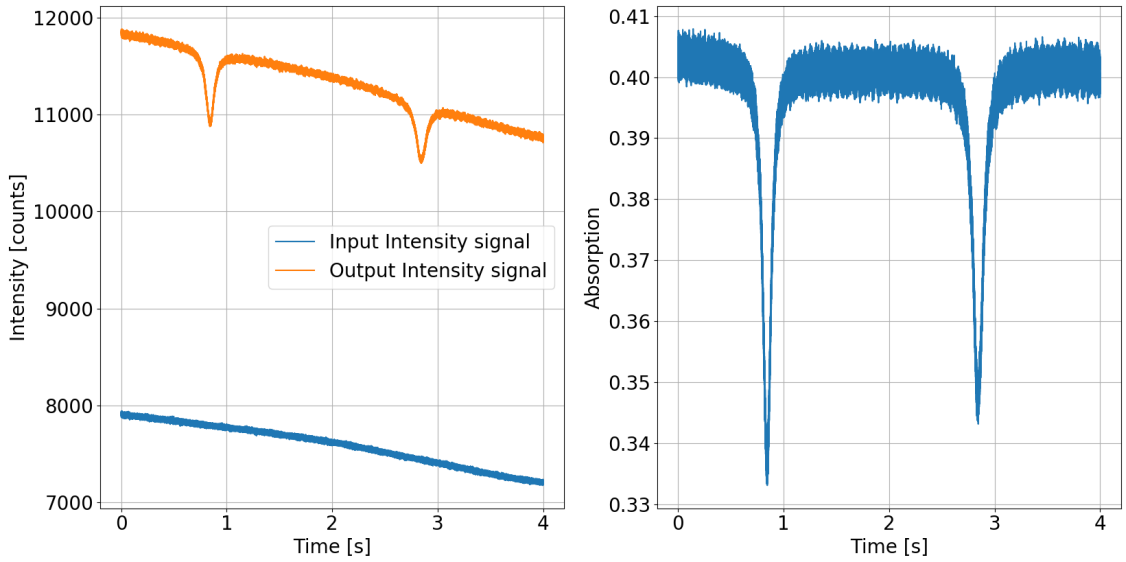


(a) Output and input intensities

(b) Absorption function

Fig. 3.2. Mach Zehnder Calibration: temperature sweep up

As shown in the Figure, both signals contains some background noise. To reduce the noise, a low pass filter is utilized. In addition to this, both absorption lines are fitted separately into Voigt profiles. From theory, a Voigt profile is the convolution of a Gaussian and a Lorentzian profile. Thus, it is defined by the following characteristics: Gaussian width, Lorentzial width, Voigt's amplitude (area inside the curve), Voigt height (altitude of the Voigt profile), center location and inclination with respect to the horizontal plane. To develop the fitting procedure, the values of both centers and the Voigt inclination are fixed, following the Voigt profile shown in Figure 3.2. Hence, an iterative process fitting all the remaining parameters is carried out. Figure 3.3 shows both Voigt profiles fitted in each one of the lines.

As illustrated in the Figure, both Voigt profiles are accurately adjusted to the real absorption lines. For a clearer comparison, results have been normalized. Moreover, to develop the fitting, the center of each absorption line has been fixed and set in 0. The main reason behind this is to have an easier understanding of the width variation with

respect to the height in terms of symmetry. Hence, Figure 3.3a and 3.3b illustrates the above explanations graphically.

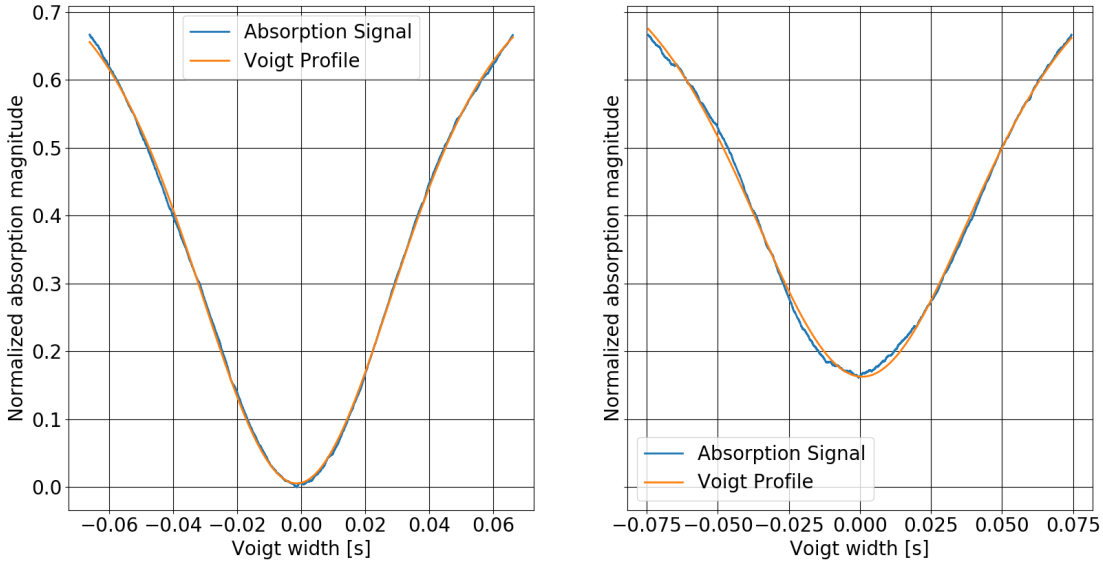


(a) Fit of the first absorption line

(b) Fit of the second absorption line

Fig. 3.3. Absorption function fitting

Then, replacing each Voigt profile into its respective absorption line, the absorption function is attained. Figure 3.4 contains three graphs with the aforementioned results.

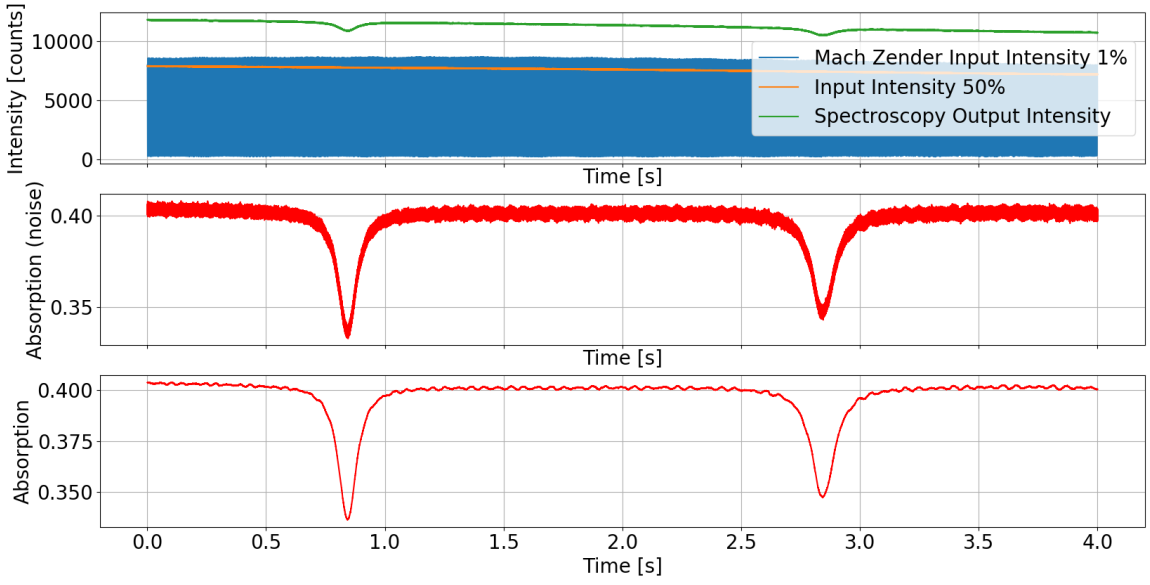


Fig. 3.4. Upper graph (a): Channel 1, 2 and 3 signals; Middle graph (b): absorption function from Lambert-Law equation; Lower graph(c): filtered and fitted absorption function

In the upper plot (Figure 3.4a), the three intensities of the three signals are shown; the green function corresponds to the output signal, the orange one to the Mach Zehnder signal and the blue one is the intensity of the input signal. With respect to Figure 3.4b

(middle one), the absorption function as a directly result of the ratio between the output and the input intensities is displayed. Belatedly, the function in which both noise filter and Voigt profiles are incorporated is presented in Figure 3.4c. A zoom-in of the first absorption line is also plotted separately to clearly visualize the signals' behavior through time.

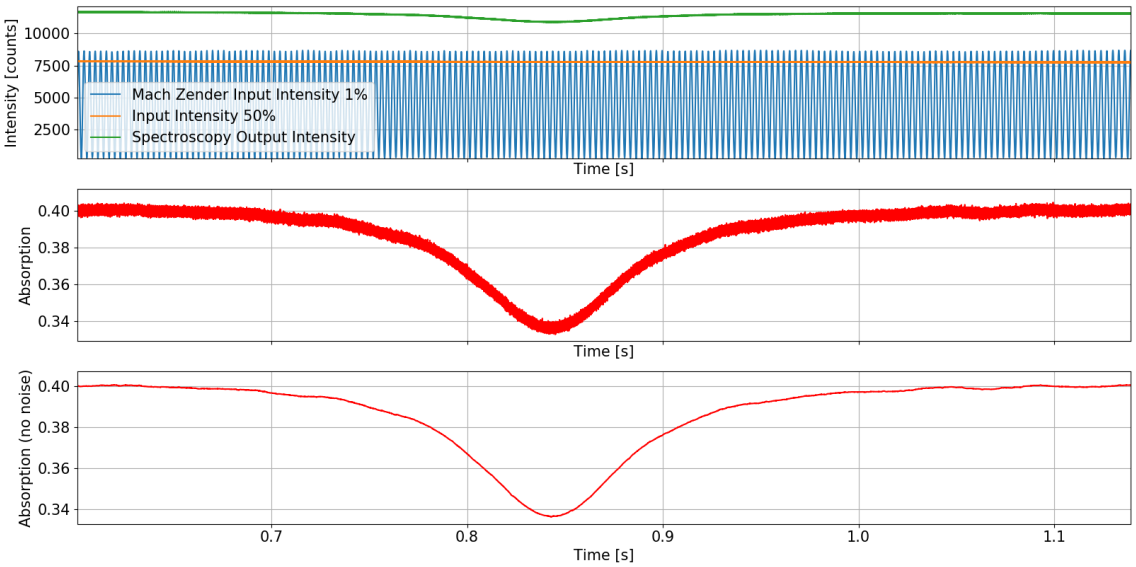


Fig. 3.5. First absorption from Figure 3.4 line zoom-in

Following the schematics presented in Figure 2.10, the Mach Zehnder interferometer signal's frequency is processed. Applying the Fourier transform, a range of frequencies between 240 to 380 Hz is found.

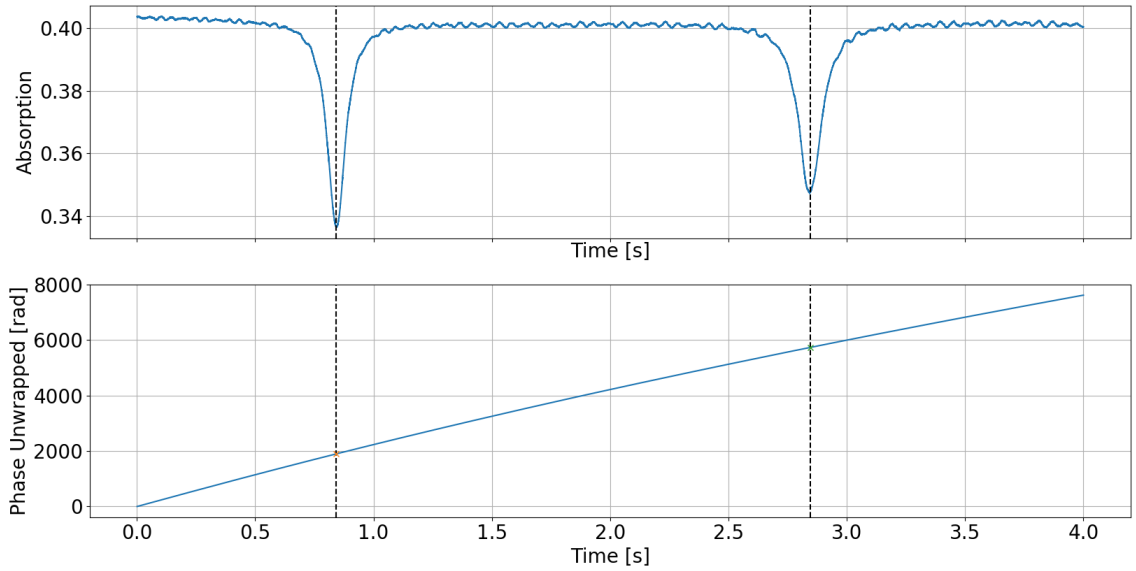


Fig. 3.6. Phase unwrapped in time: determination at each absorption line

Then, by shifting each one of the frequencies by $\pi/2$, the Hilbert transform expressed in a sine wave form is estimated. Introducing both output signal from the MZ (y(t)) and the

signal obtained from the Hilbert transform HT(y(t)) into Equation 2.11, the unwrapped phase evolution in time of the MZ signal is found, identifying "unwrapped phase" as a parameter obtained from the constant addition of the phase change through time. For the 4 seconds experiment, this value goes up from 0 up to 7610.54 rad (Figure 3.6).

Finally, the MZ signal's phase at each one of the absorption lines is determined. To obtain the exact value, the first derivative of the absorption function is utilized, so both minimums are accurately known. Summarizing the results, at the first absorption line (corresponding to the time 0.84 seconds), the phase value is 1896.04 rad meanwhile at the second absorption line (time value of 2.84 seconds), the value is 5726.38 rad, as displayed in Figure 3.6. Therefore, the resulting phase sweep is 3830.34 rad.

Once the phase sweep is defined, it is proceed to determine its relative frequency sweep. To obtain such value, the same input conditions assumed for phase computation are employed: just one laser diode, in this case LD368, working at a fixed current of 75 mA and specific ambient conditions (23 °C and 0.96 atm). Following the guidelines from Figure 2.11, the dependence between characteristics of the laser diode (current, temperature and wavelength) is established. With an Optical Spectroscopy Analyzer (OSA), these relations are approximated. Figure 3.7 graphically illustrates the quantities' relation. The interpretation of the Figure provides the upper and lower limits of operation of the laser diode. The LD368 works at wavelengths between 760.2 to 761.5 nm, in a current range from 50 to 110 mA and with a temperature sweep of almost 18 °C (15°C to 32.5°C).

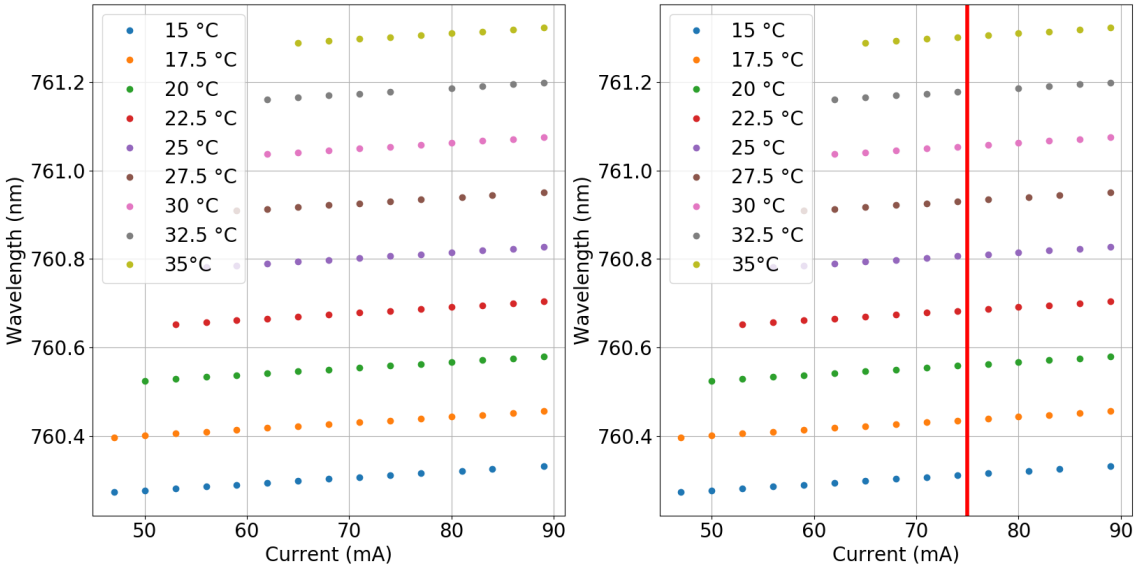


(a) Correlation between LD's characteristics (b) Fixing current: temperature vs. wavelength

Fig. 3.7. LD characteristics measured with OSA

From its apparent simplicity, it can be concluded from Figure 3.7 that wavelength and current are correlated in a way that follows a direct linear regression. Higher currents lead to higher wavelengths. Similar conclusion can be drawn from their correlation with the temperature. Increasing the working temperature of the laser diode, higher wavelengths

are achieved. Nevertheless, if both relations are closely examined, the regressions are not entirely linear. Inaccuracies in the temperature values and the unbalance between the working mechanism in the setup lead to small offsets in the resulting values. As an example, the linear regression between the temperature and the wavelength has offsets in each one of the values in the order of magnitude of 0.01 nm. These offsets are represented as oscillations along the linear regression. Nonetheless, for the purpose of this master thesis, a linear regression between magnitudes is assumed.

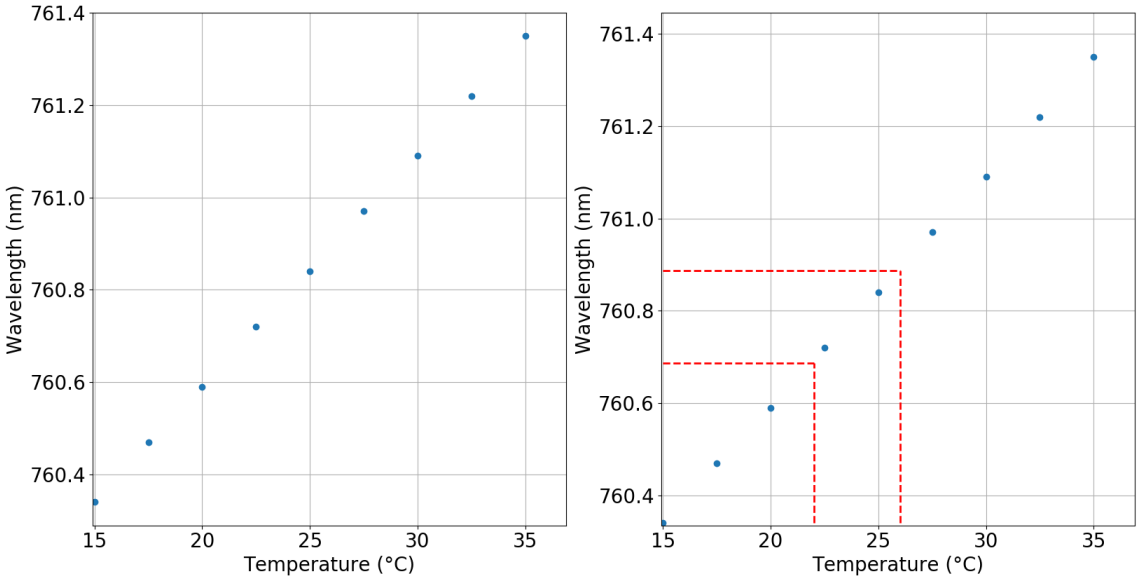


(a) Correlation between temperature and wavelength (b) Wavelengths estimation from temperature

Fig. 3.8. LD characteristics: Temperature vs Wavelength

Making use of the 75 mA of current fixed for the whole procedure and substituting it into the current-temperature-wavelength relation, direct correlation between wavelength and temperature is found (Figure 3.7b). The resulting plot gives a smooth linear correlation between the two temperature and wavelength variables. The equation for the line regression in point-slope form is $y = 0.0503x + 759.59$, being "x" the temperature (°C) and "y" the wavelength (nm), with a R-squared of 0.999. Again, because of the desirable output is a sweep in one magnitude, in this case frequency, and a linear relation between magnitudes is assumed, two values of temperature have to be used. On the basis of the two temperatures of the two absorption lines T = 22°C and 26°C postulated for the signal's phase computation, wavelengths equal to 760.69 nm and 760.89 are estimated.

To prove the accuracy of the wavelength results, the simulator in HITRAN on the web is utilized. As the input parameters, the minimum and maximum values of the wavelength just computed are introduced. An important remark is that information in HITRAN is in wavenumbers, so a previous conversion is required. From the wavelength values reported above, wavenumbers of 13145.94 $cm^{-1}$ and 13142.45 $cm^{-1}$ are estimated. Introducing these values into the simulator and establishing measurement is performed at ambient conditions (assuming ambient conditions as 0.96 atm and 23 °C), the location of the two

absorption lines in the frequency domain is established. Again, absorption function's derivative from HITRAN that includes both lines is computed so to accurately define the value (in wavenumber) at each absorption line location. Finally, the output results are 13144.53 $cm^{-1}$ and 13146.56 $cm^{-1}$. Converting into frequencies (Hz) by multiplying with the speed of light, the outputs are 394396.97 GHz and 394336.00 GHz, being the frequency sweep 60.97 GHz.

To sum up, the presented phase sweep 3831.03 rad and frequency sweep 60.97 GHz are exclusively to calibrate the TDLAS technique. The ratio between both magnitudes gives the calibration parameter, 0.0159 GHz/rad. This parameter will be used afterwards to calibrate the system into the frequency domain

Just to finish, to validate the calibration procedure, the optical length difference is computed. Replacing into Equation 2.12 both phase and frequency sweep and assuming the optical fiber has a refractive index of 1.454 and the speed of light is approximately $3x10^8$ m/s, the value of the optical length difference is equal to 2.059 m.

To confirm whether the obtained outputs are consistent with the expected results, same process is repeated but this time sweeping down in temperature (from 26 ° C to 22 ° C). Recapitulating to the phase computation, the two same absorption lines in a time interval of four seconds are selected. Using a LPF to filter the noise and a Voigt profile to fit the absorption lines, the absorption function from Channel 3 and Channel 1 is estimated. Then, with the Fourier Transform and the Hilbert Treansform, the phase from the MZ interferometer's signal is computed. Lastly, the phase sweep between each absorption line is estimated, being in this case 3718.04 rad. Likewise, the frequency sweep from the temperature and wavelength relation is found to be the same 60.97 GHz, obtaining a calibration parameter of 0.0163 GHz/rad. Substituting the calibration parameter in Equation 2.12, the optical length difference is equal to 1.999 m.

Table below contends all the calculated calibration parameters from both approaches:

| $\Delta T$ (°C) | $\theta(t)$ (rad) | $v(t)$ (GHz) | Calibration Paramater (GHz/rad) | $\Delta L$ (m) |
|---|---|---|---|---|
| 22 to 26 | 3830.34 | 60.97 | 0.0159 | 2.059 |
| 26 to 22 | 3718.04 | 60.97 | 0.0163 | 1.999 |

Table 3.1: TDLAS Calibration Parameters

In spite of minor disagreement, both processes have the same order of magnitude in the three values. Nonetheless, the optical length difference varies in a 0.06 m (60 mm). The cause of this controversy comes from the variation in the calibration parameter, and so in the phase and frequency sweep estimation. A minor change in the beam's intensity caused by the mechanism of the laser diode when sweeping up or down in temperature can be a possible cause of this small offset. Other possible source of error can be related with the different performance of the electronics during warming up and cooling down the system. Although the apparent cause is probably more related with the two effects

previously mentioned, physical effects are neither discarded. Notwithstanding the controversy in results, for the TDLAS calibration, just one direction in the temperature sweep will be perfomed i.e sweep up.

### 3.1.2. TDLAS Calibration: Interferometers comparison

To conclude, it has been proved the viability of calibrating the TDLAS system using the MZ interferometer. Nevertheless, as stated in Section 2.4.1, the FP interferometer was another possible tool for such procedure. Thus, before completely discarding this last interferometer, it is appropriate to support this deselection with a comparison against the Mach Zehnder interferometer.

Recalling from Section 2.4.1, the high sensitivity and structural complexity of the Fabry Perot interferometer make inadequate its utilization for calibration purposes. To support these arguments, both interferometers are incorporated into the TDLAS setup. For this purpose, the TDLAS setup has to be rearranged, as shown in Figure 3.9.

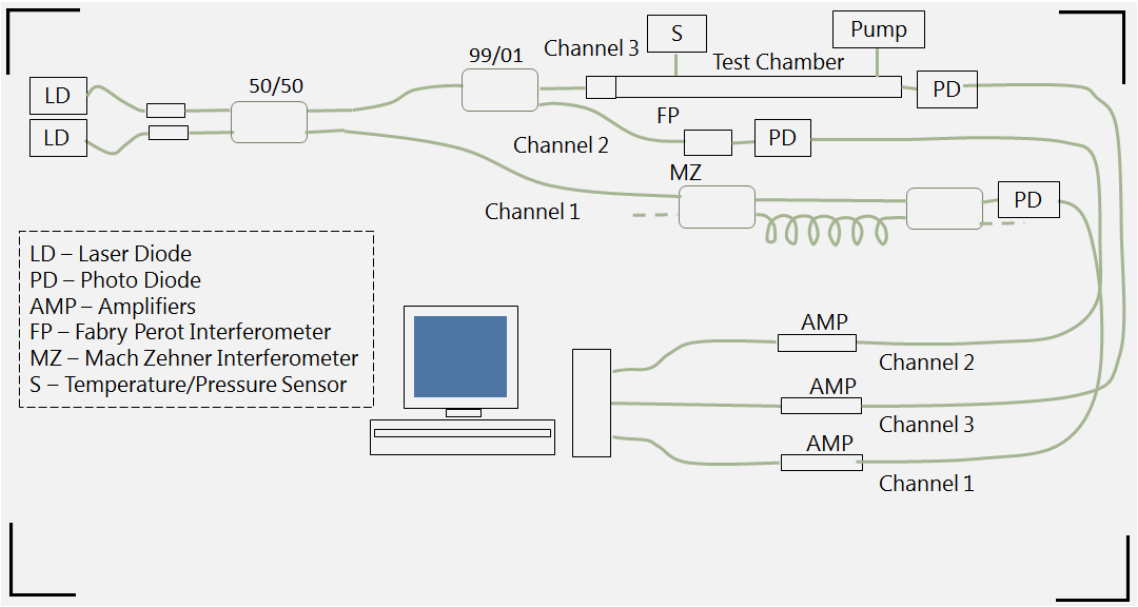


Fig. 3.9. TDLAS setup for interferometer comparison

In this new arrangement, the three-channels configuration is kept but the data acquired in each one differs from the data in the original TDLAS setup. This entirely depends on the Fabry Perot interferometer. Because of its components' characteristics and its working principle, constraints in the magnitude of the light's intensity must be applied. For example, high intensity light beams can damage the mirror's surface when reflection occurs. Thus, for the sake of convenience and safety, the light beam with lowest intensity is the one that is going to interact with this interferometer i.e. 1 %. Therefore, the Fabry Perot interferometer will be connected to Channel 2. With respect to Channel 1, the signal traveling through it is the output intensity of the Mach Zehnder interferometer. Lastly, Channel 3 will remain unchanged, carrying the signal that defines the output intensity

after the absorption procedure.

With the current configuration, one experiment at ambient conditions, considering ambient 23 °C and 0.96 atm, is performed. For such experiment, again, one tunable laser diode (LD368) sweeping in intensity is used. The LD input characteristics are set to 24.48 °C, 75.22 mA and 1.91 V, being constant during the whole experiment. After 100 measurements, results are post-processed.

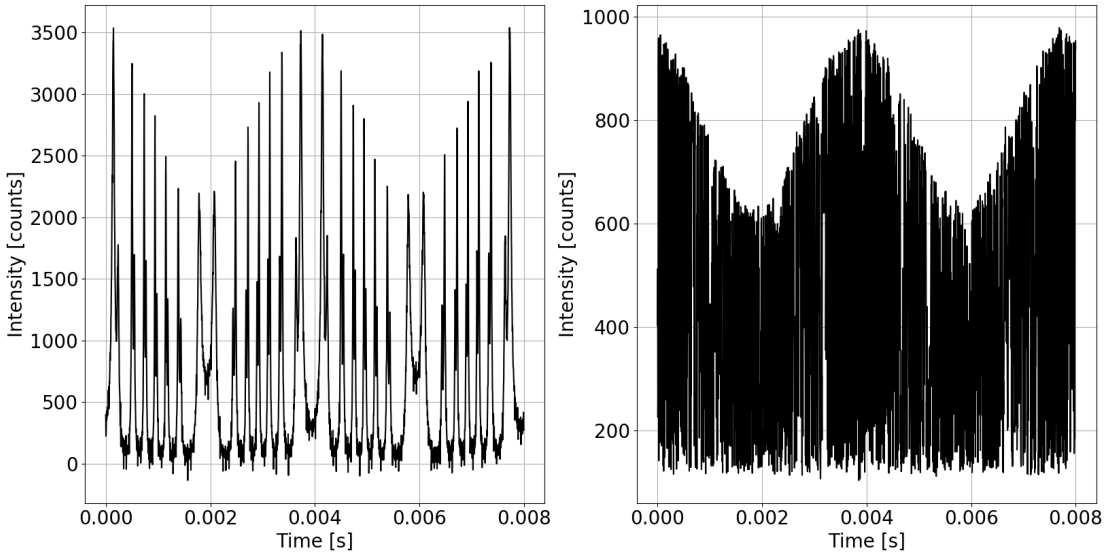


(a) Fabry Perot signal (b) Mach Zehnder signal

Fig. 3.10. Interferometers' output signal comparison

In this case, absorption is not relevant but the performance of the interferometers. Through it the intention is to compare the signal in each and identify the cleanest one to work with. Figure 3.10 displays both FP and MZ interferometers' signal in terms of intensity. As the Figure depicts, the Mach Zehnder contains less modulations than the Fabry Perot interferometer. Looking closer to the figure, double peaks can be also seen in the FP signal, coming from polarization effects. Furthemore, the the FP is more sensitive to changes and a small movement of the optical fibers can change abruptly the signal's shape in short periods of time. Therefore, it is demonstrate the preference of using the Mach Zehnder interferometer.

## 3.2. TDLAS Pressure Estimation

Once the calibration procedure with the MZ interferometer is completed, TDLAS setup is ready to be utilized. Putting theory into practice, this section contains all static pressure results estimated from spectroscopy. In the contest of increasing complexity, three types of scenarios are created. Firstly, experiments with one laser diode and air at ambient pressure and temperature are simulated. This is the simplest scenario at which static pressure will be estimated. Secondly, experiments with one laser diode but changing

pressure and at ambient temperature are made. Lastly, experiments with two laser diodes varying the pressure and at a constant temperature are reproduced.

### 3.2.1. Experiment 1: One LD at ambient pressure and temperature

Focusing first at the simplest level, both temperature and pressure inside the test chamber are going to be set to ambient conditions, 22.8 ° C and 0.95 atm, being fixed during the whole experiment (Fig 3.11 ).

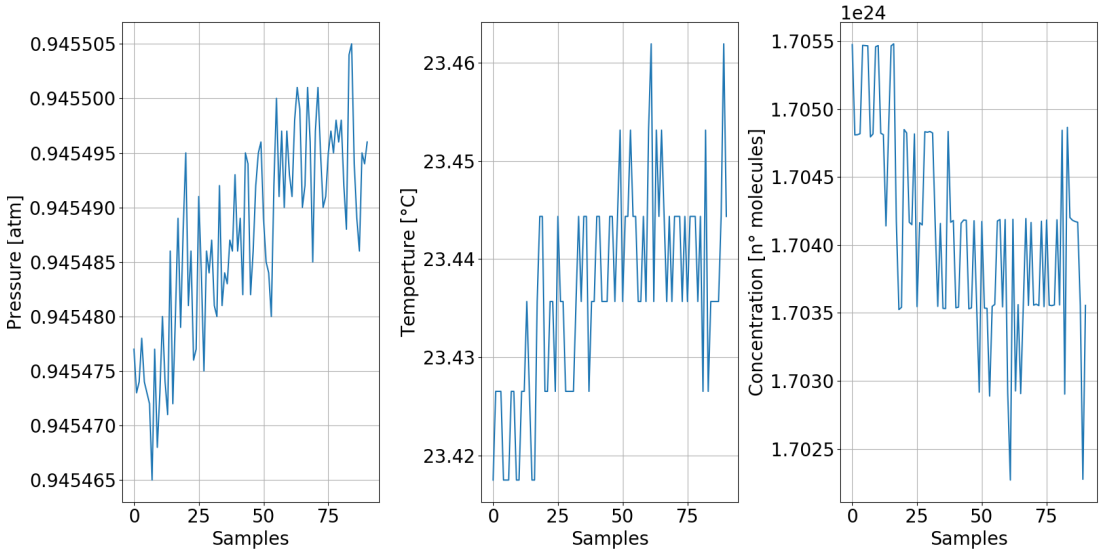


Fig. 3.11. Ambient conditions for Experiment 1

To achieve this objective, the pump is switched off and the valve opened. Also, just one Laser Diode LD368 is used. To select a strong oxygen absorption line, an oscilloscope is used. Varying the input settings of the LD, the absorption line is identified. Thus, the working setting of the laser diode related to it are: a temperature of 24.72 °C, a current of 75 mA and a wavenumber of 13143.48 $cm^{-1}$. This last value of frequency was obtained from the substitution of the LD temperature into the temperature-frequency relation described in Figure 3.8.

Moreover, a signal generator is utilized to create a signal with a saw tooth shape (instead of the common sine wave). The signal of both Channel 1 and Channel 3 will have this shape. In this way, by introducing a linear sweep of the intensity, uncertainties and noise appeared from the change of the slope in the sine wave will be eliminated. The saw tooth signal for this experiment will have alternated sweeps. This is done due to the operating settings of Experiment 3. Because of Experiment 3 will be performed with two laser diodes, there will be two pairs of input and output intensities. In order to not change the settings of the signal generator to include the second intensities of the additional laser diode, alternative sweeps are introduced for this experiment (explained in detail in Section 3.2.3). With all these input settings, a spectroscopy experiment takes place. 100 absorption measurements are simulated in an iterative process and in each one,

the three signals from the three Channels are processed. Figure 3.12a depicts both input and output intensities from the absorption procedure using LD368. Then, following the approach described in Section 2.4.2, with the Lambert-Beers' law from Equation 2.4, the absorption function is defined (3.12b).

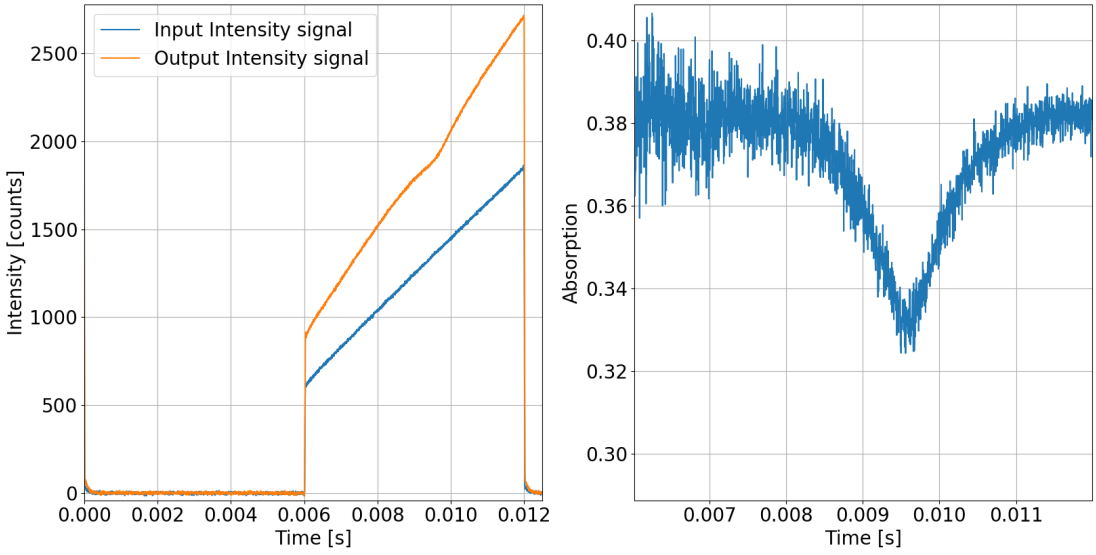


(a) Input and output intensities

(b) Absorption function

Fig. 3.12. Experiment 1: absorption function from spectroscopy (one sweep)

From it, $\gamma_{Doppler}$ is estimated via Equation 2.13. Substituting into the expression the laser diode frequency 13143.48 $cm^{-1}$, ambient temperature 23.42 °C, oxygen molecular mass 32 u and assuming a speed of light equal to $3x10^8$, the value of $\gamma_{Doppler}$ at each one of the 100 iterations are computed. Because the temperature here is fixed, the value of $\gamma_{Doppler}$ remains constant during the whole experiment, being 0.43 GHz.

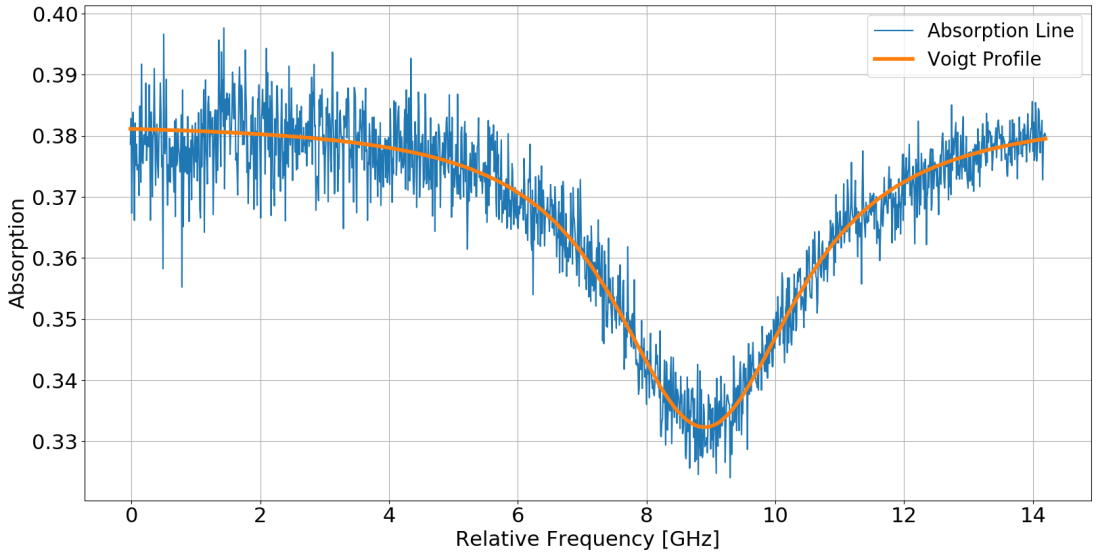


Fig. 3.13. Voigt profile at ambient pressure

Fitting the absorption function into Voigt profile with a fixed value of $\gamma_{Doppler}$ (so no Doppler contribution into the line broadening), an iterative process is carried out to obtain $\gamma_{Lorentz}$ at each iteration. Recapitulating from Section 2.4.2, the location of Voigt center, the inclination of the Voigt profile with respect to the horizontal plane and now, the width of the Gaussian width are kept fixed in every iteration, so the only variables in the fitting are the Lorentzian width and the Voigt area. As an example of this fitting, Figure 3.13 contains an absorption line at ambient pressure fitted with Voigt profile. In this case, the Voigt width profile is defined from the calibration procedure, being the frequency sweep.

Performing the fitting in each iteration, the value of $\gamma_{Lorentz}$ is found to be oscillating between 1.43 GHz and 1.45 GHz, being the average 1.44 GHz.

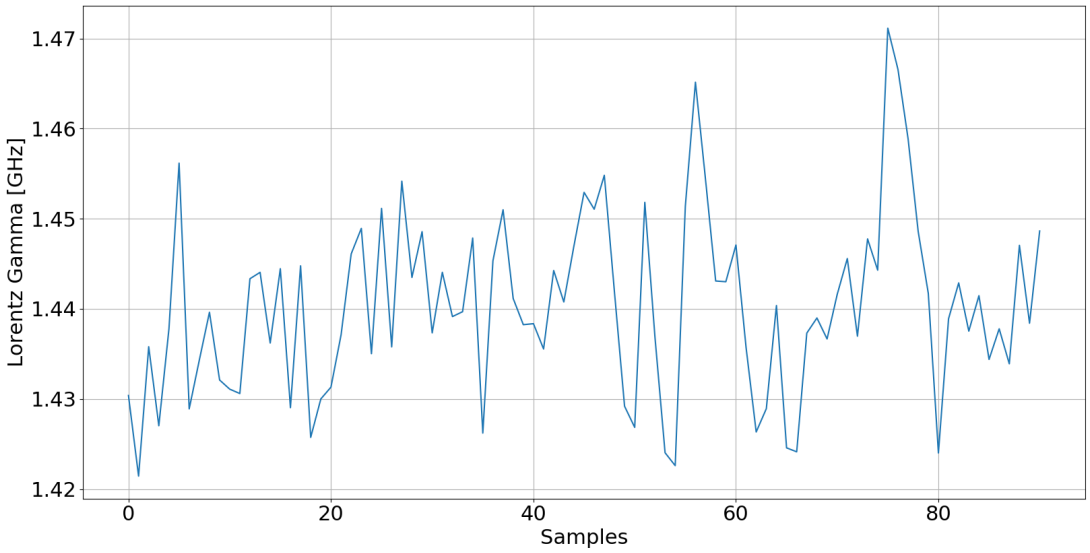


Fig. 3.14. Value of gamma lorentz during Experiment 1

Although this offset is practically negligible, it may come from different sources i.e. the way the experiment was performed. The time waited between each sample could have not been enough for the light to stabilize. The not-perfect isolation of the setup to external loads can also be a possible source of error. The noise induced by electronics could have played a role in the measurement deviations. Last but not least, the numerical procedure also could have generated these oscillations. To support these arguments, here are plotted the Voigt's amplitude and full width half maximum (FWHM) parameters.

Recalling from theory, the Voigt profile is defined as the convolution of Gaussian and Lorentzian distribution. More specifically, the width of Voigt profile comes from the resultant combination of Gaussian and Lorentzian width. Therefore, if the width of the Gaussian distribution $\gamma_{Doppler}$ is fixed, it can be assumed the Voigt's width will totally depend only the width of Lorentzian function $\gamma_{Lorentz}$. Because in this experiment pressure is also fixed, the effect due to collisional broadening is negligible and so it can be expected that the Lorentzian distribution has also a fixed width throughout the whole experiment, being the Voigt profile's shape unchanged. Nonetheless, the Figures below show fluctuations in the Voigt's amplitude, FWHM and $\gamma_{Lorentz}$ fluctuations.

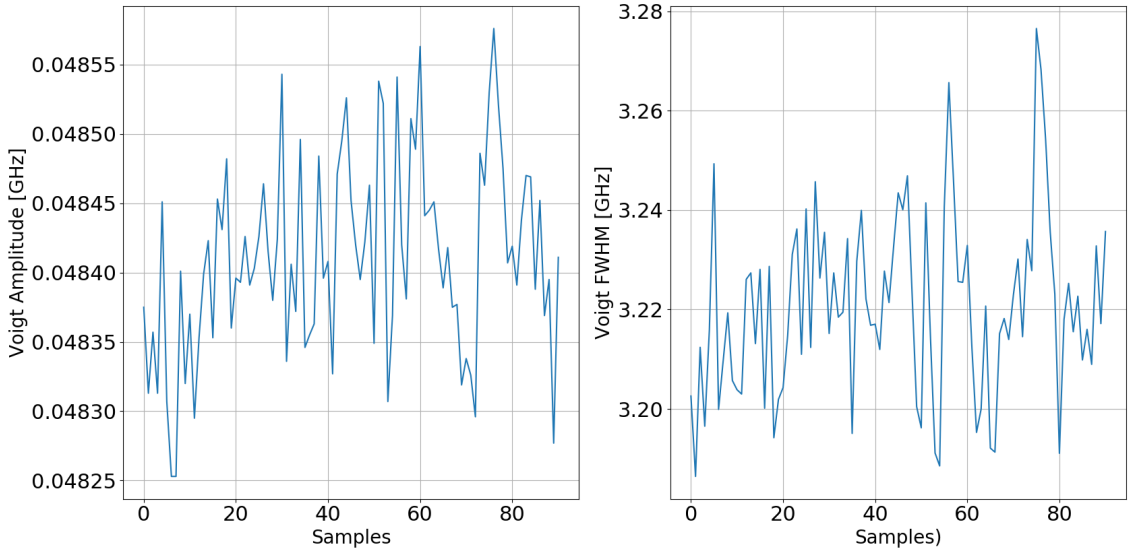


Fig. 3.15. Values of voigt amplitude and FWHM in Experiment 1

From $\gamma_{Lorentz}$, the static pressure value is approximated with Equation 2.16 . The wavenumber at which the laser diode is operating defines the broadening coefficients of the oxygen line. In this case, for a wavenumber of 13143.48 $cm^{-1}$, the broadening coefficients obtained from HITRAN database are $\gamma^0_{O_2 self}$ 0.047 and $\gamma^0_{Lforeign}$ 0.048, with a $n$ value of 0.73. Substituting in Eq. 2.16 all the above values and assuming a concentration of oxygen in air of 20.9 %, pressure is estimated. Figure 3.16 depicts the value of the pressure at each iteration. As shown in the Figure, the value of the pressure oscillates between 0.995 atm and 1.02 atm, in a range of 0.025 atm and being the average 1.006 atm. As mentioned in Section 2.4.2, $\gamma_{Lorentz}$ is directly proportional to the static pressure, so the oscillations induced in the former will also affect the latter.

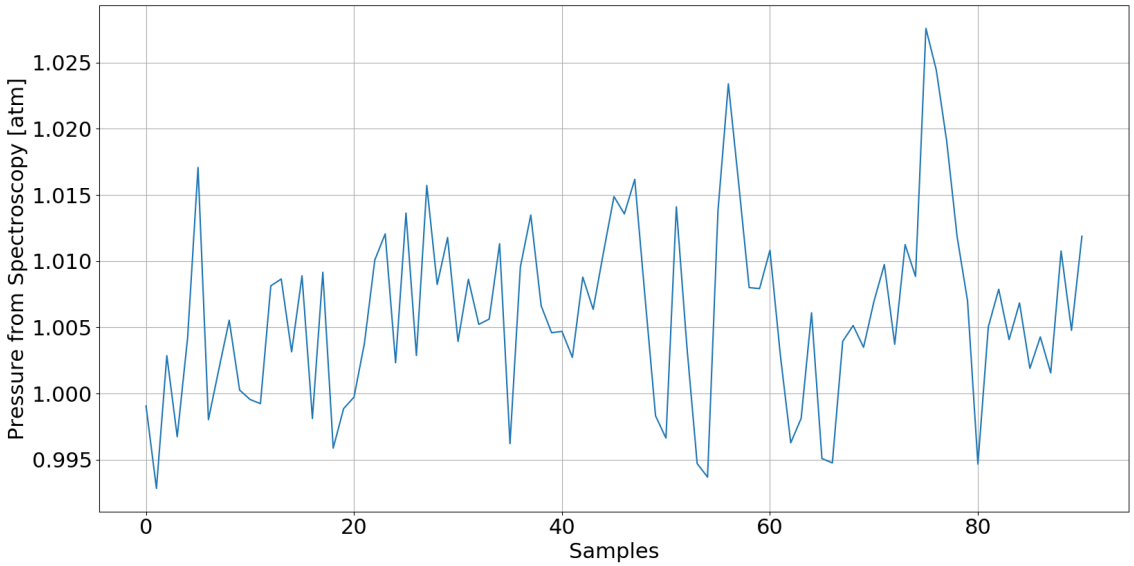


Fig. 3.16. Spectroscopy Pressure at each sample in Experiment 1

To validate the value of static pressure, the sensor installed in the TDLAS setup is

used. This sensor has measured the pressure inside the test chamber in each one of the iterations, being practically fixed at 0.945 bar (0.933 atm). Thus, the average relation between them is 1.006 atm from the spectroscopy procedure against 0.933 atm from the sensor. Between the two outputs there is an offset of approximately 0.07 atm.

Apart of the possible sources of error previously mentioned, this offset can also come from the sensor itself. This last source is unlikely due to the sensor implemented in the setup is a very precise pressure sensor which also gives an approximated value of the temperature inside the test chamber. Nonetheless, values read from the sensor could have inaccuracies. The not perfect calibration with the Mach Zehnder interferometer is another possible source of error that could have given inaccurate pressure values from the spectroscopy experiment. Nevertheless, with this experiment it has been demonstrated the viability of obtaining ambient static pressure from the spectroscopy procedure.

### 3.2.2. Experiment 2: One LD at variable pressure and ambient temperature

Increasing the complexity, a second spectroscopy experiment at a non-fixed pressure value is performed in order to obtain the static pressure. The same working characteristics for the laser diode are set ($T$ equal to 24.72 ° C, current at 75 mA and a wavenumber of 13143.48 $cm^{-1}$). Nonetheless, in this case, the pressure inside the test chamber changes.

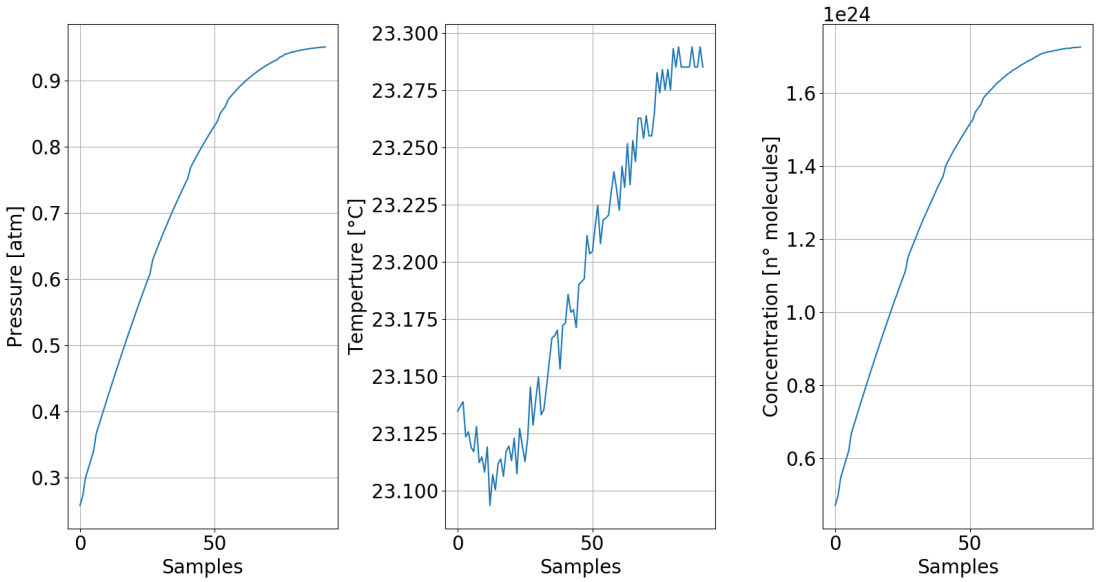


Fig. 3.17. Ambient conditions for Experiment 2

To do so, the valve that connects the test chamber with the pump is opened. Switching on the pump, air is extracted until a pressure of 0.2 atm is reached. This value remains blocked for the first measurement. Then, the valve is automatically unlocked for 1 second, increasing the concentration of air inside and so the pressure. The procedure is repeated 100 times, taking 100 absorption measurements until ambient pressure is reached.

Figure 3.17 illustrates the evolution of pressure, temperature and concentration of air

during the time the experiment takes place. As it can be seen in the graphs, the value of pressure gradually increases in a smoothly curve until reaching ambient conditions. As for temperature, because it has been fixed as ambient, it is kept with a value of approximately 23.2 ° C. A small oscillation of +/- 0.1 ° C is introduced in the final value, which could be as a side effect of pressure growth. Lastly, as it can be expected, pressure increases as the number of molecules increases, being both curves proportional.

From each measurement, the light intensity in the three Channels is processed. Again, the ratio between Channel 1 and 3 gives the absorption function from Lambert-beer's equation. Differing from Experiment 1, the shape of the absorption line at each one of the measurements is going to vary.

Recalling the line broadening mechanisms, the relation of pressure in the shape of the absorption line is mainly described by collisions (collision broadening). From Eq. 2.16 and Experiment 1, it is demonstrated pressure is directly proportional to $\gamma_{Lorentz}$. Also, when increasing the pressure inside the test chamber, there is a higher probability of molecules to collide with each other and so higher collisional broadening effects in the absorption line. In other words, higher pressures leads to broader absorption lines. For just analyzing this effect, temperature in the experiment is again fixed and so $\gamma_{Doppler}$, being approximately 0.64 GHz. Fitting each one of the absorption line with the Voigt profile, the value of $\gamma_{Lorentz}$ at each measurement is estimated.

For the sake of understanding this effect of pressure in the Lorentzian width $\gamma_{Lorentz}$, Figures 3.18 and 3.19 depict two examples of absorption lines at two different pressure measurements:

- Voigt profile at 0.25 atm:

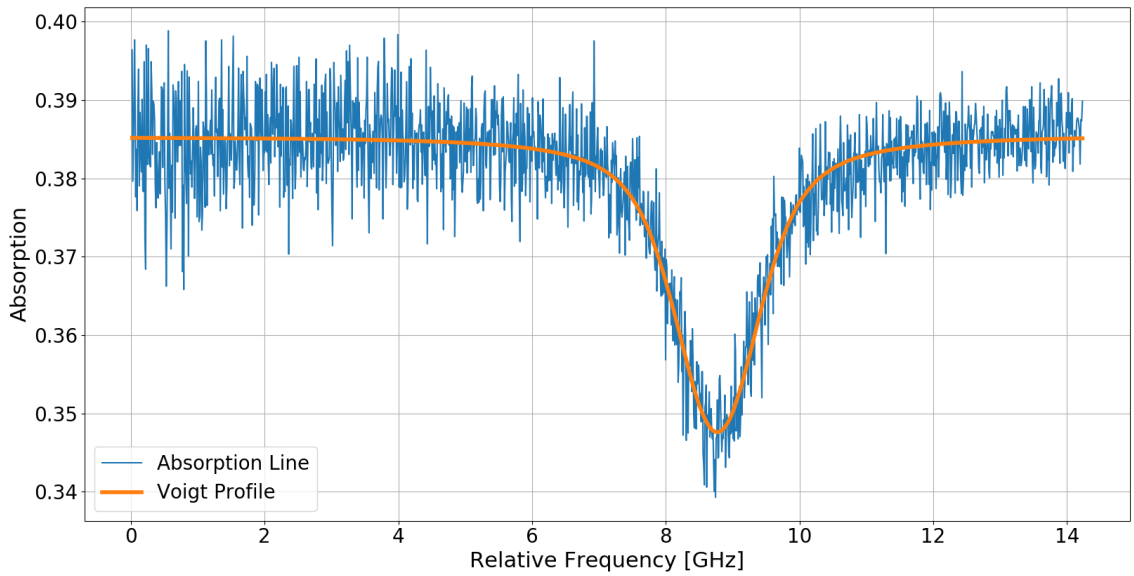


Fig. 3.18. Absorption line at pressure equal to 0.25 atm

- Voigt profile at 0.95 atm:

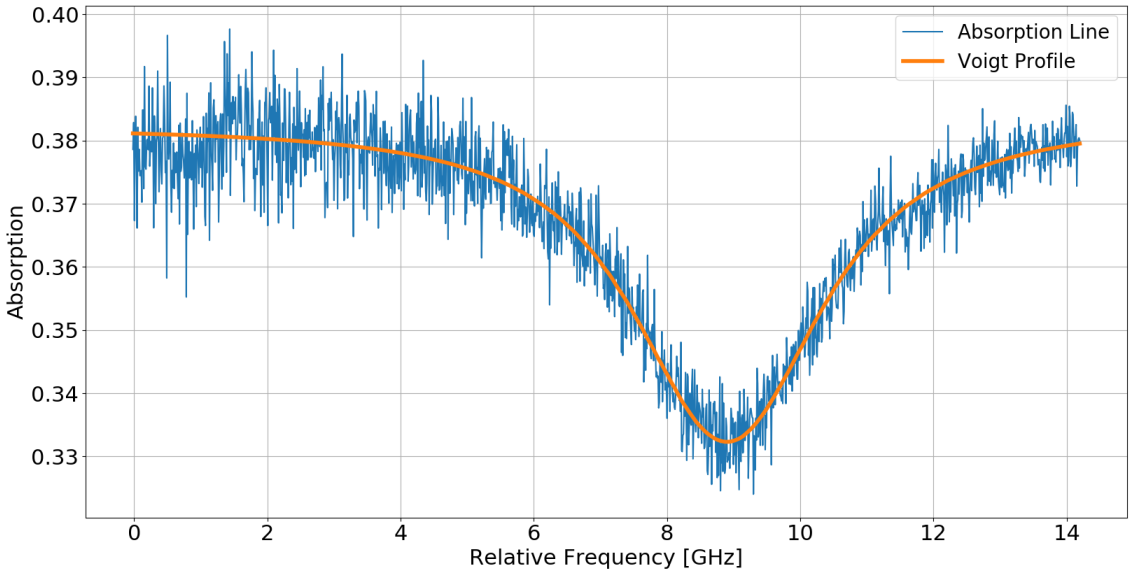


Fig. 3.19. Absorption line at pressure equal to 0.95 atm

Then, making use of Eq. 2.16, pressure for spectroscopy is determined. Figure 3.20 illustrates both magnitudes as a function of the pressure read from the sensor in each one of the 100 measurements.

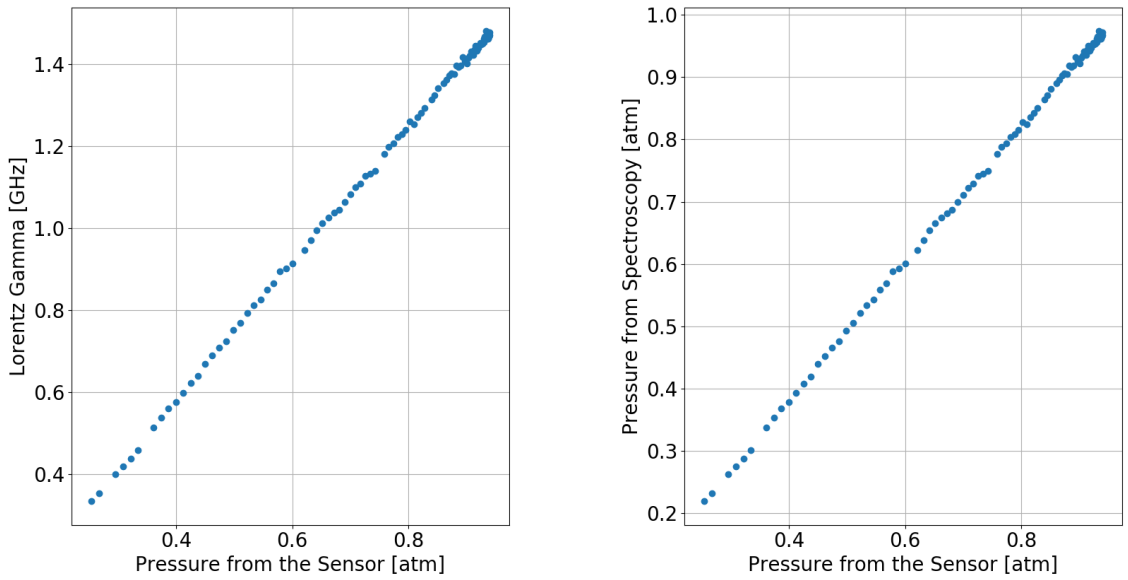


(a) Lorentz gamma vs. pressure from sensor (b) Spectroscopy pressure vs. pressure from sensor

Fig. 3.20. Spectroscopy results from Experiment 2

As shown in Fig. 3.20a, increasing pressure inside the chamber, $\gamma_{Lorentz}$ also increases following a linear distribution. Because of all parameters that define the Voigt profile are kept as constant as the exception of $\gamma_{Lorentz}$, pressure from spectroscopy will vary directly proportionally to $\gamma_{Lorentz}$ (Fig. 3.20b). When comparing both values of pressure, however, it can be seen an offset between both magnitudes. At low pressures, the values

of pressure from spectroscopy are smaller compared with the ones from the sensor. For instance, when the sensor reads 0.29 atm, spectroscopy pressure is 0.26 atm. The best fit is obtained between 0.5 - 0.6 atm, being both values practically equal. From that point onwards, pressure from spectroscopy increases linearly faster than pressure from the sensor, being at the very end 0.97 atm versus 0.93 atm. Basing on these results, one can conclude that, although a good matching between both magnitudes is possible, there is an external factor affecting the spectroscopy output.

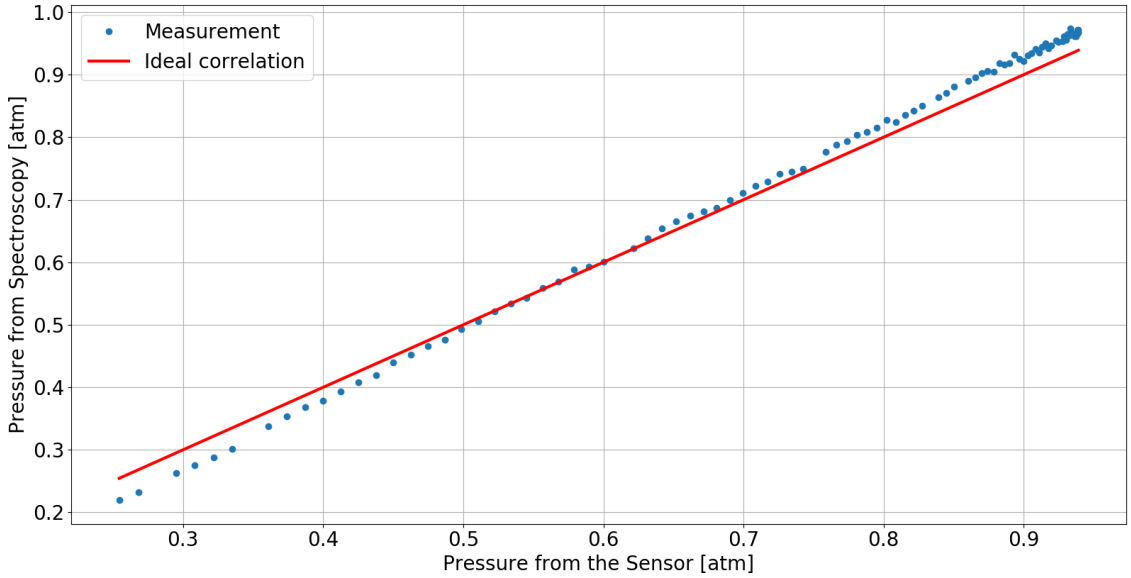


Fig. 3.21. Pressures comparison from Experiment 2

Recalling from Section 2.2, the test chamber is actually divided in three parts. The one located at the middle is where the absorption procedure takes place meanwhile the two located at the extremes are just passages for stabilizing the light beam. For this last purpose, both parts need to be at vacuum conditions, so the output light beam is not altered. At the moment the experiment was performed, one could have assumed both parts were at vacuum conditions. Nevertheless, it could have not been the case. If both sections were still storing air when the experiment took place, an extra absorption term (unknown value) could have been added into the equation. As a consequence of this effect, broader absorption lines could have been created contributing to the achievement of higher pressure values (Figure 3.22). This explanation not only justifies rapidly increase in the pressure slope but allows the problem to be nicely solved. With the aid of a more powerful pump, air is extracted from both sections, reaching a pressure value of 0.002 atm. Then, in order to be more productive and efficient, experiments with both laser are performed.

### 3.2.3. Experiment 3: Two LD at variable pressure and ambient temperature

With the TDLAS fully analyzed and ready for accurate pressure measurements, the third type of experiments is carried out. As in Experiment 2, ambient temperature is kept,

being 23.44 ° C and pressure is firstly reduced to 0.2 with a mechanical pump and then increased via valve until a value of 0.96 atm is reached in an iterative process of one hundred iterations.

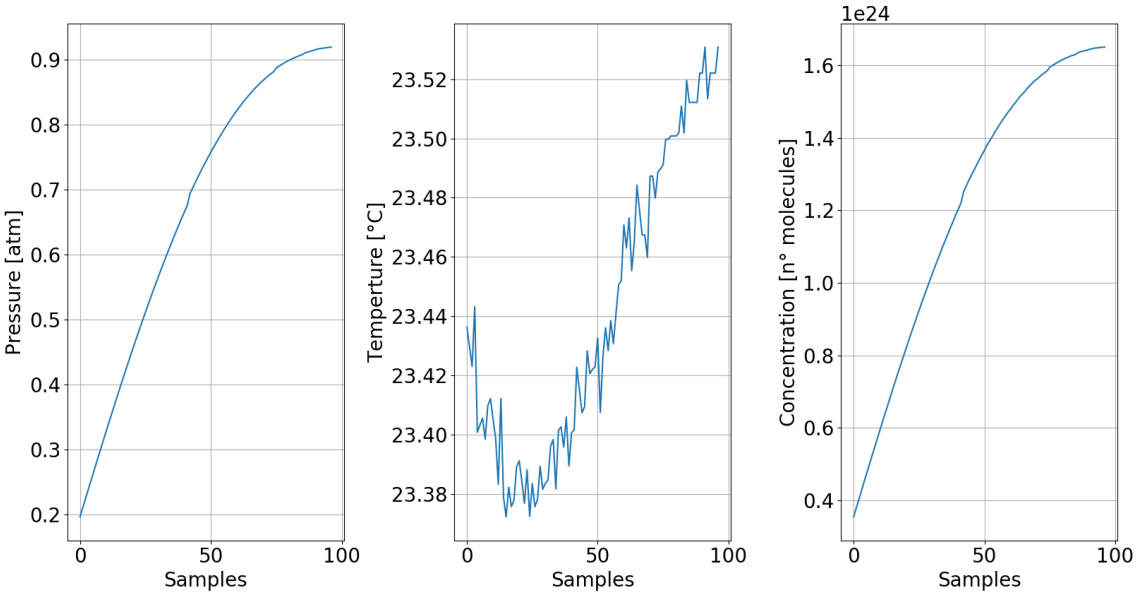


Fig. 3.22. Ambient Conditions for Experiment 3

The main difference in Experiment 3 is the number of laser diodes utilized. Here, both LD are switched on (LD366 and LD368). The principal reason for working with both laser diodes is to obtain simultaneously the pressure results as well as their variation with respect to their initial settings. Basically, it is desired to acquire in just one measurement pressure values from each one of the two laser diodes at two different initial conditions. So, using an oscilloscope, two absorption lines at different LD input settings are selected.

As in the other experiments, the selection of both of the lines relies on the value of its cross-sectional absorption parameter, which literally depends on the temperature and pressure. Stronger lines (high cross section absorption) are preferred so a better visualization of the absorption effect can be acquired. Due to temperature is assumed to be fixed inside the test chamber and pressure is the only parameter that will vary during the experiment, two absorption lines with the same cross-section absorption value are selected, so results can be comparable. For the laser diode LD366, a working temperature of 15.6 ° C is specifically selected. With the oscilloscope, an absorption line at that temperature is picked, with a wavenumber of 13150.19 $cm^{-1}$ (wavelength equal to 760.445 nm). Again, substituting these values into the temperature-wavelength-current relation from Figure 3.7a, a working current of 53 mA is found. Repeating same procedure for LD368, its working characteristics are: 29.25 ° C, 13138.20 $cm^{-1}$ (761.139 nm) and 67 mA, respectively. In this way, each laser diode works at a different conditions and so the value of pressure from spectroscopy can be characterized regarding them. Table below contains the input settings of each LD.

| Laser diode | Temperature (°C) | Wavenumber ($cm^{-1}$) | Current (mA) |
|---|---|---|---|
| LD366 | 15.60 | 13150 | 53 |
| LD368 | 39.25 | 13138 | 67 |

Table 3.2: LD366 and LD368 settings

To work with the presented configuration, a modification in the settings of the signal generator must be performed. The usage of both laser diodes requires to introduce both signals into a single channel, for its further post-processing. Channel 1 and Channel 3 will now contain the input and output intensities of the light beams (respectively) from the absorption procedure for both laser diodes. Basically, the input intensities of the light beam from both laser diodes will be emerged into one signal (Channel 1), being alternated in each intensity sweep. To do so, laser diodes will alternatively be switched on and off. Similarly, the output intensities from both laser diodes will be emerged into the signal of Channel 3 following the same pattern. Figure 3.23a illustrates an example at static pressure equal to 0.2 atm of the signals generated for both input and output light intensities from Channel 1 and 3.

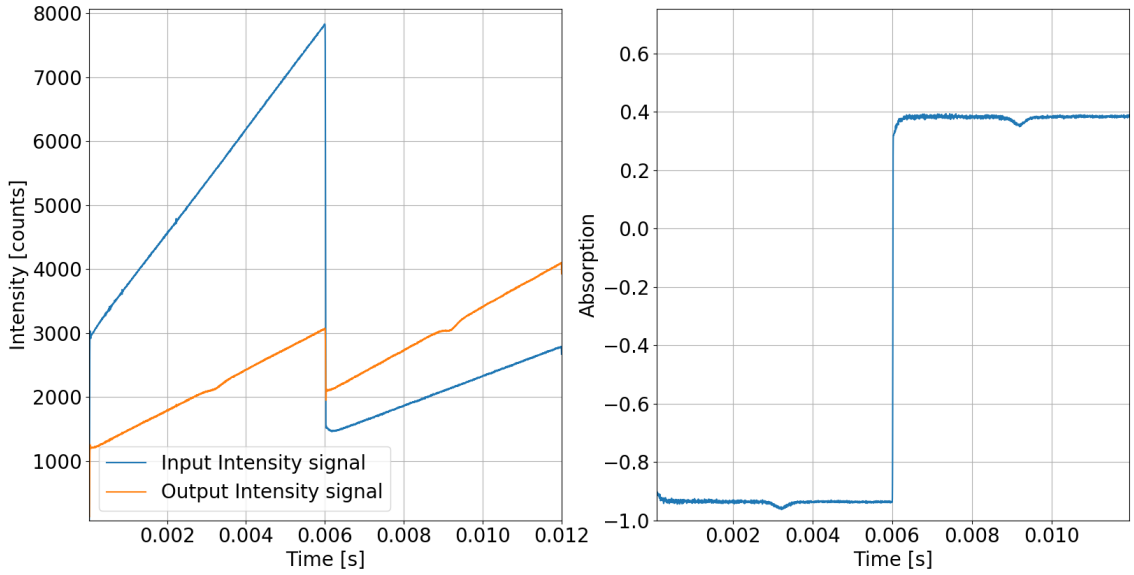


(a) Input and Output intensities

(b) Absorption function

Fig. 3.23. Experiment 3: absorption function (one sweep each LD)

The first simultaneous pair of sweeps refers to LD366 (from 0 to 0.006 s) and the second to LD368 (from 0.006 to 0.012 s), and so on and so forth. From them, the absorption function related to each laser diode settings is estimated, as shown in Figure 3.23b. Here is important to study the values of both absorption functions. As remarked in Experiment 1 and 2, the absorption parameter goes from 0 to 1. Looking in detail into Figure 3.23b, it can be observed that for the second laser diode, negative values are introduced in the graph. Nonetheless, this is not the real absorption but with an offset included. Hence,

each absorption function normalized is contained between the range 0 and 1.

Continuing with the spectroscopy experiment, from ambient temperature 23.44 °C read with the sensor, value of $\gamma_{Doppler}$ is approximated to 0.43 GHz, being the same as in Experiment 1 and Experiment 2. Regarding the absorption line fitting into the Voigt profile, in this experiments there are two absorption lines obtained in the process. Hence, to fit each absorption line, the absorption function has to be alternatively split to treat each one separately.

Beginning with LD366, the absorption line is fitted into the Voigt profile and hence the Lorentzial width $\gamma_{Lorentz}$ is approximated in each measurement, as shown in Fig. 3.24a. Then, recalling Equation 2.16 in Section 2.4.2, from the Lorentzian width $\gamma_{Lorentz}$, the static pressure is estimated (Fig. 3.24b). Analyzing the results from above, the proportionality between both magnitudes is clearly proved. Moreover, in relation with the magnitude of pressure values, they are characterized to follow a linear regression from 0.15 to 0.85 atm.

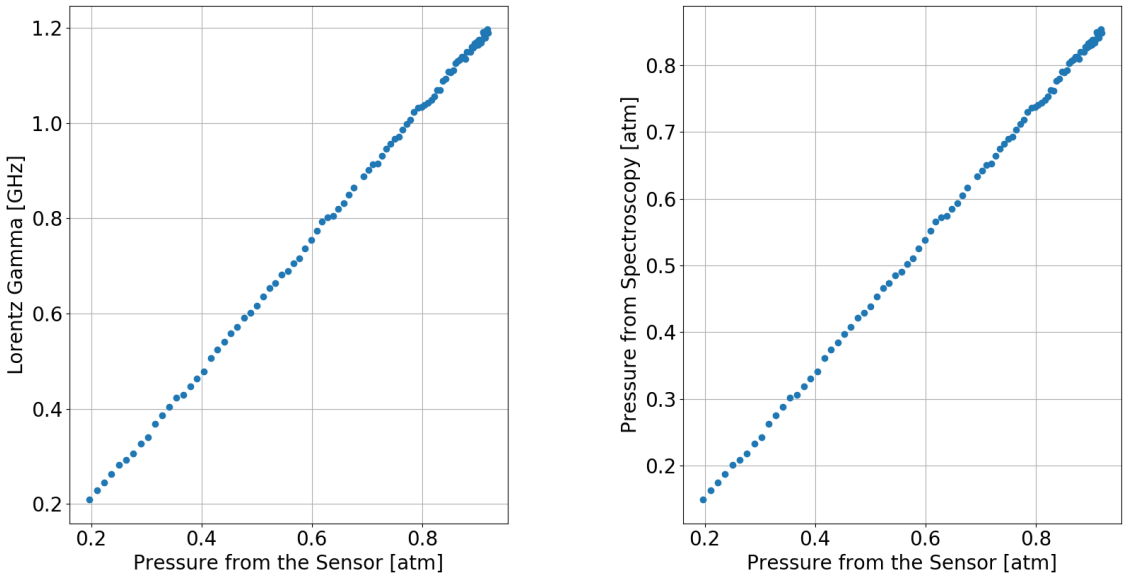


(a) Lorentz Gamma vs. Pressure from Sensor (b) Spectroscopy Pressure vs. Pressure from sensor

Fig. 3.24. Spectroscopy results from Experiment 3, LD366

To validate the value of $\gamma_{Lorentz}$ and so of pressure, the characteristics that define the Voigt profile need to be evaluated.

As stated in the very beginning of this subsection, temperature is kept constant during the whole experiment, being the average value 24.4 ° C. As in Experiment 2, the change in pressure leads to an increase of +/- 1 ° C inside the test chamber. In addition, it is the main driver for the Doppler broadening mechanism, so the value of $\gamma_{Doppler}$ is solely and directly dependent of the value of temperature, as demonstrated in the second graph (Gaussian gamma vs. Pressure from Sensor). Therefore, the value of both magnitudes barely changes and stays fixed at 23.4 ° C and 0.43, respectively.

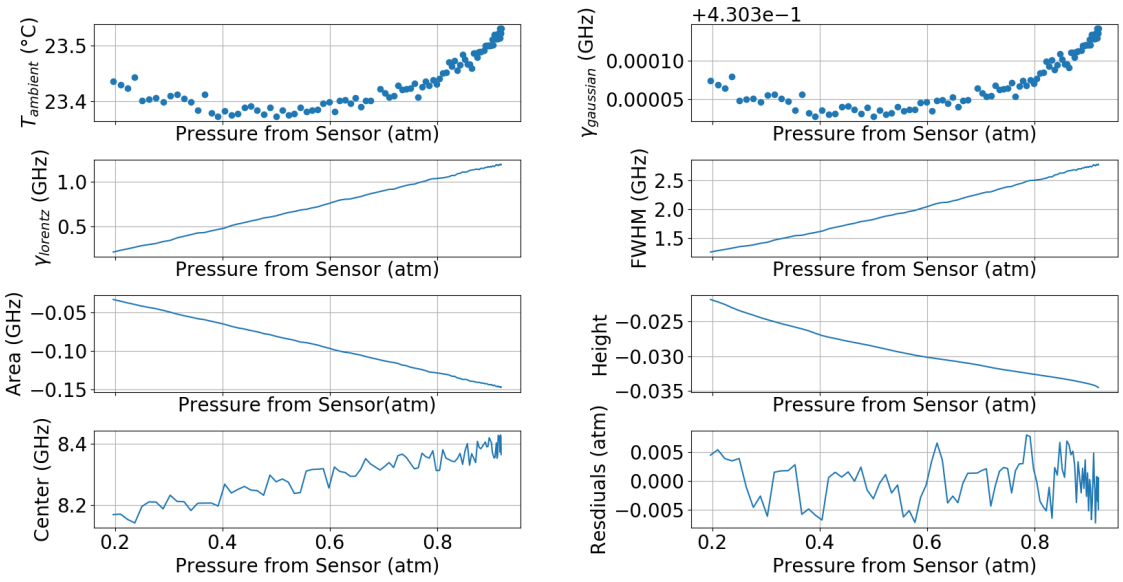


Fig. 3.25. Output characteristics of the Voigt profile using LD366

Thinking out, as proved in the second Experiment, width of Voigt profile is exclusively conditioned by the variation of pressure and, therefore, by variation of $\gamma_{Lorentz}$, which is defined as the HWHM of the Voigt profile. Increasing the gas concentration leads to an increase of pressure inside the test chamber and so wider absorption lines. Hence, Figure 3.25 third plot demonstrates this statement with a linear sweep in the value of $\gamma_{Lorentz}$. Same behavior can be characterized in plot number four, where FWHM is represented against pressure from sensor. Moreover, the area enclosed inside the Voigt profile is defined as the Voigt amplitude and is also dependent on $\gamma_{Lorentz}$. Bigger areas are obtained when enlarging the width. Thus, Voigt's amplitude linearly increases, getting broader with time as demonstrated in plot number five. Just to finish, the slightly and constant movement of the center location to the right (seventh plot) is a quantum mechanical effect. With respect to the values of residuals, study will be cover later on.

The previous validation of the Voigt profile's characteristics demonstrates an accurate fitting of the absorption lines. However, as shown in Figure 3.24b, pressure results from spectroscopy do not coincide with the ones read by the sensor. Figure 3.26 depicts a clearer picture of the offset between magnitudes.

For an easier understanding, a linear regression of the measured values is plotted. Comparing both functions, it is shown a constant offset between the pressure from sensor that should have been obtained and the measured one from the spectroscopy experiment. The value of this offset is approximately 0.04 atm. As in Experiment 2, main cause for this offset could have been the non-perfect calibration with Mach Zehnder interferometer, leading to a constant error of imprecision between both magnitudes. Looking closer into the graph, values from measured pressure are oscillating though its linear regression. These oscillations are the ones induced by the value of $\gamma_{Lorentz}$, FWHM and Voigt's amplitude, as illustrated in Figure 3.26.

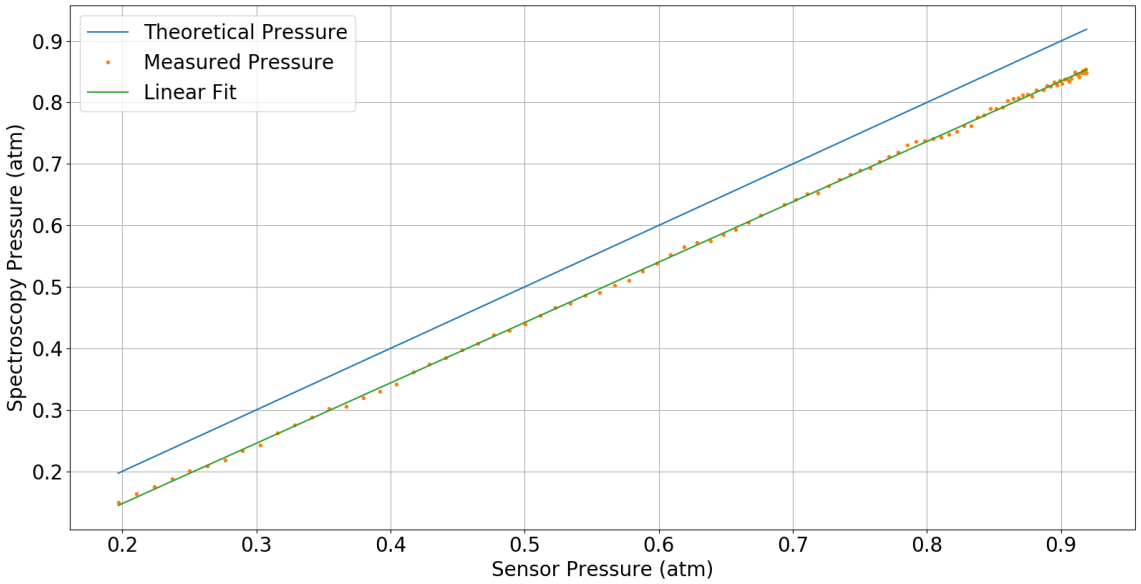


Fig. 3.26. Theoretical pressure vs. measured pressure using LD366

Contrasting them, small offsets in the order of magnitude of less than 0.0075 atm are found (Figure 3.27, middle plot). As explained beforehand, these induced errors in pressure measurements could have been the consequence of a non-exact calibration of the TDLAS setup, non-precise experiments' development or/and non entirely suitable numerical approach. Nonetheless, the average percentage of error here is less than 1.05 %. For lower pressures, this error is higher due to the still existence of extra absorption inside the test chamber. Non-perfect vacuum conditions inside two of the three cells that compose the test cell and background absorption can be two possibilities of cause for this effect. On contrary, pressures higher than 0.26 atm, error is reduced to less than 0.48 %.

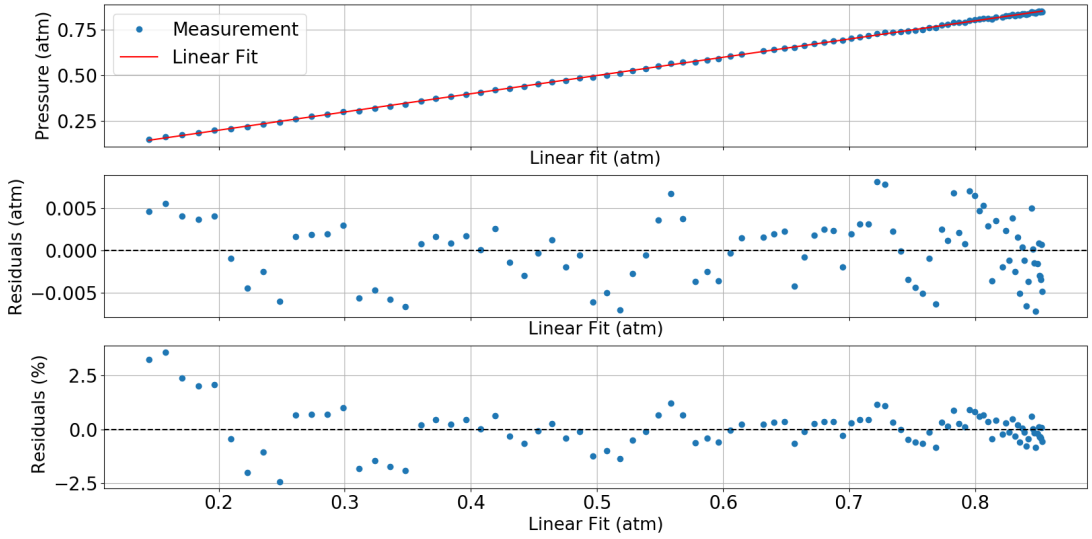


Fig. 3.27. Upper plot: measured pressure vs. linear fit (LD366). Middle plot: Residuals of measured pressure vs. linear fit(LD366). Lower plot: residuals (in percentage) of measured pressure vs. linear fit (LD366)

In order to reduce the oscillations in the measured values and obtain more accurate results, a weight function is included in the numerical method. The idea behind it is to improve the fitting procedure by eliminating possible appearance of imprecisions during the iterative process. To do so, values located at the peak and at the extremes of Voigt profile will have "more weight" in the fitting than the remaining values. Incorporating this correction into the numerical approach, $\gamma_{Lorentz}$ is estimated as well the static pressure.

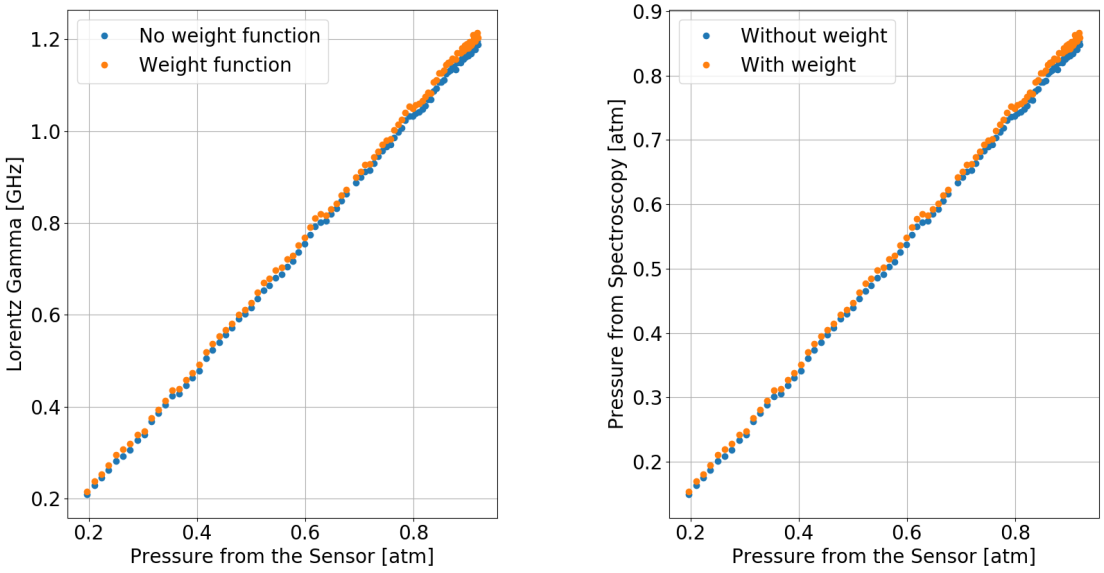


(a) Lorentz gamma vs. pressure from sensor (b) Spectroscopy pressure vs. pressure from sensor

Fig. 3.28. Spectroscopy results with and without weight function (LD366)

Figure 3.28 depicts the comparison between the spectroscopy results with and without using the weight function. Although it could have been expected a reduction in magnitude of the oscillations, this is very far from the truth. When implementing weight function, the magnitude of the offsets is not reduce but sometimes increased. Therefore, the oscillations in Lorentz and pressure values are not a consequence of the numerical fitting. A suitable explanation of this outgrowth relies on background effects. Fitting procedure is not the cause that generates them but the absorption function itself. As explained above, irregular absorption from the background can be the cause of these oscillations. Thus, to study this effect, a more detailed study about the absorption process inside the chamber must be carried out. This last is out of the scope of this Master Thesis.

Just to have a clearer idea of how pressure outputs are affected by the weight function, linear regression analysis of both results from Figure 3.28b is conducted. In the plot below, the offset of each measurement from the linearized value, with and without the utilization of weight function, is represented. As mentioned above, when including the weight function into the numerical approach, the damping behavior of the measurements does not decrease. Instead, some offsets are slightly increased in magnitude. Aside of this, the value of residuals is practically less than 1 %, being the most accurate values from spectroscopy experiments obtained. Hence, to conclude with, for analysis purposes,

the weight function is not included in the numerical approach.

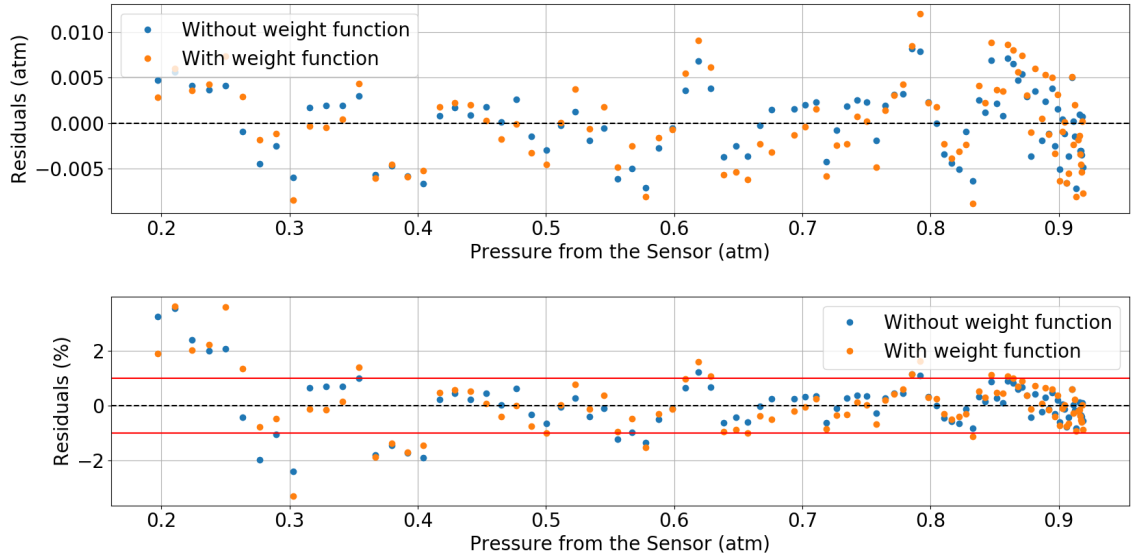


Fig. 3.29. Upper plot: residuals between measured pressure vs. linear fit with and without weight function (LD366). Lower plot:residuals (in percentage) between measured pressure vs. linear fit with and without weight function (LD366).

Lastly, altitude and flight level aircraft is flying at are estimated. Recapitulating from Chapter 2, both pressure and altitude are correlated as established in Equation 2.17. Thus, substituting in the former values of measured pressure from the spectroscopy experiment, the altitude (in meters) is estimated. Results are presented in Figure 3.30.

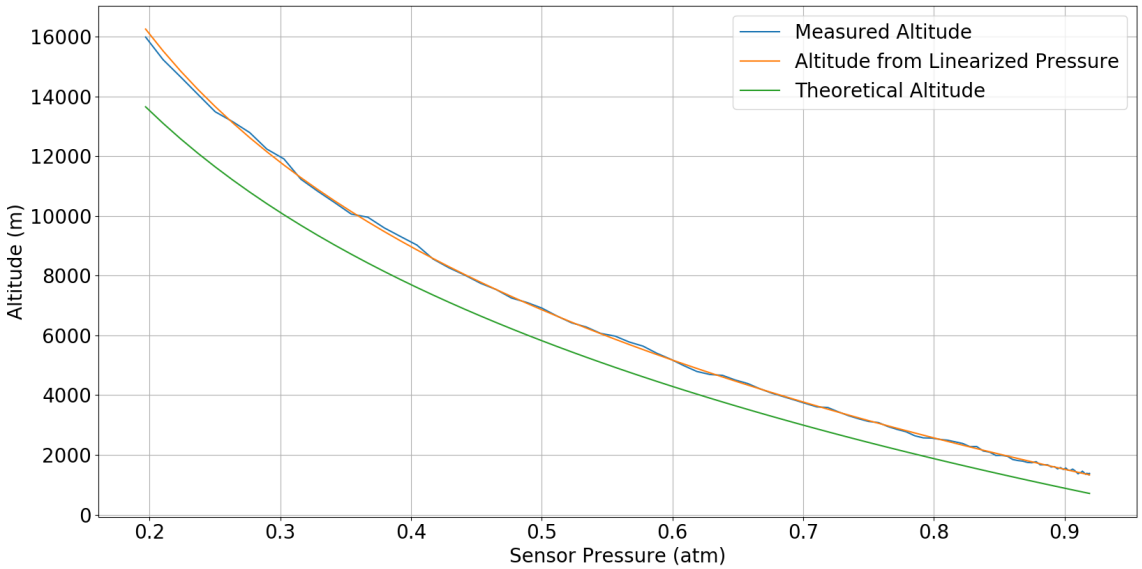


Fig. 3.30. Altitude calculation from spectroscopy pressure (LD366)

Comparing the measured pressure against linearized one, it can be seen an altitude error of approximately one / two hundreds meters. Due to the higher oscillations presented at low pressures, the altitude offset here is higher, reaching a maximum value of 292.6 m.

For pressures greater than 0.4 atm, this offset value remains below 100 m, as shown in Fig. 3.31. Indeed, this proves the high accuracy in the numerical method.

However, when comparing the measured pressure with respect to the one from sensor, difference between values is much higher. It is governed by the summation of a constant exponential offset plus oscillations. Because of the value of oscillations is much lower than the offset, the difference can be assumed to be just the offset itself. In this case, for pressures lower than 0.4 atm, the altitude error reaches a maximum of 2500 m meanwhile for higher pressures this offset is reduced up to 750 m, where it remains constant. Detailed information about these differences is given in Figure 3.31.

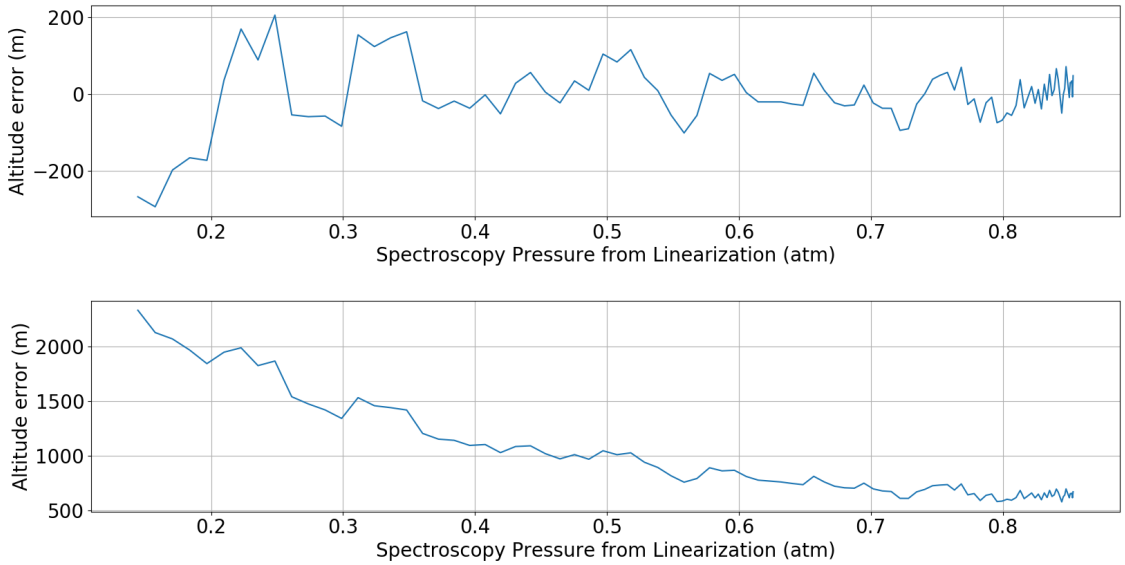


Fig. 3.31. Upper plot: Altitude errors measured and linearized pressures (LD366), Lower plot: Altitude errors mesured and theoretical pressures (LD366)

To sum up, it has been estimated the viability of estimating both static pressure and altitude using LD366 in the spectroscopy experiments.

To continue with the analysis, LD368 is utilized. Here, a working temperature of 29.25 ° C, at a frequency of 13150.19 $cm^{-1}$ and a current equal to 67 mA are selected. Because ambient temperature is keep as constant, the value of $\gamma_{Doppler}$ is equal to 0.43 (as for the experiment with laser diode LD366). Fitting the absorption line into the Voigt profile, the value of $\gamma_{Lorentz}$ is estimated for each one of the measurements during the experiment. Then, applying Equation 2.16, static pressure is automatically defined, as illustrated in Figure 3.32.

To validate results, characteristics of the Voigt profile are again studied (Figure 3.33). In this case, both values of $\gamma_{Lorentz}$ and pressure are slightly larger. As for the latest, it changes from 0.16 to 0.89 atm. Nevertheless, as illustrated in Figure 3.32, oscillations here are more prominent. In addition, from Figure 3.33, variations in the values of temperature and $\gamma_{Doppler}$ are practically negligible. On the other hand, $\gamma_{Lorentz}$ is defined with larger offsets in its measurements, being the oscillations of the value stronger. Same effect

can be seen in both FWHM and amplitude regressions. As the outcome, pressure results will have offsets of higher magnitude, being oscillating between +/- 0.01 atm.

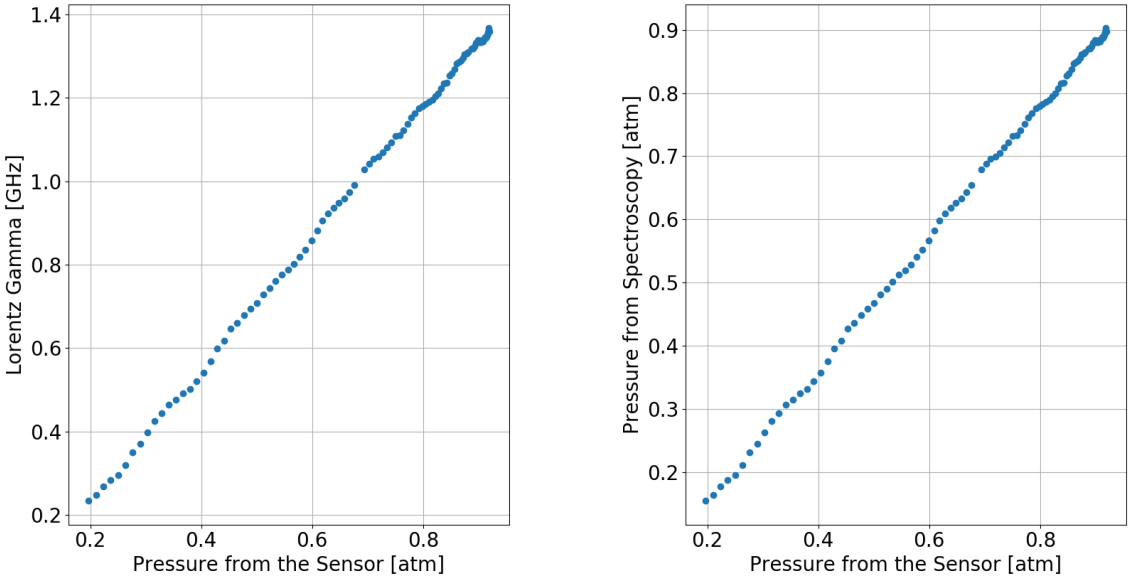


(a) Lorentz gamma vs. pressure from sensor (b) Spectroscopy pressure vs. pressure from sensor

Fig. 3.32. Spectroscopy results from Experiment 3, LD368

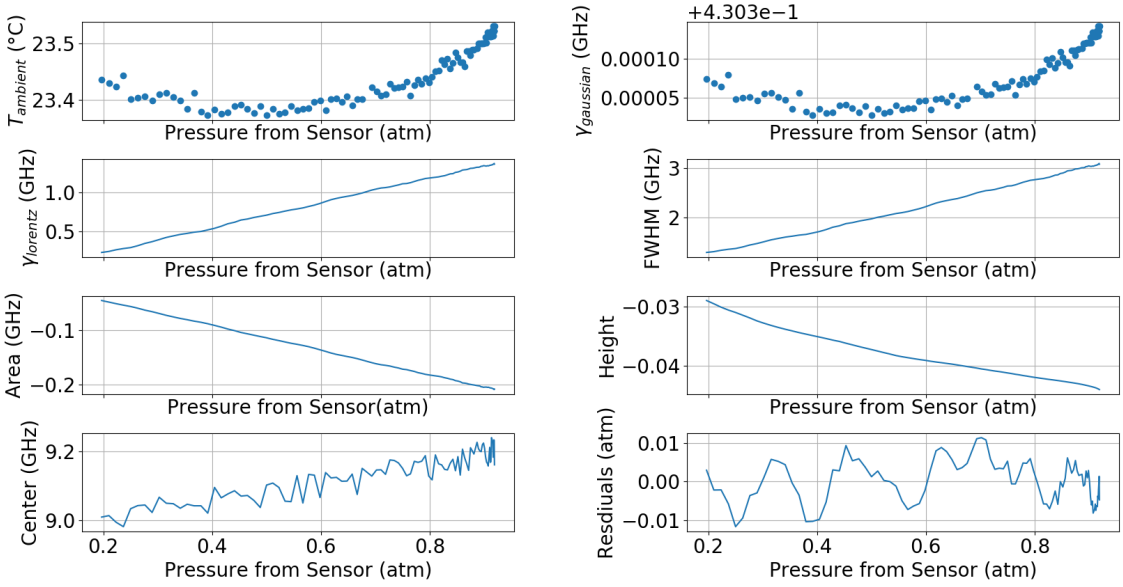


Fig. 3.33. Output characteristics of the Voigt profile using LD368

To have a better picture of the pressure residuals, a linear regression of the measured values is again approximated and plotted. The residuals values here vary between +/- 0.01 atm. Again, at lower pressures, these offsets are higher, reaching almost the 5 % of error. Then between the values of pressure of 0.3 atm to 0.45 atm, the offset is approximately between 2 % and 3 %. For pressures higher than 0.45 atm, the error is reduced in the

interval of +/-1 %, reaching the minimum of almost 0 % at ambient pressures. Figure 3.34 depicts these results.

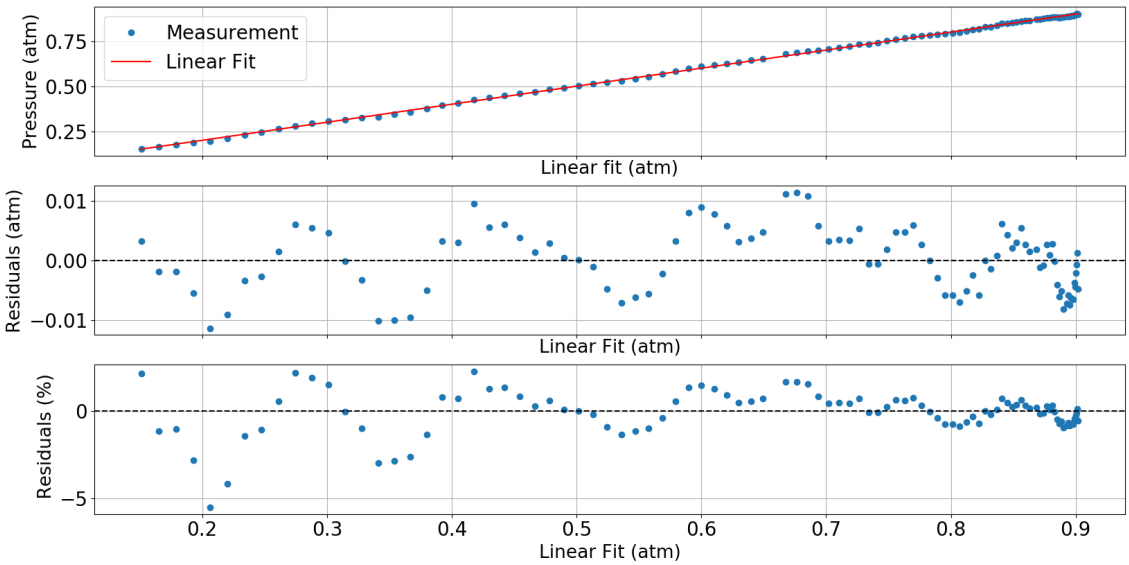


Fig. 3.34. Upper plot: measured pressure vs. linear fit (LD368). Middle plot: Residuals of measured pressure vs. linear fit(LD368). Lower plot: residuals (in percentage) of measured pressure vs. linear fit (LD368)

Plotting the measured pressure against the one from the sensor, a clearer view of the results is shown. In this case, both regressions are separated by a non-constant offset, meaning that apart of the offset induced by the calibration procedure, the laser diode itself and its working characteristics have a huge impact in the pressure estimation.

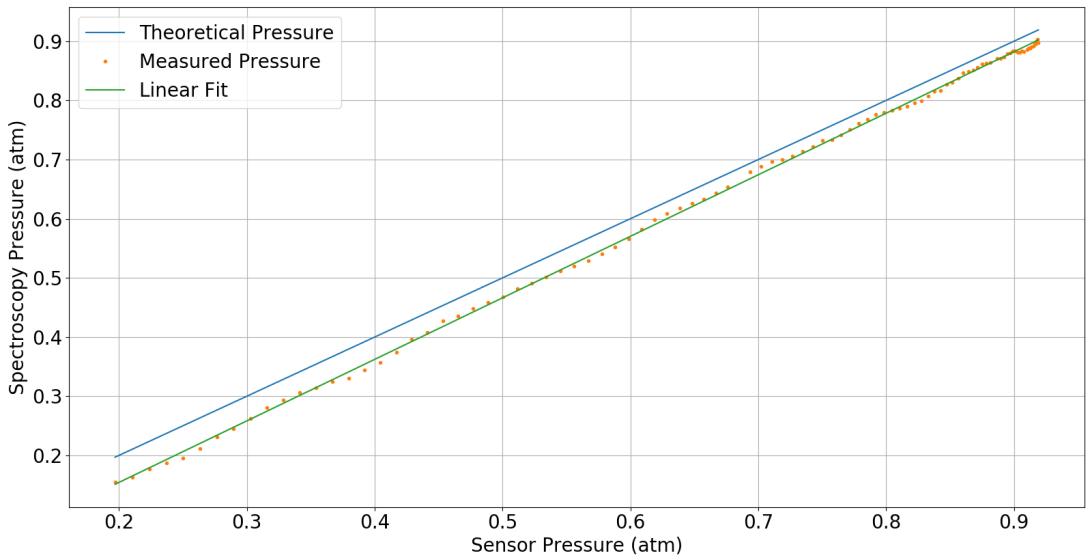


Fig. 3.35. Theoretical pressure vs. measured pressure using LD368

Although it was proved in the LD366 analysis the weight function does not improve the pressure results, a second try into the fitting of LD368 pressure results is carried out.

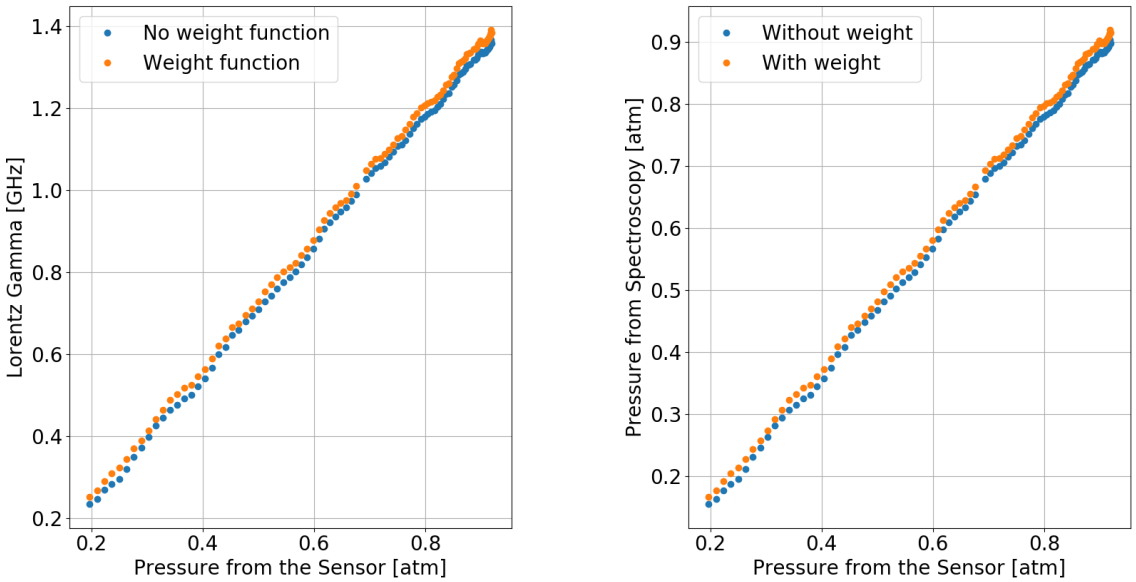


(a) Lorentz gamma vs. pressure from sensor (b) Spectroscopy pressure vs. pressure from sensor

Fig. 3.36. Spectroscopy results with and without weight function (LD368)

When including the weight function, the offsets are not reduced and sometimes even increased. This can be clearly seen in Figure 3.37. Residuals have the same order of magnitude as if the weight function was not utilized. Thus, here is double checked oscillations are not a numerical induced error but a consequence of the TDLAS setup working characteristics.

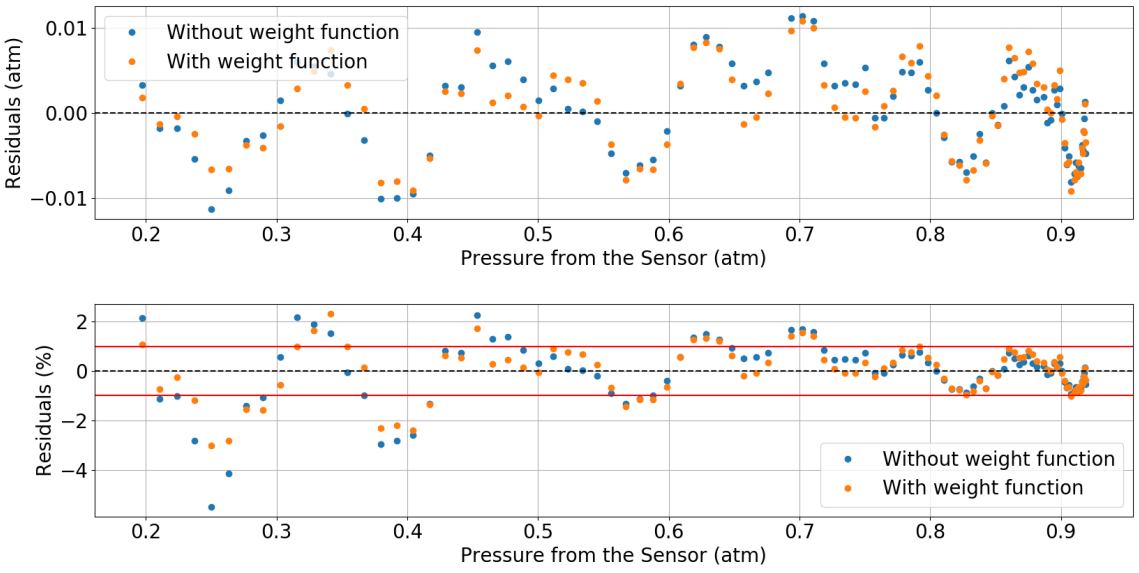


Fig. 3.37. Upper plot: residuals between measured pressure vs. linear fit with and without weight function (LD368). Lower plot:residuals (in percentage) between measured pressure vs. linear fit with and without weight function (LD368).

Just to finish, altitude at which the aircraft is flying at according to its relative value

of pressure is estimated. As expected, a higher error in the altitude values due to pressure oscillations is found. At pressures lower than 0.4 atm, the altitude error is the inside the interval of (-2300, 500) m meanwhile at higher pressure is reduced up to +/- 100 m. In relation with the altitude total error, is goes from 2300 m up to 300 m.

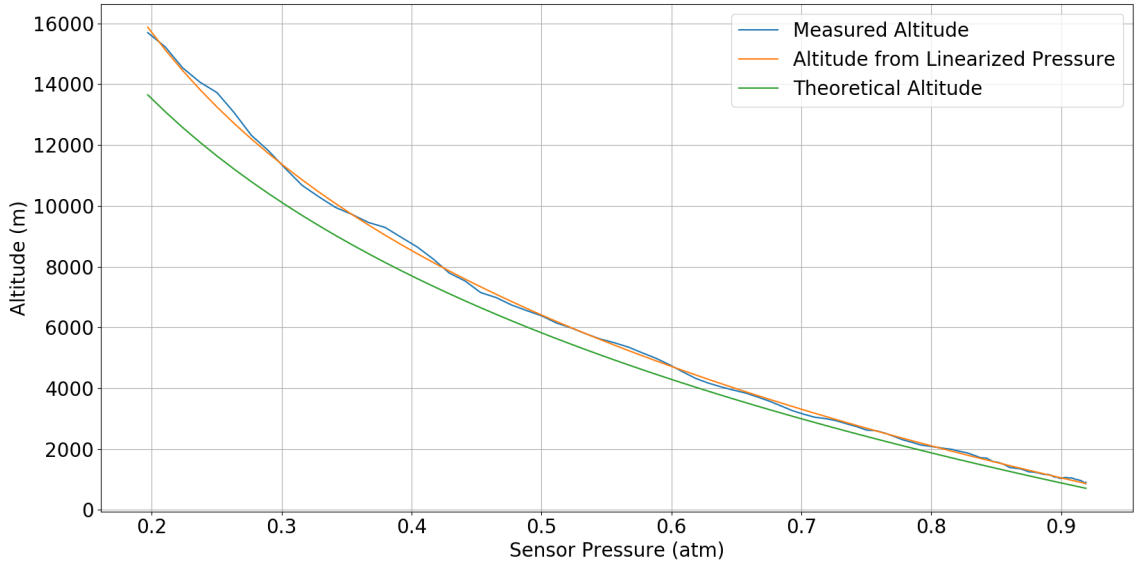


Fig. 3.38. Altitude calculation from spectroscopy pressure (LD368)

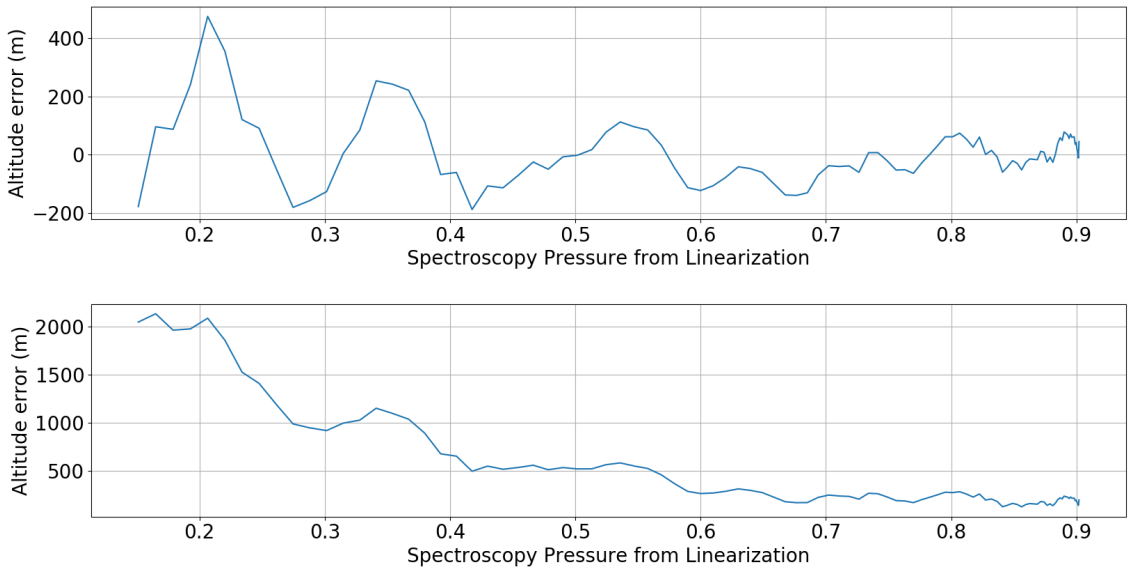


Fig. 3.39. Upper plot: Altitude errors measured and linearized pressures (LD368), Lower plot: Altitude errors mesured and theoretical pressures (LD368)

Concluding with LD368 experiments, it has been proved the possibility of estimating static pressure from spectroscopy experiments at those specific input conditions. But, results obtained here are less accurate than the ones from LD366. Here, offsets in the measures are larger and not constant overtime. Hence, it is demonstrate the working characteristics of the laser diode indeed have a influence in the absorption procedure.

The main reason for performing Experiment 3 was to estimate simultaneously same spectroscopy pressure values from both laser diodes working at different input conditions. As explained before, the combinations of LD temperature, wavelength and current leads to the appearance of different oxygen absorption lines. Therefore, to achieve the same pressure results in both experiments, this can only be done by choosing two absorption lines with the same cross sectional absorption parameter (as stated at the very beginning of this subsection). Basically, the area of both absorption lines has to be proportional as well as the width. To verify indeed this condition ad demonstrate the correct acquisition of pressure results with both laser diodes, the ratio between the Voigt amplitude has to be proved as constant. In the same vein, the ratio between both $\gamma_{Lorentz}$ has to be it too.

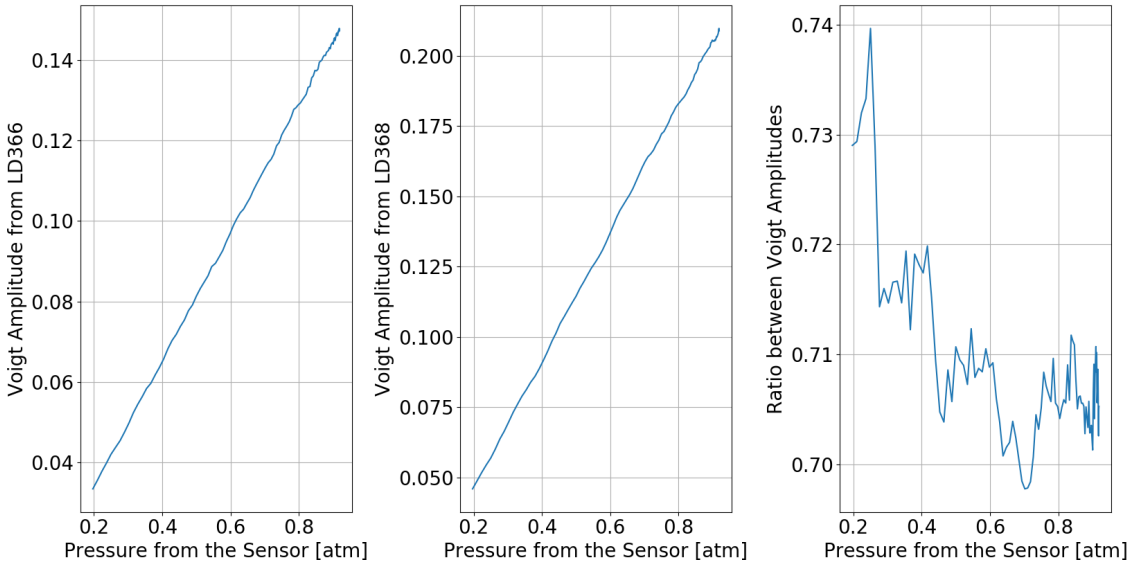


Fig. 3.40. Amplitude comparison between LD366 and LD368 experiments

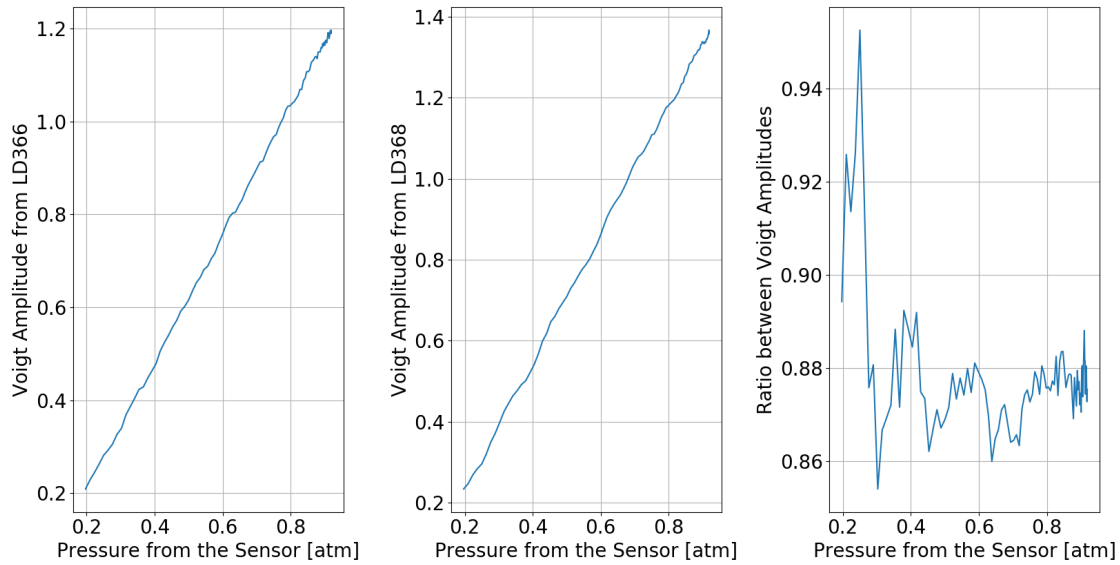


Fig. 3.41. Lorentz comparison between LD366 and LD368 experiments

Validating the experiments, Figure 3.40 and Figure 3.41 show the ratio between both

magnitudes. Because of both Voigt characteristics are oscillating, so they are their ratios. Notwithstanding, the median of amplitude and $\gamma_{Lorentz}$ ratios is approximately equal to 0.7066 and 0.8756, respectively, so, proving the input conditions for both experiments were correctly picked.

In view of finishing off Experiment 3, several conclusion are drawn. Firstly, the input settings at which laser diode is working at have a huge influence in the light absorption procedure. They must be precisely and accurately selected as they have a direct impact into the shape of absorption lines and hence, in the values of pressure results. Secondly, there exists absorption on the background that affects measurements. Although vacuum conditions were "reached" in Experiment 2, there is still an unknown extra-absorption term included in the environment. Doing an educated guess, this and the input conditions of the LD could be the main responsible factors for the measurements' oscillations. Furthermore, the incorrect calibration of the TDLAS system with the interferometer is also a detrimental effect for pressure estimation as it includes a constant offset in the values.

Despite all this, Experiment 3 demonstrates the possibility of estimating pressure from absorption when laser diodes work at different conditions. Although there is still a long way to improve the results, a successful preliminary estimation was obtained and so the chance to compute the altitude and speed the aircraft is flying at.

# 4. DESIGN

Although the design and implementation of TDLAS into the aircraft was not supposed to be covered by this Master Thesis, it has been decided to include a preliminary idea of how the resulting configuration will be set. The subsequent Chapter contains a brief description of the TDLAS shape, size and location in the aircraft.

## 4.1. TDLAS Location

To being with, the location at which TDLAS is placed on is analyzed. For convenience purposes, the aircraft selected for the flight experiments in Stage 5 is the Dassault Falcon 20. Therefore, the TDLAS location will be dependent on the Falcon's structure.

As described in Chapter 2, what makes the utilization of TDLAS so appealing is its open-path structure. Recapitulating from Section , the light beam can be directly in contact with the medium in which the measurement is performed, ensuring a more reliable and accurate results. This is particularly beneficial for the technique's location, as it can be placed outside the aircraft itself. Keeping this idea in mind, part of the TDLAS setup can be located at the fuselage's skin. More specifically, components required for the absorption procedure can be placed outside on the fuselage meanwhile remaining components can be storage inside the aircraft. Hence, the collimator, photodiode and pressure sensor will be installed in the aircraft's fuselage and the laser diode and main electronics will be housed in the aircraft's cabin. To connect both parts, optical fibers are utilized. A schematics of this structure is shown in Figure 4.1

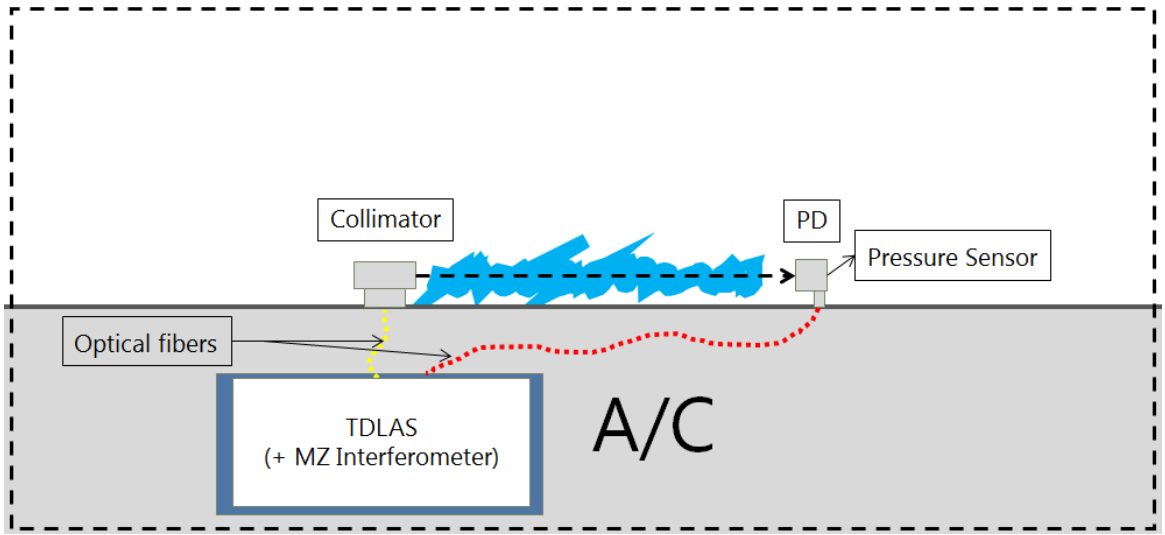


Fig. 4.1. TDLAS components' localization

Once the selection of component's location is defined, it is required to determine the

exact position of the outside components on the aircraft skin. Because this Section only contains preliminary ideas, various configurations are going to be proposed. An important aspect to consider is the existence of ports around the fuselage. To implement TDLAS, it is mandatory to re-utilized the specific ports already existing. Thus, positioning TDLAS at the lower part of the fuselage is discarded. Focusing on the upper part of the fuselage, several ideas are presented below.

In first place, a possible location here to discuss is at the fuselage's front upper part. One option can be at the 20 % of the fuselage's length. In terms of aerodynamics, the closest to th A/C nose, the most laminar flow is found. When a flow passes through a body, at the very beginning it has laminar regime. Then, due to the flow's characteristics and the body's shape, there is a transition to turbulent flow. Therefore, lower turbulence will appear at the front, making it more suitable for placing the TDLAS (Figure 4.2A). One may think placing the components one in front of the other instead of in line will give more accurate pressure results as so flow is not disturbed in between. Nonetheless, the optical technology here presented needs at least a distance of 2.2 m of separation for the absorption procedure. Because of the fuselage width is not larger enough, this configuration is rejected, but not the in-line one.

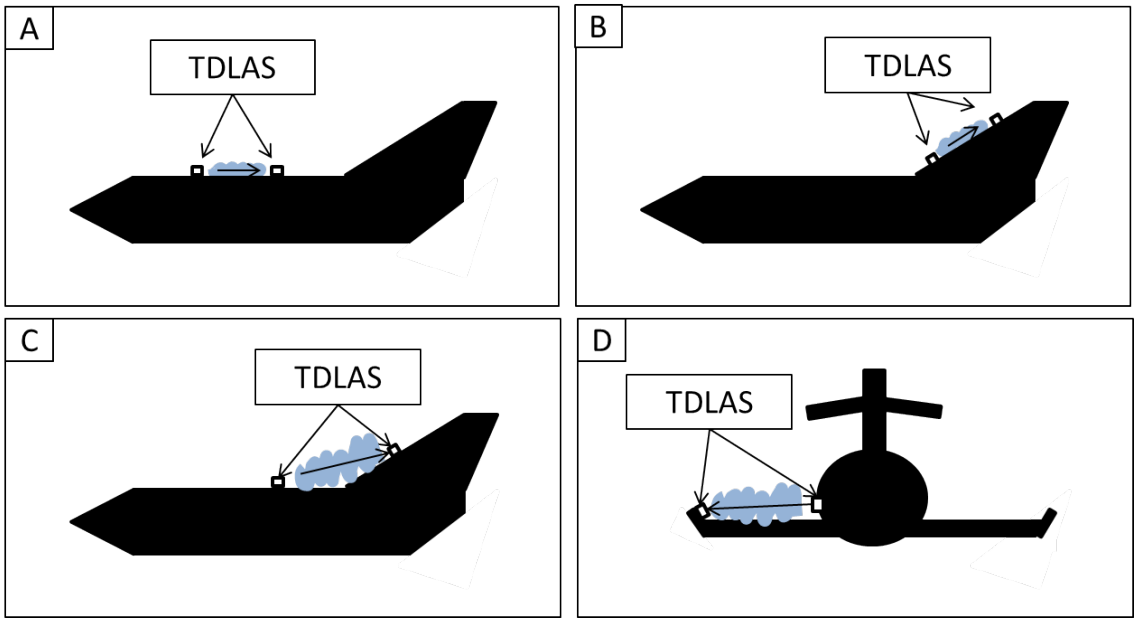


Fig. 4.2. TDLAS position in the aircraft

Other possibility worthy to mention is the location of TDLAS at the vertical stabilizer. Because the Dassault Falcon 20 is a low-wing aircraft and engines are installed in the fuselage, flow that reaches the vertical stabilizer is not deflected by any of the above and so the static pressure can be accurately measured (Figure 4.2B). A variant from this idea can be the placement of the collimator at the back of the fuselage and the photodiode and sensor at the vertical stabilizer. In this case, a more extensive study of the flow's behavior will have to be carried out due to turbulence regime the flow is at that location and the angle formed between the components (Figure 4.2C).

Finally, other potentially alternative that has been also proposed is the location of both components on the upper part of aircraft's wing (Figure 4.2D ). The collimator can be placed at the lateral skin of the fuselage and photodiode and pressure sensor at the winglet. The distance here is sufficiently large for the absorption procedure and flow's streamlines are not disturbed beforehand. However, biggest complication that may emerged from this configuration is non-accurate pressure results arisen from aerodynamics and aeroelasticity effects. During the flight profile, aircraft and wings do no have the same aerodynamic characteristics i.e. lift and drag forces. This leads to an unsymmetrical deflection over the wings' structure that must be considered for pressure measurements and adjusted via correction factor.

Although each one of the suggested architectures will have to be separately analyzed with a very explicit and elaborated aerodynamic approach to prove its viability for static pressure measurements, this Master Thesis contains a preliminary analysis of the most feasible one, which is configuration A. The selection of this one relies on its simplicity and the already existence of the ports at those locations.

## 4.2. TDLAS Design and Configuration

Continuing with the analysis, enclosures where TDLAS components will be kept in are designed. On one hand, main electronic systems, laser diodes, MZ interferometer and amplificators will be housed together in the same space inside the cabin of the aircraft. As for the collimator, photodiode and pressure sensor, specific devices will be designed for its storage. This subsection will be focused on these last ones.

The main characteristic of the device in which the design will be emphasized on is its aerodynamic shape. It is desired for the enclosure to be aerodynamically efficient, so it does not affect or modify the surrounding pressure gradients. For the purpose of fulfilling the presented feature, a broad study of possible shapes is performed. Making allusion of the existing enclosures in the aerospace field, one example are radomes. By definition, radomes are structures that protect radar antennas by enclosing them. They can have different shapes, being the most common one instated in aircraft, planar. Using radomes' shape as reference, the enclosure for both collimator and photodiode is designed.

The radome of B737MAX located at the upper part of the fuselage is described by an airfoil shape. Following the same line of though, enclosures for TDLAS are designed with this similar shape. To do so, a NACA 0024 airfoil is utilized. Due to it is desired to perturb the flow's streamlines as less as possible, a symmetrical airfoil shape is selected. Moreover, the thickness also plays an important role in the aerodynamics. Thinner airfoils allows the streamlines to be more resistant to deviations and so to generate less drag force. This is of course limited by the air compressibility effects. Thus, for preliminary analysis considering thickness as the main driver, just the trailing edge of the NACA 0024 is used. With this configuration, the length of each one of the enclosures is 1190 mm long,

enabling the best aerodynamic characteristics. With respect to the width, it is 204.07 mm. Finally, from its symmetrical structure, the height is 102.03 mm. Figure 4.3 contains a sketch with the multi-view projections from CATIA software.

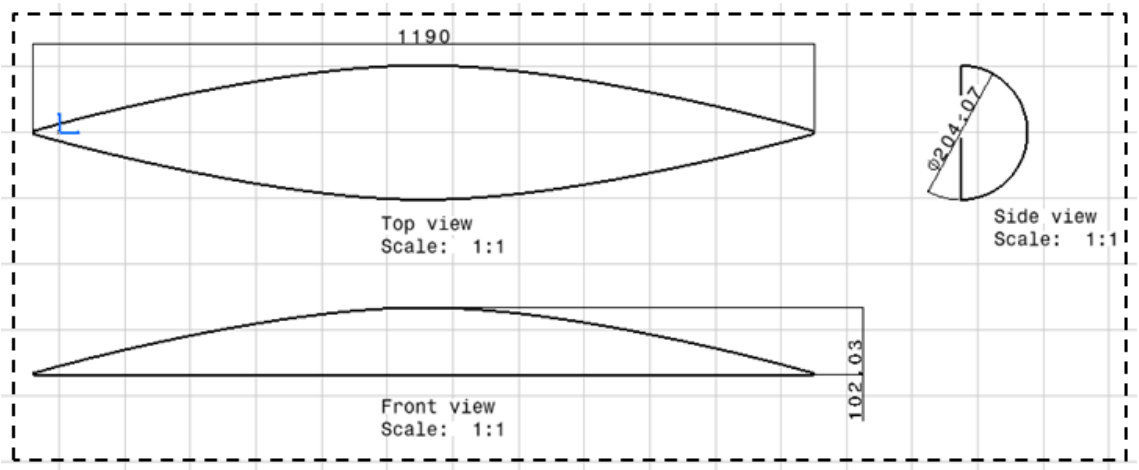


Fig. 4.3. TDLAS device dimensions

### 4.3. TDLAS Design Preliminary Analysis

Recalling from Section 4.1, it has been decided the TDLAS collimator and photodiode are going to be placed at the upper front part of the fuselage in-line with a distance in between of 2.2. m. With reference to the shape, in Section 4.2 it has established an airfoil shape for each enclosure that is going to kept both components. Thus, it can be concluded the collimator will be located at trailing edge of the first enclosure meanwhile the photodiode at the leading edge of the second enclosure.

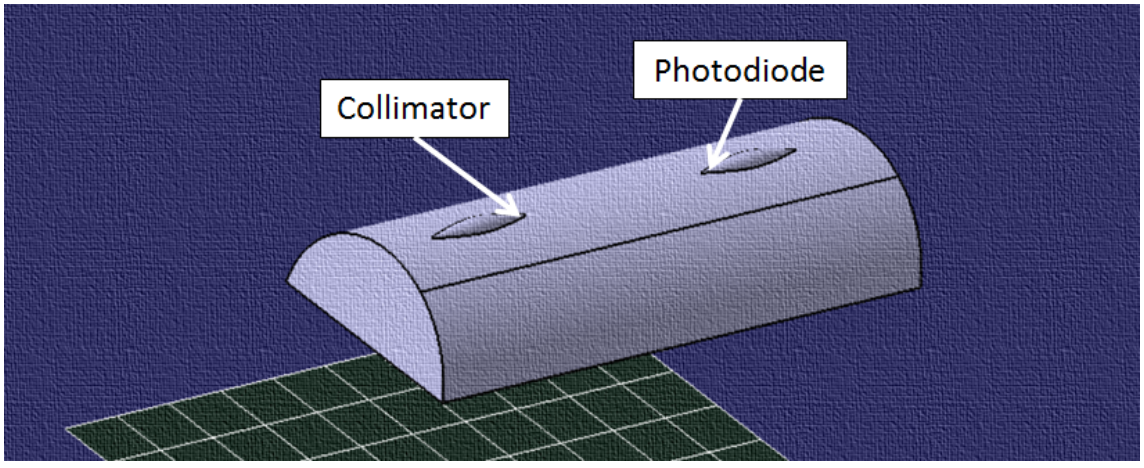


Fig. 4.4. CATIA model of TDLAS implemented in the fuselage

To obtain a preliminary idea of pressure gradients around these two implementations, a fluid dynamic analysis with ANSYS Fluent is performed. For the sake of simplicity, a cylinder is designed to simulate the aircraft's fuselage. In addition to this, the simulation

is executed at ambient density. For the speed of aircraft, 200 m/s is set for input, as it is the cruising speed of the Dassault Falcon 20. After an iterative process in 2D using the front view from the design shown in Figure 4.4 with this input conditions, the next pressure gradients are estimated.

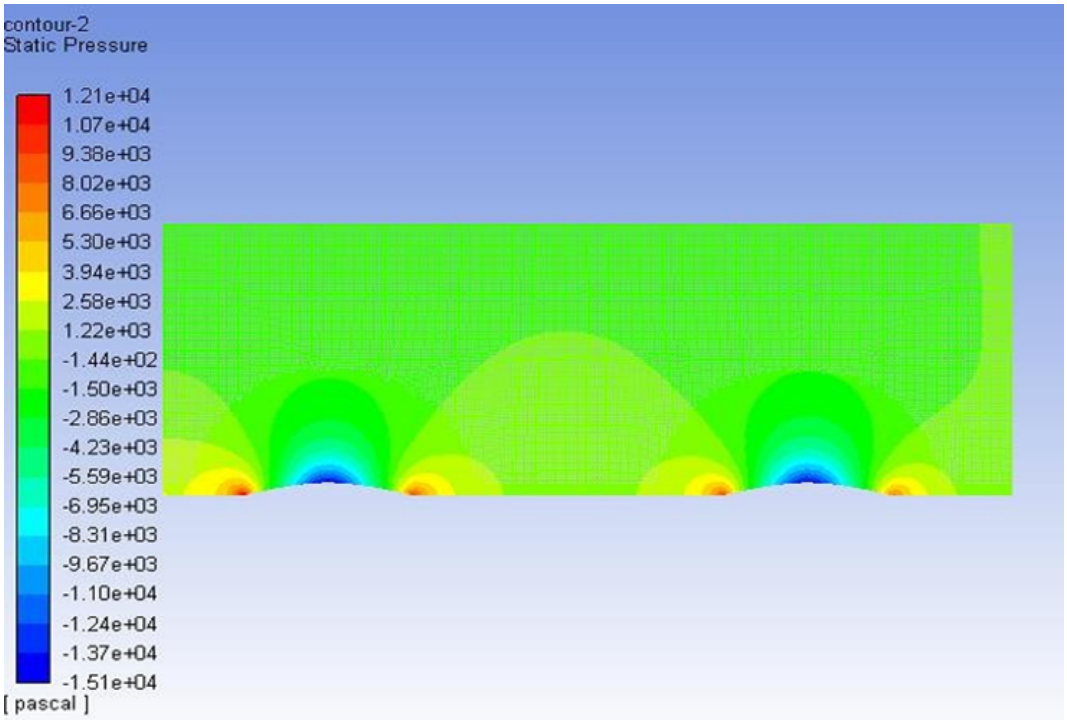


Fig. 4.5. Static pressure variation with TDLAS implemented. Front view

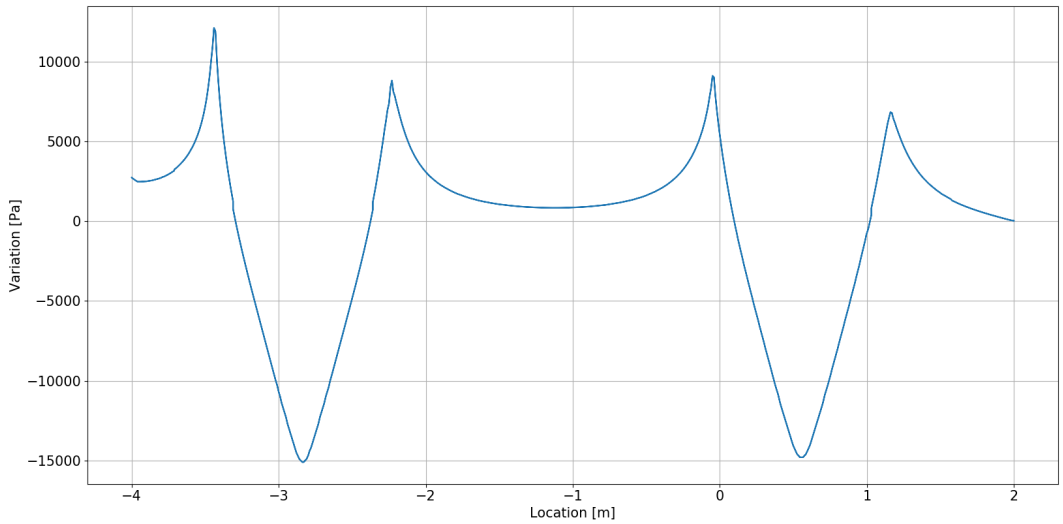


Fig. 4.6. Static pressure variation magnitude analysis at the bottom

Figure 4.5 depicts the static pressure variation over the whole control volume defined. Overemphasizing in the aim of this section, this quick simulation was only performed to have an approximate idea if the two devices implemented can cause pressure changes. Thus, the y axis has arbitrary pressure values as so all the initial parameters have not be explicit selected to simulate a real scenario. From the Figure, it is confirmed the

effect of enclosures' shape in the flow's behavior. Although it can seem at first a very abrupt change, this is not entirely true. The simulation was performed in 2D, making the assumption that the devices' length is equal to the aircraft one. Hence, in terms of accuracy, this simulation is only realistic for a perpendicular plane at the middle of the aircraft section and under laminar flow regime. To have a more accurate results, a 3D analysis needs to be carried out. Nonetheless, this last one requires a powerful computer, which is not the case.

To have a closer look to pressure results, Figure 4.6 illustrates the pressure variation at the bottom line of the control volume (at the skin of the aircraft), being centered at the leading edge of the second device. The ideal scenario will be to not have a change in pressure along the fuselage, meaning a constant straight horizontal line in this plot. Far from this affirmation, recalling the stagnation pressure definition from Section 1.1, at the leading of the first device, the static pressure is maximum as the dynamic pressure is defined with a zero velocity. Subsequent stagnation points at the leading and trailing edges are found, being their pressure magnitude lower as the velocity losses increase through the fuselage. Contrary effects happens at the top of each device, being the static pressure the lowest. These effects are indeed a consequence of the devices' shape. Despite os this behavior, the important section of the fuselage for which this aerodynamic analysis is performed is the one located in between both devices. Here, pressure is practically maintained constant, proving the viability of measuring a constant value of static pressure with optical equipment.

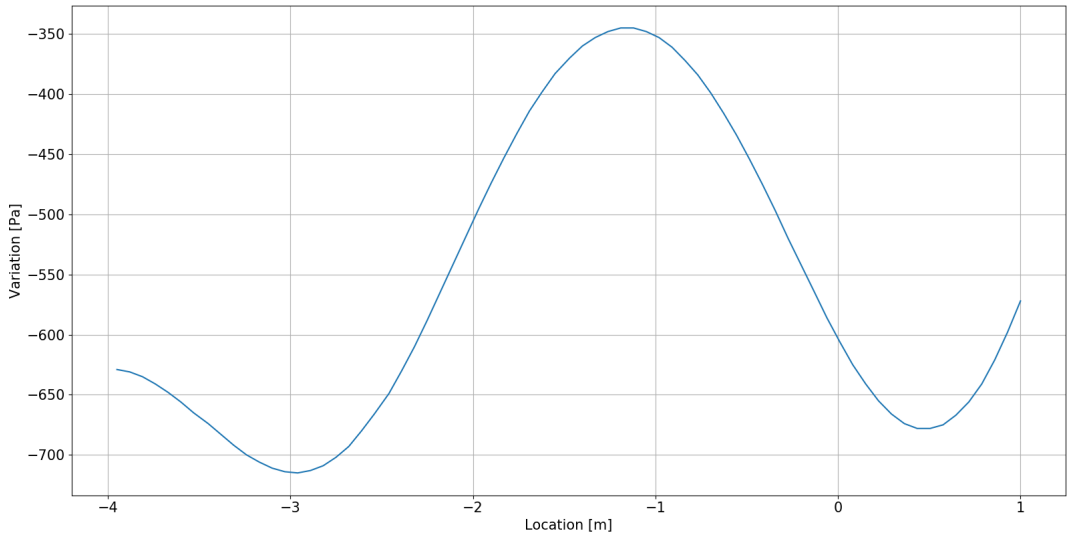


Fig. 4.7. Static pressure variation magnitude analysis at the one third

To check how much the implementation of devices affects the surrounding flow, a second simulation is performed. In this case, a line at one third of height from the bottom line is taken. Figure 4.7 shows the pressure variation at this location. Comparing both graphs, one can conclude that the altitude at which the laser beam is going to travel needs to be accurately selected, as so pressure abruptly changes with height. The further from the aircraft fuselage, the closer to the ambient static pressure value. Nonetheless, the

higher the laser beam is sent, the bigger in height needs to be the device ( influenced again by the boundary layer). Thus, a middle course will be required to be precisely selected. This is proved to be true in Figure 4.7, as higher pressure variations are found at the device's surroundings and, at the section in between, a more similar value of ambient pressure is reached, not constant and highly affected by the devices.

Just to finish, to verify indeed the above pressure variations, the top view of the device is simulated in 2D. Again, this procedure is just to have an initial clue of the flow's performance. The results obtained here are not realistic and the are only valid for a parallel plane in which flow is unidirectional.

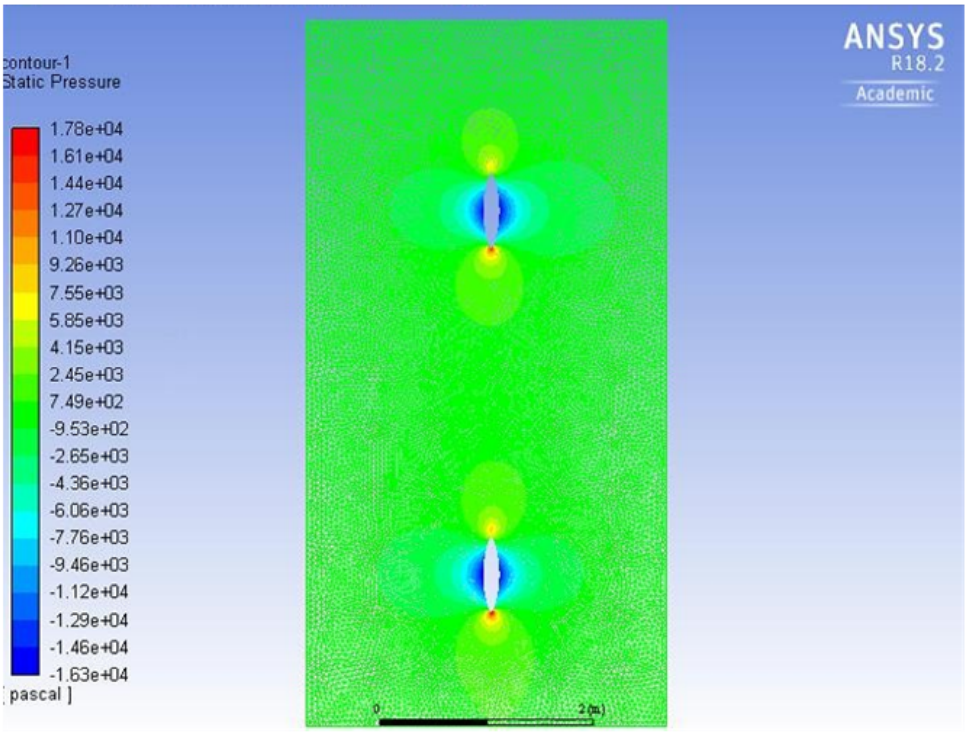


Fig. 4.8. Static pressure variation with TDLAS implementation. Top view

Concluding with the preliminary analysis, it has been demonstrate the possibility of using Configuration A for TDLAS implementation. A more detailed fluid dynamics (in 2D and 3D) analysis will be required to determine the altitude at which the laser beam will be sent. In any case, correlations between the device's height, location of the boundary condition and real pressure value will have to be extensively accurately analyzed.

# 5. CONCLUSIONS

Although it would be many years before a new static pressure measurement technique would be accepted for its implementation into aircraft, this Master Thesis has demonstrate the viability of using TDLAS for such purpose. Characterized by its open-path structure and high level technology, it provides the ability to accurately and precisely estimate atmospheric static pressure at the altitude aircraft is flying. Recapitulating from Chapter 2, its working principle relies on correlation between width of absorption lines and static pressure. Ligt beam is sent to a medium and absorbed by the species on it. Selecting oxygen as the "sensor specie", the absorption of light is defined with a Voigt profile shape. From the width of this profile, static pressure is estimated via correlation. Therefore, concluding with this underlying mechanism, TDLAS represents a non-intrusive, in-situ and real-time alternative for pressure estimations.

To validate the model, three experiments at different input conditions were performed, as stated in Chapter 3. Beginning with the simplest one, spectroscopy measurements with one LD at ambient pressure and temperature were executed. The output of analysis showed a static pressure of 1.006 atm against the 0.995 atm marked in the pressure sensor. Thus, a 0.011 atm of difference, in percentage terms 1.1 %, was obtained. Increasing gradually the complexity, a second experiment for pressure measurements with one LD but sweeping up in pressure (from 0.2 to 0.96 atm) was carried out. In this case, larger offsets between both magnitudes were found, being the smallest and largest ones 0 % and 6.8 %, respectively. Then, a third experiment with both LDs and sweeping up in the same pressures was completed. Under these input setting, a variation of spectroscopy pressure between 0.15 and 0.84 atm was acquired, being the offset with respect to its linearization of 0.005 atm (1 %) and the offset against the sensor of 0.04 atm (4.33 %).

Lastly, regarding its implementation into the A/C, its open-path structure allowed the collimator and photodiode to be placed outside the fuselage, housed inside an enclosure. The location of TDLAS has been selected to be at the upper front part of the fuselage, being both enclosures in line. At this point in the structure, more laminar flow would be reached. As for the aerodynamic shape of each device, trailing edge of NACA 0024 airfoil has been adopted. The size, indeed, was decided to have the lowest impart as possible into the streamlines, being 102x1190x204 mm. Furthermore, preliminary fluid flows analyses have been carried out to show the impact of the enclosure's shape into the flow. From them, pressure variations have been obtained, demonstrating the altitude at which the laser beam is shot effectively matters to the pressure estimation.

To sum up, the accuracy of results presented in this Master Thesis prove TDLAS to be a suitable alternative that may replace partially static-pressure measuring instruments onboard aircraft. In line with this though, due to the satisfactory outcomes, TDLAS can be proposed as a tool for others than the aerospace field.

# BIBLIOGRAPHY


[1] T. E. A. E. Berriman, *What the day have brought and what the machines have done in the military trials, The Military Competitions, FLIGHT Magazine*, 12 August 1912.

[2] F. M. White, *Fluid Mechanics, 7th edition*. Avenue of the Americas, New York: Mc-Graw Hill, 2011.

[3] J. D. Anderson, *Fundamentals of Aerodynamics, 5th edition*, 2011.

[4] Sivaranjith, *Pitot tube, working, advantages and disadvantages, https://automationforum.co/pitot-tube-working-advantages-disadvantages*, 2018.

[5] J.O.Bird and P.J.Chivers, *Measurement of fluid flow*.

[6] G. Bar-Meir, *Fundamentals of Compressible Fluid Mechanics*, 2013.

[7] B. d'Enquêtes et d'Analyses pour la sécurité de l'aviation civile, *Final Report - On the accident on 1st June 2009 to the Airbus A330-203 registered F-GZCP operated by Air France flight AF 447 Rio de Janeiro - Paris*, 2012.

[8] A. B.Buchlolz and V.Ebert, *Rapid, optical measurement of the atmospheric pressure on a fast research aircraft using open-path TDLAS, Atmospheric Mesurement Techniques, pages 3653-3654*, 2014.

[9] J. K. Delgado, *Amount of Carbon Dioxide Fraction Determination by TDLAS: Evidences for a Potential Primary Method Directly Applied in Gas Analysis*, 2006.

[10] T.-J. Ahn and D. Y. Kim, *Analysis of nonlinear frequency sweep in high-speed tunable laser sources using a self-homodyne measurement and Hilbert transformation, Applied Optics, Vol.46, No. 13, pages 2393 and 2394, https://www.osapublishing.org/ao/abstract.cfm?uri=ao-46-13-2394*, 2007.

[11] G. S. University, *Fabry Perot Interferometer, HyperPhysics, http://hyperphysics.phy-astr.gsu.edu/hbase/phyopt/fabry3.html*, 2016.

[12] S. T. Hendow, *Atomic, Molecular, and Optical Physics: Electromagnetic Radiation, Experimental Methods in the Physical Sciences, pages 343-367, https://www.sciencedirect.com/bookseries/experimental-methods-in-the-physical-sciences/vol/29/part/PC*, 1997.

[13] S. K.P.Zetie and R.M.Tocknell, *How does a Mach–Zehnder interferometer work?, Teaching Physics*, 2000.

[14] M. BAKER, *Demystifying Mixed Signal Test Methods, FREQUENCY DOMAIN TESTING AND THE FFT, https://www.sciencedirect.com/book/9780750676168/demystifying-mixed-signal-test-methods*, 2003.

[15] J. Clark, *THE BEER-LAMBERT LAW, CHEMGUIDE, https://www.chemguide.co.uk/analysis/uvvisible/beerlambert.html*, 2007(modified May 2016).

[16] T.-J. Ahn and D. Y. Kim, *Analysis of nonlinear frequency sweep in high-speed tunable laser sources using a self-homodyne measurement and Hilbert transformation, Applied Optics, Vol.46, No. 13, pages 2394 and 2395*, 2007.

[17] F. R. Kschischang, *The Hilbert Transform*, 2006.

[18] *HITRAN on the web, http://hitran.iao.ru/home*.

[19] A. B.Buchlolz and V.Ebert, *Rapid, optical measurement of the atmospheric pressure on a fast research aircraft using open-path TDLAS, Atmospheric Mesurement Techniques, pages 3653-3664*, 2014.

[20] A. Parsons, *Line Profile Functions (Spectral Line Broadening) , Youtube tutorial video*, 2013.

[21] L. M.N.Berberan-Santosa, E.N.Bodunov, *On the barometric formula*. American Association of Physics Teachers, 1996.